## DEVELOPMENT AND INVESTIGATION OF A CENTRIFUGAL COMPRESSOR FOR 10 MWe BRAYTON CYCLES USING SUPERCRITICAL ${\rm CO}_2$

By

Javad Hosseinpour

### A DISSERTATION

Submitted to
Michigan State University
in partial fulfillment of the requirements
for the degree of

Mechanical Engineering – Doctor of Philosophy

2023

#### **ABSTRACT**

Since the 1960s the idea of using supercritical carbon dioxide (s-CO<sub>2</sub>) as the working fluid in a Brayton power cycle has been entertained. But due to technical limitations of the time, the idea did not progress forward much. Presently, due to the availability of more knowledge, better technological platform, and advanced analysis tools, many believe it is time to revisit the idea of using carbon dioxide as the working fluid for power generation. Theoretically, the concept of a closed-loop s-CO<sub>2</sub> Brayton cycle is highly attractive and promising; however, there is yet a major hurdle to be passed, namely the designing, developing, and testing of a reasonable size (10 MWe or higher) prototype of an s-CO<sub>2</sub> Brayton-cycle-based power gas turbine. Specifically, designing a stable s-CO<sub>2</sub> compressor is one of the main challenges that need to be addressed.

In this dissertation, a supercritical CO<sub>2</sub> Brayton cycle design tool in Microsoft Excel coupled with CoolProp real gas NIST database was developed to optimize and analyze the power cycles as well as obtain the best operating conditions for an s-CO<sub>2</sub> compressor working in a 10 MWe power cycle. Then, three s-CO<sub>2</sub> Brayton cycles, namely simple recuperated, recompression, and dual turbine cycles were reconfigured to produce 11.11 MW (10 MWe) output net power. The results were compared to the conventional Brayton cycle as the basic s-CO<sub>2</sub> layout. It was shown that the recompression cycle had the highest efficiency, but the highest back-work ratio and the lowest specific work. Furthermore, the reconfigured simple recuperated cycle had a thermal efficiency of 43.2% with a specific work of 125.13 kJ/kg, which is in a moderate range between the dual turbine and recompression cycles. The lower capital cost of the simple cycle suggests it could be a viable option for commercialization.

Furthermore, a new compressor design procedure was introduced and developed for s-CO<sub>2</sub> centrifugal compressors with a pinched diffuser under on-design and off-design conditions in

MATLAB. The developed codes aimed to obtain a stable supercritical CO<sub>2</sub> compressor design and to predict the performance of s-CO<sub>2</sub> compressors by considering Span-Wagner real gas equation of state, condensation limit, as well as internal and external losses. The procedure was validated with experimental results for an air compressor and Sandia's s-CO<sub>2</sub> compressor to examine the validity of the meanline code. The efficiency and pressure ratio obtained from the 1-D code were compared to CFD results and showed reasonable agreement with experimental data. It was found that there was an overprediction due to not considering the volute in the design at higher mass flow rates. By comparing the total-to-static efficiency of Sandia's compressor with 1-D code and CFD, it was found that while the CFD results match the experimental data, the code could not calculate the total-to-static efficiency of Sandia's compressor for the mass flow rates below 2.5 kg/s.

Besides, a new impeller with a vaneless pinched diffuser was proposed, which achieved a compressor efficiency of 90.62% with an excellent operating range of 47.8%. The results matched well with simulations for different mass flow rates at the design speedline of 20,000 RPM. Additionally, the internal behavior of s-CO<sub>2</sub> was studied at the choke condition and a new analogy between the compressor passage and a converging-diverging nozzle was made for the high limit of the performance map. Besides, a loss analysis in the proposed s-CO<sub>2</sub> compressor was performed, revealing that 75.8% of the total enthalpy loss was due to internal losses. Finally, the condensation contours were studied and the results highlighted that condensation is unavoidable in an s-CO<sub>2</sub> centrifugal compressor; however, the condensation does not cause damage or affect the compressor's performance.

Copyright by JAVAD HOSSEINPOUR 2023

This dissertation is dedicated	l to the Imam Al-Mal the last prophet Mu	ndi (AS), the final Inhammad (PBUH).	mam from the descender	nt of

#### **ACKNOWLEDGEMENTS**

I would like to express my sincere gratitude to my adviser Professor Abraham Engeda, whose guidance and support have been invaluable throughout my academic journey. Your insights, expertise, and encouragement have helped me to grow both professionally and personally, and I am deeply appreciative of your consistent kindness. I would like to thank the respected committee members, Dr. Jaberi, Dr. Benard, and Dr. Liao for all the research discussions and helpful feedback that have helped to improve the quality of this dissertation. I would also like to thank all current and past Turbolab members, especially Mekuannint and Jonathon, who helped me significantly when I started working in this lab.

I also want to acknowledge the memory of my late dad whom I lost during my Ph.D. and whose unwavering support and love was my source of strength, and my mom, whose unwavering support and encouragement have been my driving force.

Lastly, I would like to give a special thanks to my wife. Your love, patience, and unwavering support have been the driving force behind my success. Your constant encouragement, understanding, and belief in me have helped me to overcome challenges and achieve my goals. I could not have done this without you, and I am forever grateful for your love and support.

### TABLE OF CONTENTS

LIST OF TABLES	ix
LIST OF FIGURES	X
CHAPTER 1: INTRODUCTION	1
1.1. Background	
1.2. The Need for New Alternative Energy Sources	
1.3. Attractive Concept of Supercritical CO <sub>2</sub> for Different Energy Sources	6
1.4. Objectives	9
CHAPTER 2: LITERATURE REVIEW OF RELATED WORKS	11
2.1. Introduction	11
2.2. S-CO <sub>2</sub> Brayton Cycle	13
2.3. S-CO <sub>2</sub> Compressor	
2.4. S-CO <sub>2</sub> Compressor Design Challenges	20
CHAPTER 3: CHALLENGES TO DEVELOP S-CO <sub>2</sub> GAS TURBINES	24
3.1. Introduction	
3.2. Appropriate Real Gas Equation of State	24
3.3. Current Components Needing Changes for Use in S-CO <sub>2</sub> Brayton Cycle Applica	tion 26
3.3.1. Compact Heat Exchangers	26
3.3.2. Compressors and Turbines	
3.3.3. New Seals, Bearings, and Other Design Considerations	
3.3.4. Current Attempts to Design, Manufacture, and Test S-CO <sub>2</sub> Brayton Cycles	39
CHAPTER 4: S-CO <sub>2</sub> BRAYTON CYCLE RECONFIGURATIONS	43
4.1. Simple (Conventional) S-CO <sub>2</sub> Brayton Cycle	44
4.2. Evaluation of Currently Suggested S-CO <sub>2</sub> Brayton Cycles	45
4.2.1. Simple Recuperated Cycle	45
4.2.2. Recompression Cycle	
4.2.3. Dual Turbine Cycle	
4.3. Cycle Analysis	50
CHAPTER 5: 1-D COMPRESSOR DESIGN METHODOLOGTY	53
5.1. Inlet Condition Criterion	55
5.2. Impeller Design	58
5.3. Diffuser Design	59
5.4. Loss Models	
5.5. Characteristic Design Parameters	68
CHAPTER 6: VALIDATION	70
6.1. Air Compressor	
6.2. S-CO <sub>2</sub> Compressor	72

CHAPTER 7: CFD ANALYSIS AND COMPRESSOR PERFORMANCE	77
7.1. Governing Equations	77
7.2. A Proposed Design	
7.3. CFD Results	
CHAPTER 8: CONCLUSION	95
BIBLIOGRAPHY	99

### LIST OF TABLES

Table 1: Important thermodynamic properties of potential working fluids for supercritical power cycle [26]
Table 2: Capabilities of various heat exchangers [72]
Table 3: Current development of s-CO <sub>2</sub> power cycles (Some contents were adapted from [71] and [85])
Table 4: Cycle design assumptions. 43
Table 5: Performance parameters of various layouts of s-CO <sub>2</sub> Brayton cycles
Table 6: Coefficients of cubic polynomials for Widom lines approximation [63]
Table 7: The design conditions for Eckardt Impeller-A. Design parameters were obtained from the 1-D code
Table 8: Operating conditions (design point) of Sandia's s-CO <sub>2</sub> compressor
Table 9: Design parameters of Sandia's s-CO <sub>2</sub> compressor
Table 10: Operating conditions and the design characteristics for the design point of the proposed s-CO <sub>2</sub> compressor suitable for 10 MWe power generation
Table 11: Mesh independency study (the method adapted from [118])
Table 12: The comparison between the developed 1-D code and the CFD results

### LIST OF FIGURES

Figure 1: Comparison between turbine (compressors) sizes with different working fluids [28] 8
Figure 2: Original supercritical cycle proposed by Feher [13]
Figure 3: Cycle efficiency of various power generation systems with respect to the source temperature [8].
Figure 4: Phase diagram of CO <sub>2</sub> (without solid phase) [63]
Figure 5: Properties of CO <sub>2</sub> with respect to temperature at different pressures
Figure 6: Estimation of the size of heat exchangers for different Brayton cycle layouts including their cycle efficiencies [8].
Figure 7: A typical Printed Circuit Heat Exchanger (PCHE) [74]
Figure 8: Different flow channels: (a) straight, (b) zigzag (or wavy), (c) s-shaped fins, and (d) airfoil fins [71].
Figure 9: Fouling and possible plugging of channels in a recuperator [78]
Figure 10: Pinch point in a heat exchanger [79].
Figure 11: The lab-scale compressor and turbine examples from the Tokyo Institute of Technology [45] for a 10 kW Brayton cycle
Figure 12: Advanced oil-free compliant foil bearing (CFB) [83]
Figure 13: Active magnetic bearing (AMB) system [48]
Figure 14: Application range of component and technology options for s-CO <sub>2</sub> Brayton cycle (reproduced by White et al. [71])
Figure 15: Conventional s-CO <sub>2</sub> Brayton cycle
Figure 16: Simple recuperated s-CO <sub>2</sub> Brayton cycle
Figure 17: Recompression s-CO <sub>2</sub> Brayton cycle
Figure 18: Acceptable range of selecting proper mass flow proportions for the main compressor and the recompressor in the recompression cycle
Figure 19: Dual turbine s-CO <sub>2</sub> Brayton cycle

Figure 20: The developed 1-D centrifugal compressor design procedure
Figure 21: CO <sub>2</sub> density contours along with different areas of supercritical region in the phase diagram: Liquid-like, Vapor-Like, and Widom. The Widom lines of CO <sub>2</sub> were obtained from a polynomial fit of the SW equation of state (the polynomial relations adapted from Imre [63]) 56
Figure 22: AMC calculation based on the static pressure and temperature at the inlet of the compressor
Figure 23: Incidence loss at the inlet of the impeller [98]
Figure 24: Energy loss due to the tip clearance of the impeller
Figure 25: Throat area calculation. 65
Figure 26: Leakage flow in centrifugal compressors. 67
Figure 27: Total pressure ratio and isentropic efficiency performance validation for the Eckardt Impeller-A by using the current 1-D code developed and CFD simulation for various mass flow rates at 14,000 RPM with the blade tip speed of 295 m/s
Figure 28: The geometry of Sandia's compressor generated in BladeGen by obtaining the design parameters from the current 1-D design code
Figure 29: The mesh domain of Sandia's compressor generated in Turbogrid by obtaining the design parameters from the current 1-D design code
Figure 30: Performance maps of the current 1-D code, and the CFD simulation in comparison with the measured data from Sandia for the 50,000 RPM speedline
Figure 31: Liquid mass fraction contours inside the impeller at different mass flow rates 76
Figure 32: Blade angle distribution (β) of the proposed impeller for the s-CO <sub>2</sub> compressor 82
Figure 33: Internal and external loss distributions of the proposed s-CO <sub>2</sub> compressor at the design point
Figure 34: Internal and external loss distribution of the proposed s-CO <sub>2</sub> compressor at different mass flow rates obtained from the 1-D code
Figure 35: The 3-D geometry of the proposed compressor with a pinched diffuser generated in ANSYS BladeGen
Figure 36: The opted mesh for the proposed compressor generated in ANSYS Turbogrid 86
Figure 37: Comparison of the developed 1-D code and CFD performance plots 89

Figure 38: Relative Mach number contours at different mass flow rates for 10%, 50 spans.	•	
Figure 39: Relative Mach number (ACA) behavior inside the compressor at differentes (the converging-diverging nozzle figure was adapted from [123])		
Figure 40: Liquid mass fraction contours inside the impeller at different mass flow r	ates	94

### **CHAPTER 1: INTRODUCTION**

### 1.1. Background

The typical thermodynamic cycles in generating power are Rankine Cycle and Brayton Cycle. The major difference between these two cycles is the number of phases involved in the loop. In the former, there is a phase change while only vapor is utilized in the latter. Classically, water vapor is used as the working flow in the Rankine cycle and air in the Brayton cycle. The first emergence of Rankine cycle has given rise to the popularity of this cycle conventionally [1]. However, Brayton cycles can reach a higher gas temperature in the cycle leading to higher cycle efficiency.

One of the main issues that engineers have been consistently working on is increasing the efficiencies of the power plants. For this reason, they started to think about other potential thermodynamic cycles based on the availability of the heat sources and using a different fluid medium. A brief comparison of current power cycles with respect to the thermal efficiencies and the turbine inlet temperature was made as follows:

- Organic Rankine Cycle (ORC): The turbine inlet temperature is between 320 K and 573 K
   and the cycle efficiency is between 4% and 23%, respectively [2].
- Geothermal Power Plant: The turbine operating temperature is between 358 K and 523 K
   and the cycle efficiency is between 2% and 17%, accordingly [3].
- Solar Thermal Power Plant: The turbine inlet temperature of approximately 823 K and the cycle efficiency 30% [4].
- Steam Rankine Cycle: The turbine operation is between 593 K and 893 K and the cycle
   efficiency is between 40% and 46%, respectively [5].

- Coal-Based Thermal Power Plant: The turbine inlet temperature is roughly 873 K and the thermal efficiency is between 37% and 42% [6].
- Gen-IV Nuclear Power Plant: The turbine operating temperature is ranging from 773 K to
   1173 K and the cycle efficiency is between 34% and 50% accordingly [7].
- Air Brayton Cycle: The turbine operating temperature is between 1173 K and 1873 K and the cycle efficiency is varying between 30% to 40% respectively [8].
- Combined Cycle: The turbine inlet temperature is ranging from 1373 K to 1973 K and the cycle efficiency is between 50% and 65% accordingly [9].
- Supercritical CO<sub>2</sub> Power Cycle with potential efficiencies between 20% to 65% with the turbine operating temperature varying between 573 K to 1473 K, in order [8].

In either of the abovementioned cycles, the cycle efficiency (thermal efficiency) of a power cycle is defined as the amount of work that can be generated  $(\dot{V}_n)$  compared to the energy invested  $(\dot{Q}_H)$  and it is simplified further based on the first law of thermodynamic as follows:

$$\eta_{thernal} = \frac{\dot{W}_{net}}{\dot{Q}_H} = \frac{\dot{Q}_H - \dot{Q}_C}{\dot{Q}_H} = 1 - \frac{\dot{Q}_C}{\dot{Q}_H} \tag{1}$$

While the first law provides an estimation for the efficiency of power cycles, there is a maximum limit, imposed by the second law of thermodynamics, for the cycle efficiency which is termed Carnot efficiency and is defined as follows:

$$\eta_{carnot} = 1 - \frac{T_C}{T_H} \tag{2}$$

where  $T_C$  is the temperature of the cold reservoir and  $T_H$  is the temperature of the hot reservoir. By increasing the temperature of the hot reservoir and/or decreasing the temperature of the cold reservoir, higher Carnot efficiency can be achieved. However, due to the irreversibilities, frictions, and losses that exist in the actual processes of a cycle, it is not possible to reach the Carnot

efficiency. Regarding the efficiency of a cycle, improving energy harvest from the hot and cold reservoirs leads to higher thermal efficiency. That is, better energy transfers in the heat sink and heat source improve the cycle efficiency. Further, increasing the isentropic efficiencies of turbomachinery components including compressor and turbine results in higher cycle efficiency. Last but not least, reducing the parasitic power required for the balance of the power plant including the generator, heat exchangers, and control system [10].

In 1950, an attractive alternative was proposed by Sulzer [11] for the first time and then developed further by Angelino [12] and Feher [13] initially to exploit the benefit of carbon dioxide near the critical point aiming to increase the performance of the power cycles. It was found when the power cycles operate in the supercritical region, higher cycle efficiencies of around 50% can be accomplished [14] by reducing the compression work required. In supercritical conditions, the compressibility factor decreases and reaches a value of 0.27 and the density of the fluid increases significantly. Thus, by employing supercritical fluid, the benefits of the Rankine power cycle (high-density working fluid with higher efficiency) and Brayton power cycles (higher temperature and pressure in which cycle operates) can be utilized simultaneously to reach higher thermal efficiency even at moderate turbine inlet temperatures.

### 1.2. The Need for New Alternative Energy Sources

Electric power for the grid is primarily generated by combining a high-energy source with a thermodynamic power cycle. Improving the efficiency of the cycle is crucial to ensure cost-effective power generation. The two most commonly used power cycles are direct-fired open Brayton cycles and indirect-fired closed Rankine cycles [14]. The type of cycle used depends on the available heat source, which can come from thermal sources (natural gas, coal, and petroleum),

renewable sources (geothermal, wind, and solar energy), or nuclear energy. Coal-fired, geothermal, and solar power plants are often used in steam turbines (Rankine cycles) [5].

Rankine cycles usually operate with water as the working medium in two phases: liquid and vapor. Initially, the water is pumped to increase the pressure of liquid water before its temperature being increased in a heat transfer process from an external heat source. In this process, the phase of the liquid water changes to vapor in the superheated condition. Then, the energy of the high temperature and pressure of the superheated fluid is converted to mechanical work through expansion in the turbine, which is utilized to generate electricity in most applications. The input work for the pump in this cycle is predictably small and the work ratio  $(\dot{W}_n/\dot{W}_t)$  of approximately 1% - 2% [15] is typical due to the high density of water. The pressure ratio of the pump is high in the order of 1000 [15]. The high-pressure ratio and high temperature in Rankine cycles are limited to the material structure. One of the drawbacks of the steam cycle is condensation which may occur in the turbine leading to the erosion of the blades in the long run. Consequently, this phenomenon reduces the turbine isentropic efficiency and the cycle efficiency. The thermal efficiencies of most supercritical coal-based steam cycles, which have a turbine inlet pressure of 24.1 MPa g (Mega Pascal plus atmospheric pressure) and turbine inlet temperature of 839 K, reach the thermal efficiency of about 40% [5]. It is worth noting that this condition is considered a standard steam condition [5] for an ultra-supercritical (USC) steam cycle. When the inlet turbine temperature of the steam Rankine cycle is high, greater than 823 K, further efficiency improvement is required. Nevertheless, material degradation is inevitable in high-pressure and high-temperature conditions [8].

On the other hand, the Brayton cycle uses air as the working fluid, and it conventionally works in an open-loop system. Brayton cycles typically consume natural gas, jet fuel, diesel fuel,

or kerosene as the fuel source [16]. The cycle begins with compressing air from the atmosphere at the ambient pressure and temperature in the compressor. Then, the fuel is injected into a combustor and combustion takes place. The high temperature and pressure products rotate the turbine blades and the combustion products are discharged into the atmosphere through a nozzle. A portion of the generated work by the turbine is employed to drive the compressor continuously and the remainder of extracted power may be either utilized to generate electricity or accelerated through a nozzle to increase momentum (thrust) for the propulsion application. Since the density of air is very small compared to water in the Rankine cycle, more work is required to compress this medium in the Brayton cycle. As a result, the back-work ratio is between 40% and 80% [17], and the achievable pressure ratio is much less than the Rankine cycle, in the order of 10. Further, since Brayton cycles utilize materials compatible with the high-temperature operations, higher temperatures can be reached. In other words, the maximum temperature that turbine blades endure is 1300 K, and higher temperatures, up to 1600 K, are feasible for ceramic blades [17]. However, the thermal efficiency of air Brayton cycles is expected to be between 30% to 40% [8].

Due to the enormous energy needs and the environmental challenges, an alternative energy source is required. Several studies have shown that supercritical CO<sub>2</sub> power generation can achieve significantly higher thermal efficiencies (more than 50%) than either the advanced USC Rankine cycles or the conventional air Brayton cycles [18-20]. Higher cycle efficiencies imply lower water usage, lower fuel cost, and lower gas emissions. Moreover, the high density of s-CO<sub>2</sub> results in equipment compactness, lower capital cost, and a smaller plant footprint. The main issue is the high-pressure operating condition, which is controlled by the high temperatures of roughly 1573 K or higher [21]. While the benefits of s-CO<sub>2</sub> power cycles are manifold, there are some challenges that need to be addressed including the new equipment design to be suitable for the s-CO<sub>2</sub>

application, and material considerations impacting both technical viability and economic feasibility. Therefore, because of the high energy demands and the stricter environmental protection regulations, it is necessary to seek power-generating alternatives with more potential in highly efficient power cycles as well as less plant footprint.

## 1.3. Attractive Concept of Supercritical CO<sub>2</sub> for Different Energy Sources

By Introducing supercritical carbon dioxide (s-CO<sub>2</sub>) application as the working fluid, the thermal efficiency of the Brayton cycle can be enhanced further compared to the conventional air Brayton cycles and Rankine cycles. One of the appealing features of the s-CO<sub>2</sub> power cycles is a wide variety of applications in the moderate temperature range such as Waste Heat Recovery [22], Concentrated Solar Power [23, 24], and Gen IV reactors [25]. The principle of a supercritical CO<sub>2</sub> power cycle is to utilize a fluid in the close vicinity of the critical point to benefit from the low compressibility and higher density of the fluid. In these cycles, the working fluid is compressed in the supercritical condition and then flows through a recuperator (regenerator) to recover some of the energy exiting the turbine back into the cycle. Thereafter, the working medium enters a heat exchanger to reach the maximum temperature of the cycle before it enters the s-CO<sub>2</sub> turbine.

An important question that needs to be answered is if CO<sub>2</sub> is the best working fluid to operate in a supercritical Brayton power cycle or if there is a better alternative. To answer this question a brief comparison was made in Table 1 between air, water, helium, nitrogen, and carbon dioxide regarding the critical temperature, critical pressure, and density of the fluids. It is clear from this table that the critical condition of CO<sub>2</sub> is quite reachable compared to the other fluids which are either too high, such as water, or too low, such as helium.

Table 1: Important thermodynamic properties of potential working fluids for supercritical power cycle [26].

Fluid Medium	T <sub>critical</sub>	P <sub>critical</sub>	ρ <sub>@critical</sub>
	<b>(K)</b>	(MPa)	$(kg/m^3)$
Air	132.5	3.79	344.3
Water	647.1	22.06	321.0
Не	5.2	0.23	55.9
$N_2$	126.2	3.39	309.3
$\mathrm{CO}_2$	304.1	7.38	481.0

Further, some research demonstrated that s-CO<sub>2</sub> turbomachinery can be one-hundredth of a steam

turbine with the same power generation [27]. The high density and low compressibility factor (0.27) of s-CO<sub>2</sub> near the critical region entail lower compression work required to obtain the same pressure ratio in a compressor. Consequently, smaller turbomachinery components are needed compared to the compressors and turbines of air Brayton cycles or steam turbines. Figure 1 provides a sensible comparison between steam, helium, and s-CO<sub>2</sub> turbines with comparable sizes to the steam, helium, and s-CO<sub>2</sub> compressors, respectively. Besides, supercritical carbon dioxide is a non-corrosive fluid medium compared to water due to the low dynamic viscosity of s-CO<sub>2</sub> [10]. It is worth mentioning that CO<sub>2</sub> is stable, relatively inert, and non-toxic. Its thermodynamic properties are also known, and it is abundant in nature meaning the low cost of CO<sub>2</sub> [28]. The carbon dioxide (CO<sub>2</sub>) Brayton power cycle was proposed first by Sulzer [11] in 1950 and later in 1968, Angelino [12] evaluated several condensation (transcritical) CO<sub>2</sub> cycle configurations in which the heat of the fluid is rejected below the critical conditions, in the heat rejection process, resulting in the condensation of CO<sub>2</sub>. In the same year, Feher [13] proposed the supercritical carbon

dioxide power cycle operating above the critical temperature and pressure, as shown in Figure 2,

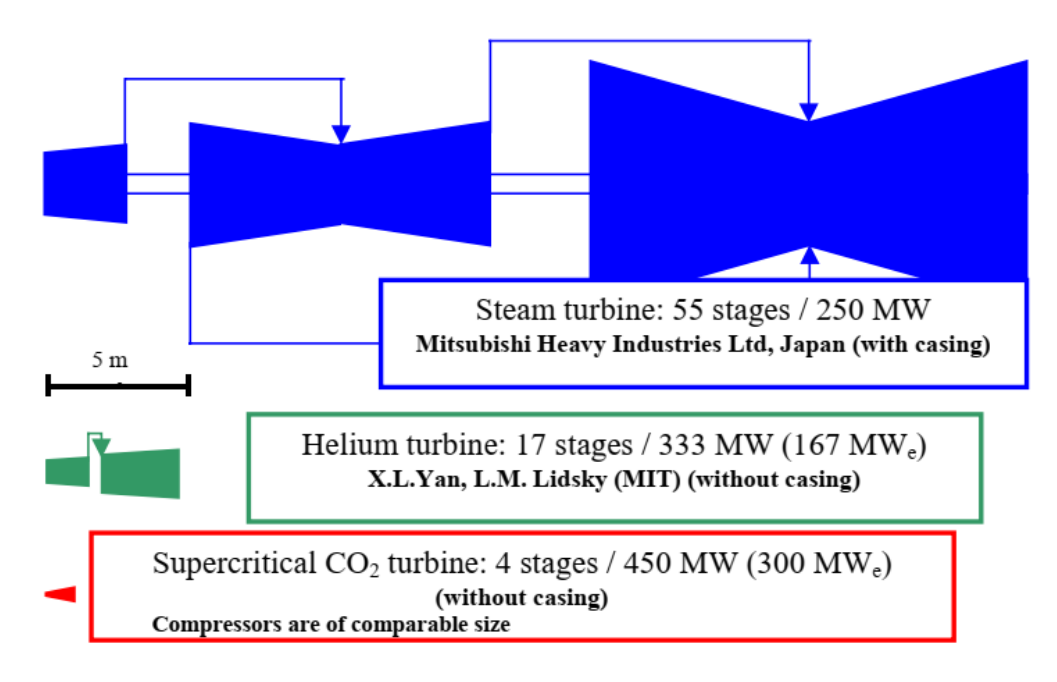


Figure 1: Comparison between turbine (compressors) sizes with different working fluids [28].

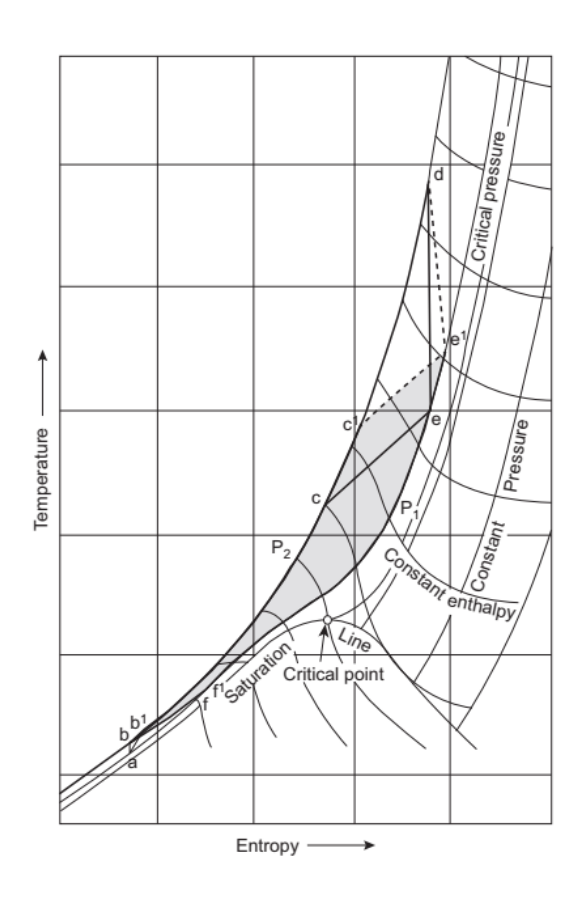


Figure 2: Original supercritical cycle proposed by Feher [13].

in the power cycle increasing the cycle efficiency. The idea of s-CO<sub>2</sub> power generation did not progress forward much due to technical limitations of the time for turbomachinery components. In 2004, Dostal [28] revisited this concept for nuclear reactor applications. Presently, due to the availability of better technological platforms, more knowledge, and advanced analysis tools, many believe it is time to reconsider the idea of utilizing s-CO<sub>2</sub> as the working fluid for power generation.

### 1.4. Objectives

The exclusive properties of supercritical CO<sub>2</sub> as a working fluid operating in a closed-loop Brayton cycle (higher thermal efficiency, smaller turbomachinery size, lower capital cost, less water use, and lower emission) grabbed the attention of the Department of Energy (DOE) and other international governments and institutes. This technology is in a developing stage with high potentiality, unlike steam turbines. However, the realization of these benefits will depend on overcoming several technical, engineering, and materials science challenges. Even though theoretically, the concept is highly attractive and promising, there is yet a major hurdle to be passed, namely the designing, developing, and testing of a reasonable size (10 MWe or higher) prototype of an s-CO<sub>2</sub> Brayton-cycle-based power gas turbine.

Some s-CO<sub>2</sub> Brayton cycle demonstrations with power generation ranging from 100 KWe to 1 MWe were developed in the laboratory scale. However, more studies and research need to be conducted towards developing and commercialization of a sufficient size (10 MWe or higher) s-CO<sub>2</sub> Brayton cycle. Recently in March 2017, a team managed by Gas Technology Institute (GTI), General Electric, Southwest Research Institute (SwRI), and General Electric Global Research (GE) with the support of DOE launched a seven-year project, known as the STEP Demo project, to construct a reconfigurable 10 MWe s-CO<sub>2</sub> pilot plant test facility. Previous works imply that

considerably more research is required to address the design challenges and to commercialize an s-CO<sub>2</sub> Brayton cycle.

This dissertation aims to support the effort for the development of the 10 MWe Brayton Cycle. For this purpose, three well-known s-CO<sub>2</sub> Brayton cycles, namely simple recuperated, recompression, and dual turbine cycles are reconfigured thermodynamically. Further, a new 1-D design procedure will be introduced by using the Span-Wagner real gas equation of state, acceleration to condensation margin, and internal and external losses to obtain a reliable and stable supercritical CO<sub>2</sub> compressor which is the main objective of this research. Two 1-D codes were developed to provide the geometry of the impeller from the on-design code and the performance map from the off-design code. Being the geometry of the designed compressors available, a comprehensive aerodynamics analysis will be performed by using the ANSYS CFX tool. To achieve this goal, we need to accomplish the divergence problem near the critical point when we are using CFD packages by using a proper equation of state. Moreover, the performance plots from the 1-D code and CFD will be validated against the available data for an air compressor and an s-CO<sub>2</sub> compressor. Finally, a new s-CO<sub>2</sub> compressor will be proposed based on the design procedure developed and the condensation analysis will be conducted and the CFD results will be discussed in detail.

# CHAPTER 2: LITERATURE REVIEW OF RELATED WORKS

### 2.1. Introduction

Increasing the cycle efficiency of power plants has been always a subject of interest to reduce the cost of operation and minimize losses. As mentioned before, power may be generated in either Rankine or Brayton cycle platforms. Due to the first emergence of the former in the form of steam engines traditionally [1], it has been more popular than the latter. However, Brayton cycles can reach a higher gas temperature in the cycle with higher cycle efficiency. By introducing the concept of utilizing s-CO<sub>2</sub> as the working medium in the Brayton cycles in the 1960s, the efficiencies of power cycles can be improved further attracting the attention of the designers and national labs. As shown in Figure 3, an interesting feature of the supercritical carbon dioxide power cycle is the adaptability of the cycle to operate in extensive source temperature applications including coal power, waste heat recovery, renewable energy, and nuclear application, as previously studied by Sandia National Laboratories (SNL) [1] and Ahn et al. [8].

There are two primary approaches for s-CO<sub>2</sub> Brayton cycle designs, directly-fired and indirectly-fired loops. In an indirectly fired s-CO<sub>2</sub> Brayton cycle, a heat exchanger is utilized to function as the heat source increasing the temperature of the carbon dioxide in the power cycle. The secondary fluid in the heat exchanger will be heated in a conventional boiler if steam is the working medium. On the other hand, the CO<sub>2</sub> heater is substituted by a combustor in a directly fired design in which the fuel is burned close to stoichiometric conditions to produce the maximum heat in the combustor. The main products of combustion, CO<sub>2</sub> and water, are employed to power the turbine. The remaining heat is recovered in the recuperator, and then the water is condensed in a cooler and then removed from the system before entering the compressor. The high-pressure CO<sub>2</sub>

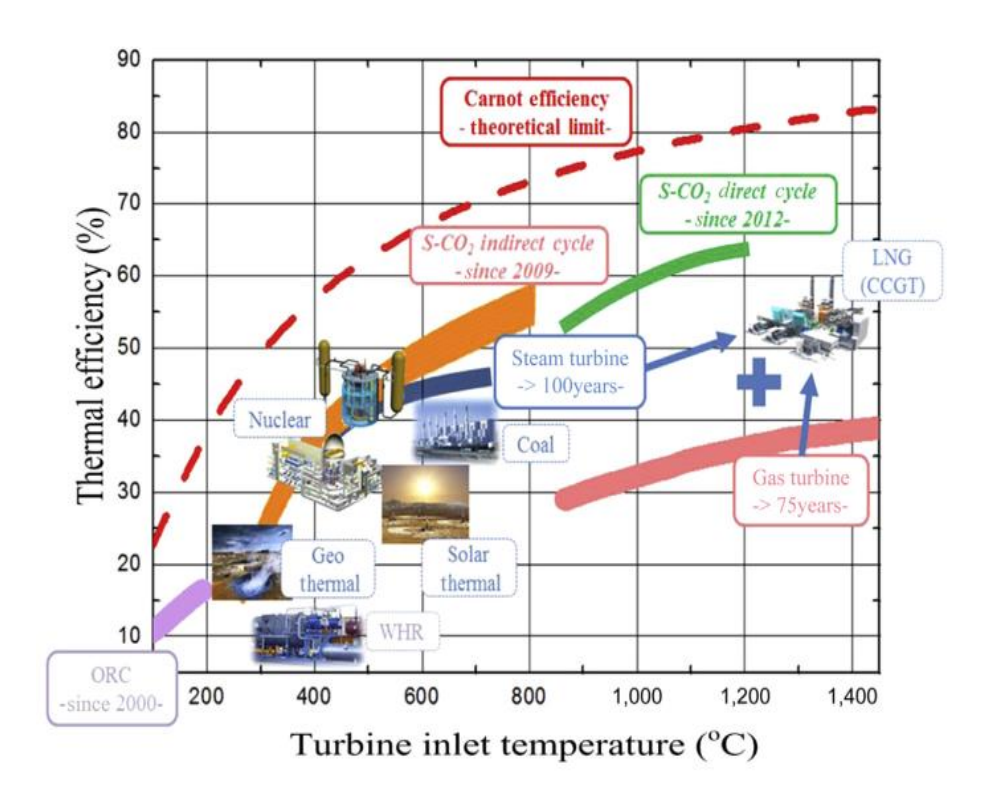


Figure 3: Cycle efficiency of various power generation systems with respect to the source temperature [8].

partially enters the recuperator to be preheated and recover the remaining energy of the turbine exit before entering the combustor as a diluent to control the temperature. Another potion of the compressed CO<sub>2</sub> is stored in a storage tank. The directly-fired scheme is suitable for the oxycombustion systems by the means of gaseous fuels such as coal-gasification syngas, and natural gas [29]. Further, higher turbine inlet temperature (~1450 K) can be achieved resulting in a higher cycle efficiency compared to the indirectly fired s-CO<sub>2</sub> cycles [10, 29].

In this chapter, the current progress in the design, building, testing, and analyses of s-CO<sub>2</sub> power cycles will be reviewed. Further, the attempts that have been made up to the present by other researchers will be also provided regarding the compressor design, which is the main concentration of the current dissertation.

### 2.2. S-CO<sub>2</sub> Brayton Cycle

To date, some measures have been taken to develop a demonstration of an s-CO<sub>2</sub> Brayton cycle which will enable the designers to move forward toward designing, building, and testing a reasonable commercial-size (10 MWe or higher) prototype of an s-CO<sub>2</sub> Brayton-cycle-based power gas turbine. Moullec [30] proposed a power plant concept to evaluate the potential employment of a coal-fired power plant integrated with an s-CO<sub>2</sub> recompression Brayton cycle. His detailed study showed that the LHV efficiency is around 47.4% and 50.8% when CO<sub>2</sub> is compressed to 200 bar and 350 bar, respectively. Bechtel Marine Propulsion Corporation (BMPC) tested a closed-loop Brayton cycle with a turbine-driven generator and a turbine-driven compressor by utilizing s-CO<sub>2</sub> as the process fluid. The power cycle was operated and controlled through an integrated system test to produce 100 kWe at 75,000 RPM with the turbine inlet temperature of 572 K and outlet compressor pressure of 16.7 MPa [31-33]. They also examined the off-design point power generation, and the net power peaked at 17.6 kW at the speed of 55000 RPM. Sandia National Lab designed and assembled a 250 kWe s-CO<sub>2</sub> recompression Brayton cycle with the compressor inlet temperature and pressure of 305.4 K and 7.69 MPa as well as the turbine inlet temperature of 811 K, accordingly. The cycle consisted of two turbine-alternator-compressor (TAC), two PCHE recuperators, a PCHE precooler, and six immersion heaters [34]. Iverson et al. [35] investigated the transient response of a 250 kWe s-CO<sub>2</sub> Brayton cycle prototype working with solar-thermal energy by reducing the thermal input by 50% and 100%. They found that the thermal mass could operate for short times even with fluctuations until the thermal energy input can recover. They also mentioned that energy storage systems can moderate the transient behavior where considerable thermal energy storage is included in the power plant design. Wang et al. [36] modeled the performance of various s-CO<sub>2</sub> Brayton cycles coupled with a molten salt solar power tower system. They reported that the temperature difference of molten salt in the simple recuperated, precompression, and partial cooling cycles are slightly larger than recompression, split expansion, and intercooling cycles.

Southwest Research Institute developed a turbine to be assembled and tested in a 1 MWe closed s-CO<sub>2</sub> recompression Brayton cycle in temperatures higher than 973 K, for the Concentrated Solar Power (CSP) application [37, 38]. Xi'an Thermal Power Research Institute designed an s-CO<sub>2</sub> recompression cycle incorporated with the coal-fired power plant in the preliminary stage to generate 5 MW power. Their proposed recompression and reheat cycle customized for the fossil-based power plant could achieve a net efficiency of 33.49% for the compressor's discharge pressure, and the turbine inlet temperature of 20 MPa, and 873 K [39]. Shouhang and EDF retrofitted the extant Shouhang's 10 MWe Rankine cycle incorporated with the CSP to the closed s-CO<sub>2</sub> power plant adapted to CSP heat source and operated in the turbine inlet temperature and pressure of 741 K and 25 MPa [40]. Ahn et al. [8] reviewed the technology development of the s-CO<sub>2</sub> power cycle and compared several s-CO<sub>2</sub> cycle layouts. They concluded that the recompression cycle has the highest efficiency according to the previous studies; however, the recompression cycle requires the largest recuperators by estimating the UA ratio quantity (overall heat transfer rate multiplied by the heat transfer area compared to the simple recuperation cycle). Crespi et al. [41] examined twelve supercritical CO<sub>2</sub> cycles systematically under comparable conditions to probe the performance of the cycles in terms of efficiency and specific work. They considered the second law of thermodynamics in their study by defining the Carnot factor. They reported that the recompression cycle with partial cooling and reheating provides the highest efficiency when temperature and pressure limitations were not considered.

### 2.3. S-CO<sub>2</sub> Compressor

The compressor design is one of the main challenges that need to be addressed when the working fluid is supercritical at the inlet of the compressor. Previous studies showed that the change in the property of carbon dioxide near critical condition is very abrupt with minor changes in temperature or pressure.

Some attempts have been made to develop compressors to be suitable for supercritical CO<sub>2</sub> Brayton cycle applications in recent years. In 2004, Wang et al. [42] developed a preliminary design of an axial compressor and a recompressor by using real gas properties in the AXIAL program for a 300 MWe s-CO<sub>2</sub> Brayton cycle. They analyzed a steady-state on-design and off-design points and showed that the s-CO<sub>2</sub> compressor sizes are smaller compared to the helium compressors with the same adiabatic efficiency. Gong et al. [43] employed the conventional Balje method, using specific speed and specific diameter, to estimate the size and performance of the main compressor for a 300 MWe s-CO<sub>2</sub> power conversion system. They modified the GAS-PASS code to study the transient and dynamic performance of the compressors for the off-design conditions. They also recommended single-stage and three-stage radial compressors for the main compressor and the recompressor, respectively.

Regarding the experimental work, to the best knowledge of the author of this dissertation, only three test facilities [44-46] have been developed across the universe which were built to test the operability of s-CO<sub>2</sub> power cycles with the power generation of less than 0.5 MW. Sandia's contractor Barber Nichols designed an s-CO<sub>2</sub> compressor for a 250 kWe power cycle. They developed a methodology that allows conventional engineering design tools to be utilized even though the behavior of supercritical CO<sub>2</sub> deviates substantially from ideal gas [44]. That is, they opted for a surrogate fluid having the key properties in the ideal region similar to the supercritical

CO<sub>2</sub> in the real region. Sandia also measured the efficiency of the designed compressor at different speeds and provided the performance map of the compressor for the SNL s-CO<sub>2</sub> test loop. Tokyo Institute of Technology [45] developed an s-CO<sub>2</sub> centrifugal compressor for a test facility of a 10-kW closed-loop simple-recuperated Brayton cycle. They analyzed the aerodynamics of the compressor computationally by using COMPAL meanline program and compared the off-design performance of the compressor with their measured data. However, their developed cycle could only generate 110 W. They identified that the major loss of output generated power originated from the windage loss in the compressor due to the high speed of the rotor, 85,000 rpm. It is worth mentioning that windage loss is proportion to  $\omega^3$ , and  $\tau^4_{rotor}$ . Korea Advanced Institute of Science and Technology [46] utilized an s-CO<sub>2</sub> pressurizing experiment with a 26-kW compressor to obtain the compressor data near the critical point of CO<sub>2</sub>, 305.65 K, and 7.44 MPa. They also simulated the measured data with a 1-D revised GAMMA+ code to validate their code by comparing it with the revised code.

Some researchers [47-49] investigated 1-D or meanline designs. In the meanline analysis, only the inlet and outlet conditions of the compressor are used to calculate the geometry and subsequently the performance of the compressor for only one streamline, the Root Mean Square Streamline. Meanline analysis enables a designer to evaluate the key design parameters such as load distribution and backsweep angle. It also provides the performance of the geometry at different rotational speeds, and flow rates [50].

In 2012, Korea Advanced Institute of Science and Technology (KAIST) and Khalifa University [47] jointly developed an in-house code, TURBO\_DESIGN, based on the real gas consideration for supercritical CO<sub>2</sub> axial and centrifugal compressors. They also tried to validate their code with the experimental data from Sandia by comparing pressure ratio and total-to-static

efficiency at on-design and off-design points. Kus [48] studied oil-free turbo-compressors by using CO<sub>2</sub> as the refrigerant for the refrigeration system application in his Ph.D. dissertation. He developed a 1-D code for turbo-compressors predicting the efficiencies of machines for a wide range of operations. He also proposed a non-standard method for partially admitted radial compressors. In 2016, KAIST [49] developed a 1-D meanline code, KAIST\_TMD, with ideal-gasbased loss models and conducted sensitivity analysis. They studied the effect of various calculation methods of stagnation temperature and pressure on the stagnation properties, the impeller's geometry, and performance prediction of an s-CO<sub>2</sub> compressor operating close to the critical point for a 1 MW<sub>th</sub> s-CO<sub>2</sub> Brayton cycle. They showed that choosing an appropriate method of static to stagnation conversion is critical because of the non-linear behavior of density and specific heat ratio, and the corresponding effects on the geometry and performance of the compressor close to the critical point. The researchers in KAIST also mentioned that the definition-based conversion method is the most accurate and was considered as a basis for comparison; however, this method requires significant computation time. Further, they reported a lower conversion error of the real gas isentropic exponent compared to the ideal-gas-based relation.

In general, the total to static conversion can be carried out by using the definition based (Eq. (3)), ideal gas based (Eq. (4)), or real gas isentropic exponent based (Eq. (5)) [49, 51] as follows:

$$h_0 = h_s + \frac{v^2}{2} \tag{3}$$

$$\frac{p_0}{p_s} = \left(1 + \frac{\gamma - 1}{2}M^2\right)^{\frac{\gamma}{\gamma - 1}} \quad ; \quad \frac{T_0}{T_s} = 1 + \frac{\gamma - 1}{2}M^2 \tag{4}$$

$$\frac{p_0}{p_s} = \left(1 + \frac{n_s - 1}{2}M^2\right)^{\frac{n_s}{(n_s - 1)}} \quad ; \quad \frac{T_0}{T_s} = \left(1 + \frac{n_s - 1}{2}M^2\right)^{\frac{m_s n_s}{(n_s - 1)}} \tag{5}$$

where  $n_s$  and  $m_s$  are isentropic exponents and defined as follows:

$$n_s = \frac{\gamma}{\beta_T p}$$
 , where  $\beta_T = \frac{1}{p} - \frac{1}{Z} \left(\frac{\partial Z}{\partial p}\right)_T$  (6)

$$m_s = \frac{\gamma - 1}{\gamma} \cdot \frac{\beta_T p}{\beta_p T}$$
 , where  $\beta_p = \frac{1}{T} + \frac{1}{Z} \left(\frac{\partial Z}{\partial T}\right)_p$  (7)

$$m_s = \frac{\gamma - 1}{\gamma} \cdot \frac{\beta_T p}{\beta_p T} \quad , \quad where \quad \beta_p = \frac{1}{T} + \frac{1}{Z} \left(\frac{\partial Z}{\partial T}\right)_p \tag{8}$$

where  $\beta_T$  and  $\beta_p$  are the isothermal and isobaric compressibility of the fluid.

Several studies were also conducted by using CFD analysis of s-CO<sub>2</sub> compressors to better understand the behavior of supercritical carbon dioxide in the compressors and to develop highefficiency compressors. Pecnik et al. [52] performed a CFD analysis of a 3-D impeller of a centrifugal compressor employed in the Sandia test facility. They wrote a C++ CFD code to solve the compressible Faver-averaged Navier Stokes equations for a simplified impeller without considering the tip clearance and vaned diffuser. They analyzed the performance of the computational results with the experiment from Sandia and reported that their results overpredict the head coefficient due to the simplifications they made in their study. Monje et al. [53, 54] developed a procedure for the compressor design. He developed a 1-D in-house code and designed impellers for a 10 MW supercritical CO<sub>2</sub> power generation cycle. He also performed CFD analysis to study the effect of boundary layer refinement and clearance gap on the computational burden of simulation. He reported that when the  $k-\omega$  SST turbulence model is used for a no-clearance-gap case the simulation was unstable. He compared his CFD results with 1-D in-house code and concluded that the  $k-\varepsilon$  realizable turbulence model could provide a stable and satisfactory result for the case of no mesh refinement.

Shao et al. [55] defined Condensation Margin (CM) and Inlet Velocity Ratio (IVR) to study the possibility of condensation in a low-flow s-CO<sub>2</sub> compressor. They developed a correlation for the calculation of impeller outlet height as a function of the meridional velocity coefficient,

tangential velocity coefficient, and the number of blades. They also simulated a low-flow s-CO<sub>2</sub> compressor with a mass flow rate of approximately 3 kg/s to validate their design procedure with commercial CFD software, NUMECA. Matos [56] used ANSYS CFX for the preliminary design and development of an s-CO<sub>2</sub> centrifugal compressor for a 10 MWe power plant in his thesis. He utilized a partial dynamic similarity, and scaling analysis to introduce a projection methodology with the aim of predicting the operation points of an s-CO<sub>2</sub> compressor map in the non-ideal gas region (close to the critical point) in terms of pressure ratio and flow coefficient from a generalized compressor performance map. In this method, Reynolds numbers do not match in the similarity model because the impeller diameter is fixed, and only speed and flow coefficients were similar between the non-ideal design point and the ideal-gas region design point (in the supercritical region); hence, it was estimated to be partially dynamically similar. He also generated the generalized compressor performance map based on the assessment of enthalpy rise, flow, and speed coefficients for a design point far from the critical point. GE Global Research Center [57] also studied the aerodynamic behavior of s-CO<sub>2</sub> inside a compressor with an inlet guide vane at three operating conditions. They utilized the TACOMA CFD tool by considering real gas effects and could capture a condensation region close to the impeller leading edge. They noticed that the condensation increases as the operating point of the compressor gets closer towards the choke. They concluded that the sharp drop in the speed of sound in the two-phase region resulted in the shock generated at the middle section of the chord.

Ameli et al. [58] studied the possibility of condensation by utilizing classical nucleation and droplet growth theories inside a converging-diverging nozzle, and they estimated the residence time and the completion time. They concluded that since the residence time is twelve times bigger than the droplet formation time, the condensation will take place in a CO<sub>2</sub> compressor operating

near the critical point. Ameli [58, 59] developed a meanline code on the basis of enthalpy loss models and compared his result with the VISTA CCD and CFD results. Ameli et al. [59, 60] also studied the effect of the skin friction coefficient estimation on the evaluation of total-to-total efficiency and compared it with the experimental results of Sandia's compressor. The loss studies he conducted on Sandia's compressor showed that more than half of the total losses occurred in a compressor are due to the skin friction loss originating from the small size of the compressor working close to the critical point. Saravi and Tassou [61] employed ANSYS CFX to study the behavior of supercritical CO<sub>2</sub> in three regions: liquid-like, gas-like, and pseudocritical (Widom). They used the same impeller as the one utilized by Sandia and they reported that a higher pressure ratio could be achieved if the compressor operates in the liquid-like region. They also noticed that the density and speed of sound of CO<sub>2</sub> fluctuate in the pseudocritical region.

### 2.4. S-CO<sub>2</sub> Compressor Design Challenges

There are some major problems in the way of developing s-CO<sub>2</sub> compressors. The main issue in the design process is the operating point of the compressor at the inlet close to the critical point. The critical point is a point in a phase diagram beyond which  $(T > T_c \& P > P_c)$  there is no boiling phenomenon and heating of a liquid generates vapor without boiling process in a smooth transition [62]. That is, the vapor and liquid phases are indistinguishable in the supercritical region,. As demonstrated by Imre et al. [63], the supercritical region is divided into three sections, liquid-like supercritical, gas-like supercritical, and Widom (pseudocritical), as shown in Figure 4. This figure also shows the stability limit of vapor-liquid which is termed spinodal. The regions between spinodals and the vapor-pressure line are Metastable regions. In the Metastable states, some hysteresis takes place inducing difficulties in the CO<sub>2</sub> processing [64], i.e., boiling or condensation could happen at any moment. While the spinodals terminated at the supercritical

point, its effect can be seen in the Widom lines. Hence, it is very important to choose the design point such that to avoid the pseudocritical region for the stable operation of an s-CO<sub>2</sub> compressor.

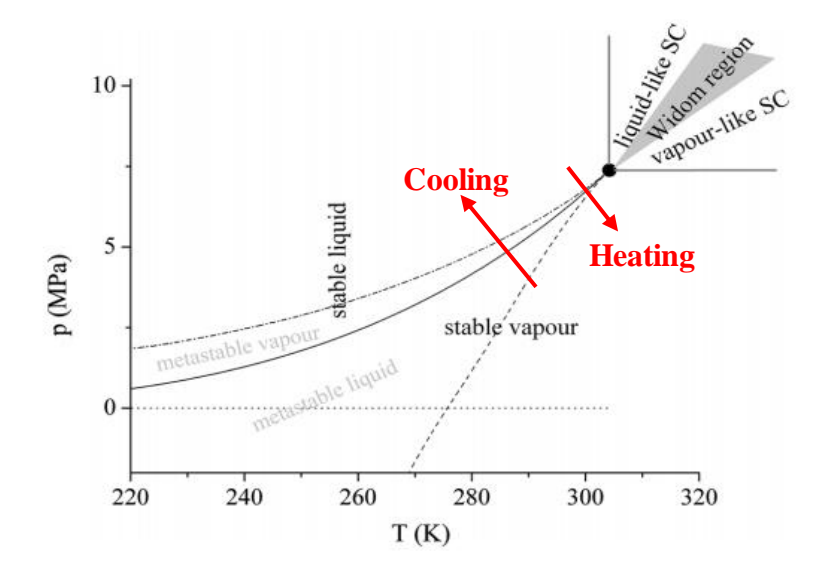


Figure 4: Phase diagram of CO<sub>2</sub> (without solid phase) [63].

The thermophysical properties of CO<sub>2</sub> depend on temperature and pressure strongly resulting in abrupt changes in the properties. As discussed in previous studies such as Ahn et al. [8], Schroder [16], Monge Brenes [54], Matos [56], Ameli et al. [58], and Li et al. [65], there is a substantial variation in density, specific heat, specific heat ratio and other fluid properties at and close to the critical point, as shown in Figure 5.

A compressor working in the vicinity of the critical point (304.13 K, 7.38 MPa) has both advantages and disadvantages. On one hand, the low compressibility factor of CO<sub>2</sub> at the inlet of the compressor implies that the gas behaves like a liquid. This will result in the lower compression work required to reach a certain pressure ratio and higher thermal efficiency of the power cycle. On the other hand, the properties do not behave like an ideal gas and there are sharp changes in properties with small changes in temperature or pressure. Unlike the ideal gas behavior whose properties only depend on the temperature, the real gases are dependent not only on the temperature

but also on the pressure. This non-linear behavior of the real gas properties in close proximity to the critical point also resulted in some challenges when CFD simulations are utilized to study the behavior of carbon dioxide at the entrance of the compressors.

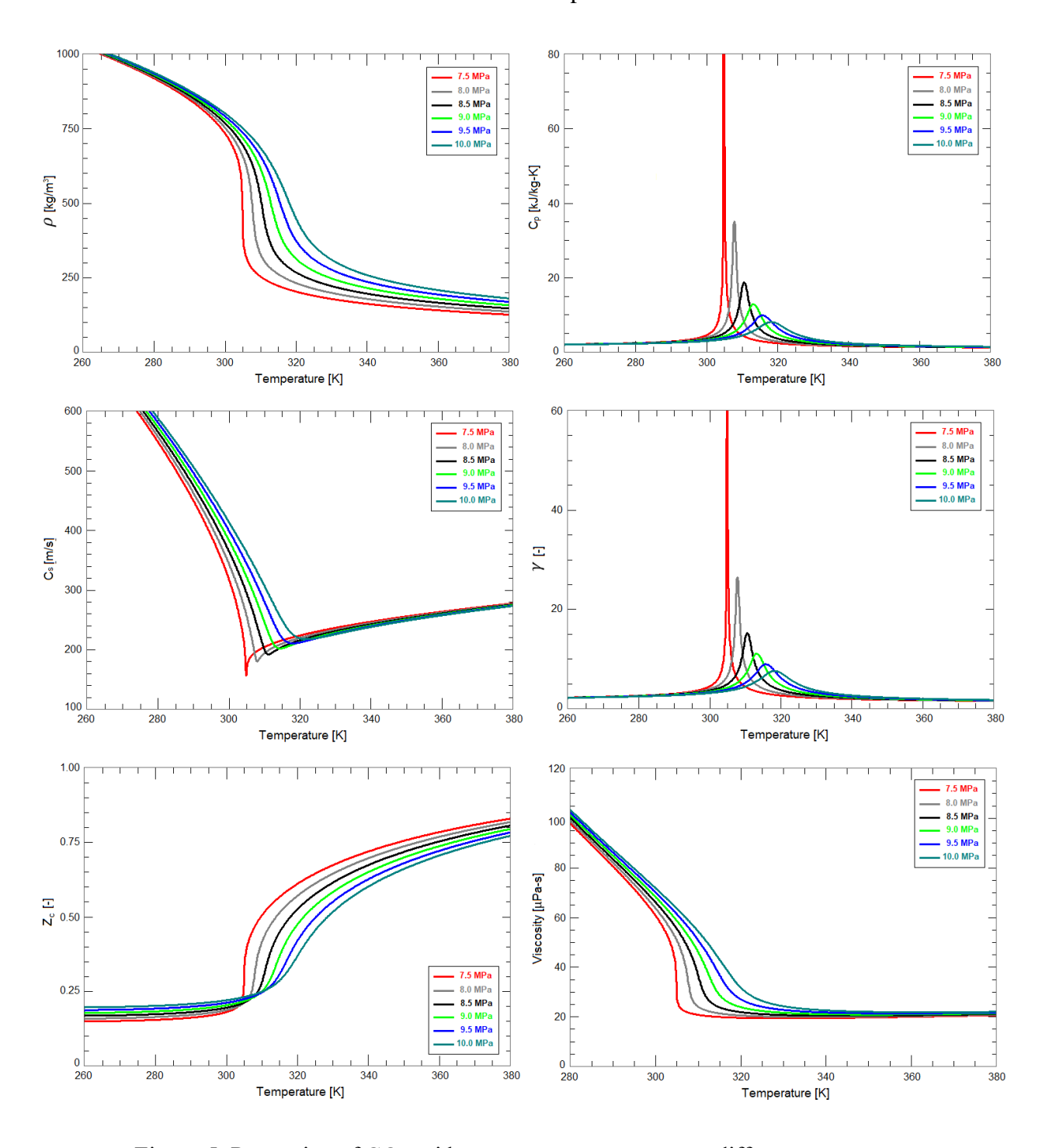


Figure 5: Properties of CO<sub>2</sub> with respect to temperature at different pressures.

Further, since the inlet conditions of the compressors are quite close to the critical point, the condensation occurring at the impeller compounds the convergence issues and makes the CFD simulation a more difficult task to address for the s-CO<sub>2</sub> compressors. The convergence difficulty was also reported in previous studies such as Schroder [16], Monge Brenes [54], Matos [56], and Ameli et al. [66]. In these studies, they used REFPROP real gas properties to simulate low-flow s-CO<sub>2</sub> compressors, less than 500 kWe, by either defining lower limits for temperature and pressure (Monge Brenes [54]) or by considering the inlet condition of the s-CO<sub>2</sub> far from the critical point (Li et al. [39], Utamura et al. [45], Baltadjiev [51], Matos [56], Saxena et al. [57], Saravi and Tassou [61], Hacks et al. [67]) to prevent condensation at the inlet of the compressors in their CFD simulations. Li et al. [65] were also proposed a new method by introducing a maximum swallowing capacity concept to restrict the relative Mach number at the inlet of the impeller. However, they reported that this methodology is not suitable for compressors requiring a high choke margin.

These challenges generated a strong motivation to design and study a compressor to operate in a 10 MWe s-CO<sub>2</sub> Brayton cycle as close as possible to the critical point by utilizing CFD tools for this problem. Thus, the aim of this work is to design an s-CO<sub>2</sub> compressor to get solved smoothly, without any convergence problem, by considering two-phase flows in the compressor to better understand the aerodynamic behavior inside the s-CO<sub>2</sub> compressor and to investigate the effect of condensation on the performance of the s-CO<sub>2</sub> compressor.

# CHAPTER 3: CHALLENGES TO DEVELOP S-CO<sub>2</sub> GAS TURBINES

### 3.1. Introduction

While developing and building an s-CO<sub>2</sub> power cycle is highly interesting and promising, several challenges required to be addressed. As shown in Figure 5, the thermodynamic properties of carbon dioxide are quite non-linear in the vicinity of the critical point. This implies that an appropriate real gas must be utilized to predict the aerodynamic of CO<sub>2</sub> in the compressor. Furthermore, employing supercritical CO<sub>2</sub> as the working fluid in a power cycle results in the challenges associated with developing and designing high-pressure and -temperature heat exchangers, compressors, turbines, recuperators, and proper bearings and seals. Therefore, it is necessary to develop new or modify the current corresponding hardware to adapt itself to the thermodynamic and other characteristics of the s-CO<sub>2</sub>. This chapter aims to investigate these challenges in more detail.

## 3.2. Appropriate Real Gas Equation of State

As previously shown in Figure 5, there is a drastic change in the thermodynamic properties of CO<sub>2</sub> near the critical point. The nonlinearity creates instability in the CFD simulation and causes convergence challenges. This behavior is mainly due to the deviation of CO<sub>2</sub> from the ideal gas as a result of the low compressibility factor of 0.27 near the critical point. This will result in unclarity in terms of the accuracy of traditional design methodology and recommendations for ideal gas compressors. In other words, the challenge of the unusual behavior of the gas near the critical condition implies that an appropriate equation of state is also required for not only compressor design procedure but also for numerical simulations [68]. This implies that the real gas properties must be employed in the analysis and CFD simulations.

In the last 50 years, equations of state for pure component CO<sub>2</sub> and its mixtures at high temperatures and high pressures have been widely investigated because of its important role in geological and petroleum science. Despite these investigations, finding a thermodynamic model that accurately predicts the s-CO<sub>2</sub> behavior is difficult because most of the equations of state are inaccurate in predicting the CO<sub>2</sub> properties near its critical point. Furthermore, some equations only focus on the accurate representation of pressure-volume-temperature (P-v-T), and thus, not enough attention has been paid to physical consistency on other properties such as enthalpy, heat capacity, speed of sound, etc. Recently, Zhao et al. [69] studied equations of state: Peng-Robinson (PR); Peng-Robinson with Boston-Mathias alpha function (PR-BM); Soave modified Redlich-Kwong (SRK); Lee-Kesler-Plöcker (LKP), Benedict-Webb-Rubin modified by Starling and Nushiumi (BWRS) and the Span-Wagner (SW). Their investigation showed that the Span Wagner equation of state is the most accurate model in the subcritical, supercritical, and critical regions of CO<sub>2</sub>.

The SW equation of state (EOS) covers the thermodynamic properties of CO<sub>2</sub> for the pressure ranges extending to 800 MPa and from the triple point temperature up to 1100 K [70]. This EOS utilizes a functional equation in the Helmholtz free energy explicitly. REFPROP [26] is a software developed by the National Institute of Standards and Technology (NIST) which calculates transport and thermodynamic properties based on the SW equation of state. In the current work, REFPROP v.10 will be employed for the simulation purpose to generate the real gas property (RGP) table for CO<sub>2</sub> to be imported into the ANSYS CFX.

## 3.3. Current Components Needing Changes for Use in S-CO<sub>2</sub> Brayton Cycle Application

### 3.3.1. Compact Heat Exchangers

In general, the type of heat exchanger, design, material choice, and cost are the essential parameters in developing a heat exchanger (HE). In the s-CO<sub>2</sub> Brayton cycle, heat exchangers play important roles in the cycle efficiency. Heat transfer behavior is significantly different for s-CO<sub>2</sub> HEs compared to the HEs which use a constant property fluid. Two main challenges in the design and development of s-CO<sub>2</sub> HEs are as follows [71]:

- 1- Enduring high temperatures and pressures whilst keeping it compact; and
- 2- Opting for suitable HE types to compromise with the performance, durability, and cost. Ahn et al. [8] assessed the recuperator size of different s-CO<sub>2</sub> Brayton cycle layouts by employing LMTD (Log Mean Temperature Difference) method. They realized that while the popular recompression cycle is the most efficient layout, the recuperator of this power cycle is the largest based on the estimation of UA ratio quantity (overall heat transfer rate multiplied by the heat transfer area compared to the recuperation cycle), as shown in Figure 6. Therefore, an important characteristic of the heat exchangers is the surface area density which evaluates the compactness of HEs. In general, if the ratio of the contact surface to the volume reaches 700 m<sup>2</sup>/m<sup>3</sup>, it is considered compact [72]. This means that the size of the heat exchanger is small and the heat transfer coefficient is large which is favorable for high-pressure applications. In the case of supercritical CO<sub>2</sub>, since the dynamic viscosity of CO<sub>2</sub> is similar to gas and the density of this operating fluid is akin to liquid, this will result in a high Reynolds number improving the heat transfer as well.

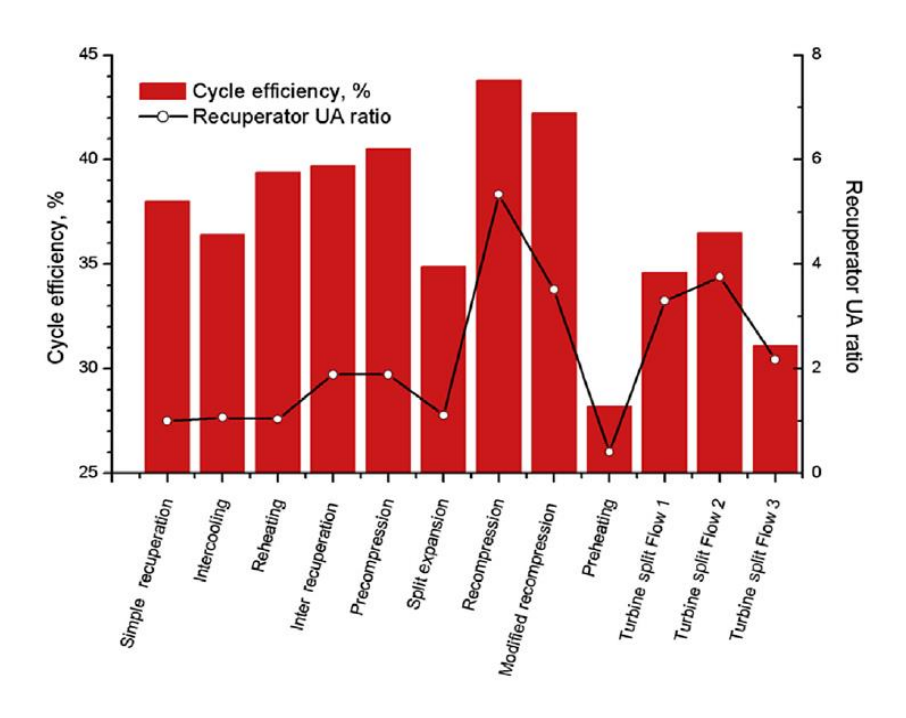


Figure 6: Estimation of the size of heat exchangers for different Brayton cycle layouts including their cycle efficiencies [8].

The heat exchangers appear in three forms in the power cycles: a recuperator which transfers the remaining energy from the exit of the turbine to the exit of the compressor for energy recovery purposes, a heater which absorbs energy from the heat source, and a cooler which removes energy from the cycle and transfers it to the environment. The currently available heat exchangers were compared in terms of maximum pressure, temperature, and surface area density in Table 2.

Table 2: Capabilities of various heat exchangers [72].

Heat Exchanger Type	Maximum surface area density	P <sub>max</sub>	$T_{max}$
	$[m^2/m^3]$	[MPa]	[°C]
Shell and tube	100	30	900
Diffusion-bonded plate-fin	800	20	500
Brazed plate-fin	1500	9	500
Micro shell and tube	2000	40	650
Printed Circuit	2500	40	900

One of the major challenges in designing an s-CO<sub>2</sub> Brayton cycle is designing and developing compact, efficient, and cost-effective recuperators which can also operate in high temperatures and pressures. Printed circuit heat exchangers (PCHEs) are well-established and commonly used as a recuperator, and high-temperature heater in the CO<sub>2</sub> Brayton power cycles. They are popular because they are compact, and extremely efficient [73, 74]. A typical PCHE including its diffusion-bonded core is shown in Figure 7.



Figure 7: A typical Printed Circuit Heat Exchanger (PCHE) [74].

Since PCHEs are manufactured through a diffusion bonding process, they are immensely strong and feature high performance. The flow channels of PCHEs are joined together with metal flat plates through either a chemically etched or pressed process [71]. Then the etched plates are stacked together to make a high-integrity block [75]. This process makes the core of the heat exchanger free of joints, welds, or points of failure [76]. The geometry of etched flow channels is manufactured in various shapes such as straight, zigzag, s-shaped fins, and airfoil fins, as shown in Figure 8.

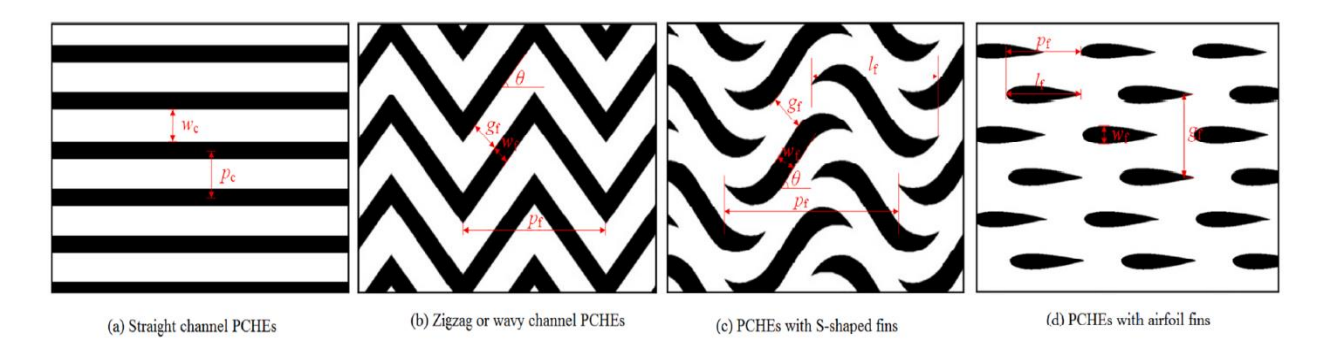


Figure 8: Different flow channels: (a) straight, (b) zigzag (or wavy), (c) s-shaped fins, and (d) airfoil fins [71].

Generally, the challenges of employing compact heat exchangers for s-CO<sub>2</sub> applications are manifold. One of the main challenges of using high-performance CHEs is the expensive production processes of diffusion bonding and chemically-etched channels because the surfaces of all plates should be perfectly clean to have successful diffusion bonding [75]. Clarson et al. [77] also reported that a typical PCHE will fail in 300 to 800 complete cycles and could fail in 200 complete cycles in case of severe thermal transient conditions. Fouling is also another challenge that compact heat exchangers are facing. Fouling is the material build-up in the fluid channels decreasing the thermal performance and increasing the hydraulic resistance in the HE [78], as shown in Figure 9. It is worth mentioning while CO<sub>2</sub> is the operating fluid in both streams of the recuperators (high-pressure and low-temperature stream on one side, and high-temperature and low-pressure flow on the other side), molten salt is utilized in the heaters and coolers as the processing fluid which compounds the problem. In the case of plugging, the cleaning process of the compact heat exchangers (PCHEs) is also a challenge because of the complicated geometry of the channels and due to the welded body from the core to the header.

In addition, the heat transfer behavior in the pseudocritical region is quite different from the heating and cooling modes of operation of a heat exchanger using constant property fluid because of the abnormal thermophysical properties inside the boundary layer [39]. Moreover, although

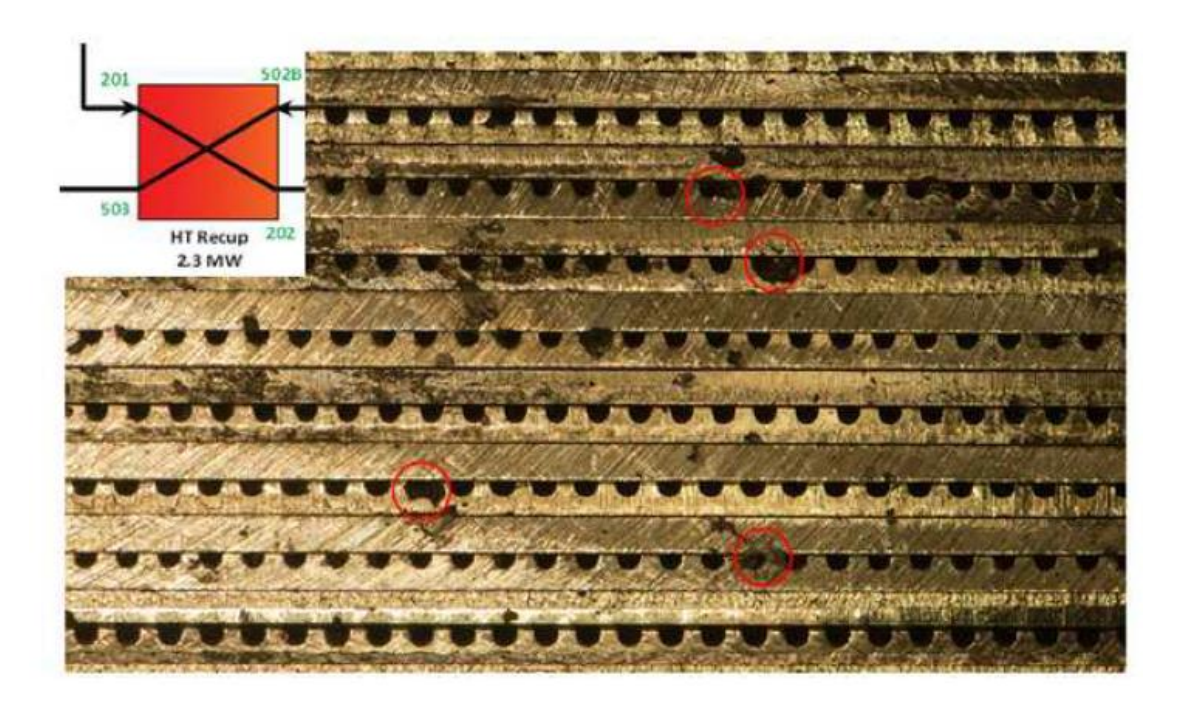


Figure 9: Fouling and possible plugging of channels in a recuperator [78].

compact HEs have high heat transfer performance, high-pressure drops are inevitable due to the non-straight and longer passages [71]. Last but not least, there is a pinch point issue that needs to be considered in the design of compact recuperators. A pinch point is a location in a heat exchanger where the temperature difference between hot and cold streams is minimum because of the substantial difference between the fluids of both streams. As this minimum temperature difference becomes close to zero, the heat transfer rate and subsequently the performance of the recuperator will decrease, and part of the energy would not get recovered as shown in Figure 10. In simpler terms, when there is a pinch point in the HE, the heat transfer in the hot stream (to get cold) is decreased resulting in a higher temperature at the exit (higher than the design value) implying surplus heat at the exit of the hot stream. On the other hand, the heat transfer in the cold stream (to get hot) is also decreased leading to a lower temperature at the exit (lower than the design value), implying a deficit at the exit of the cold stream.

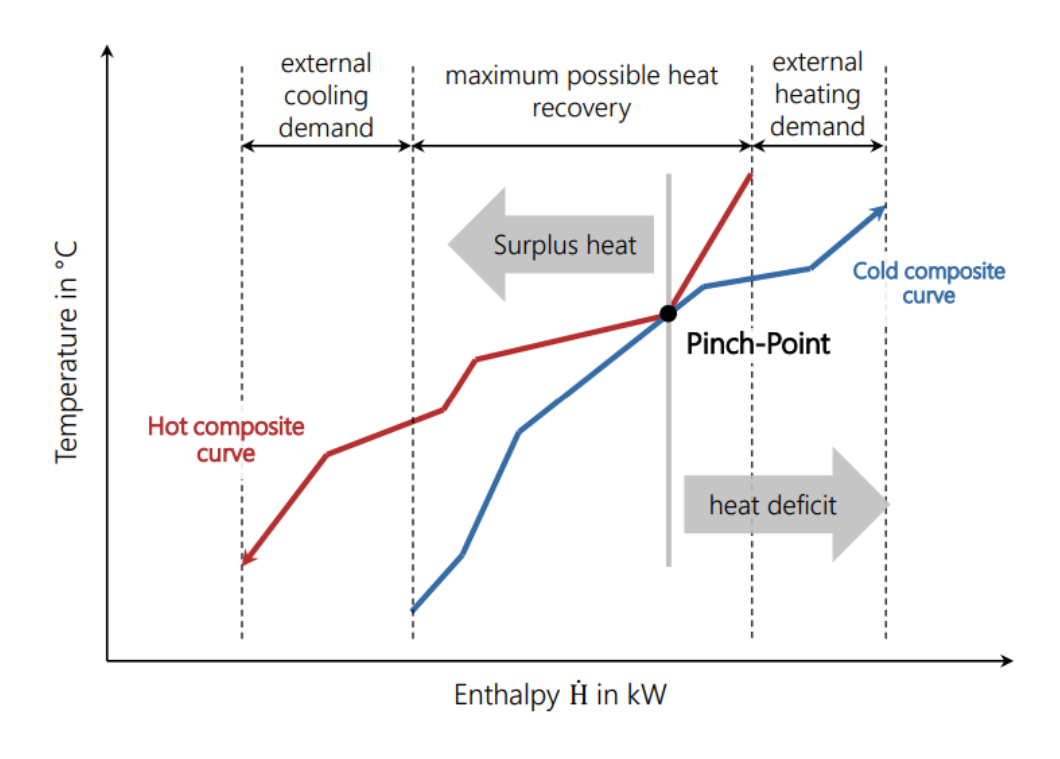


Figure 10: Pinch point in a heat exchanger [79].

## **3.3.2.** Compressors and Turbines

In an s-CO<sub>2</sub> power cycle, at least two turbomachines are required: a compressor/pump and a turbine. In a more advanced power system, more compressors or turbines might be utilized. For instance, in the recompression cycle, which is known as the most efficient s-CO<sub>2</sub> Brayton cycle layout, a recompressor is also employed along with the main compressor and turbine. Unlike the recompressor and turbine operation region, which is far from the critical point, the main compressor of the s-CO<sub>2</sub> Brayton cycle works close to the critical point in either the liquid-like or vapor-like region. Hence the design of the main compressor for an s-CO<sub>2</sub> Brayton cycle requires special attention because of the non-linear behavior of thermodynamic properties near the critical point.

Turbines and compressors can be designed in either form of radial/centrifugal or axial. In a centrifugal turbomachine, the fluid enters the machine parallel to the shaft end exit in the radial

direction, i.e., the flow turns 90°. However, in an axial turbine or compressor, the flow enters and exits parallel to the shaft. Multi-stage axial turbomachinery can be readily installed on a single shaft; on the other hand, centrifugal/radial type generates a higher enthalpy change in a single stage due to the change of radius from the inlet to the outlet, along the flow path [71]. Further, while the centrifugal/radial machines have higher efficiencies in small-scale applications, the multi-stage axial design provides higher efficiencies for large-scale (high mass-flow) power systems.

While the fundamentals of designing conventional compressors and turbines are quite established, little is known about the operational range and design procedures of the s-CO<sub>2</sub> turbomachinery. There are three major compressor development challenges [80]:

- 1- Thermodynamic properties: appropriate equation of state, and relations between stagnation and static properties.
- 2- Aerodynamic design: compressor designers feel that at the critical point, s-CO<sub>2</sub> shows some unusual characteristics never considered before in compressor design, such as the strong variation in the ratio between specific heats and the low compressibility factor of the gas. This leads to the uncertainty, of whether the compressor should be designed according to the well-established guidelines for pumps or ideal gas compressors or whether a new theory is needed.
- 3- Numerical simulation and testing challenges.

#### **3.3.2.1.** Thermodynamic Challenges

Currently, there is no specific design method for the s-CO<sub>2</sub> compressor. Wrongly, conventional air compressor design data and methods are primarily used for the initial s-CO<sub>2</sub> compressor design and parameter estimation. Unlike air, the thermodynamic properties of s-CO<sub>2</sub> are dominated by real gas effects, especially near the critical point region because the flow

properties are extremely sensitive to slight temperature and pressure changes in this region. For instance, at the pressure of 7.4 MPa, a 0.2 °K increase in temperature from 303 °K to 303.2 °K will result in a 186.58 (kg/m³) drop in density and a 33.78 (kJ/kg-k) increase in specific heat. Currently, there is no clear characterization or description of the real gas effect of s-CO<sub>2</sub> on the internal flow behavior of the compressor. Because of the lack of thermodynamic understanding, many preliminary designs that use the traditional Balje method are based on the specific speed (Ns) and specific diameter (Ds), and throughflow models; however, they do not agree well with the experimental data.

Further, conventional compressor design relies on several loss models to predict efficiency and other performance parameters. For air, most of the empirical equations are based on decades of studies on air compressors, and it is still unclear the applicability of the loss models based on air experimental data for the s-CO<sub>2</sub> compressor as it operates near the critical point.

All these challenges are associated with the unique thermodynamic feature of the s-CO<sub>2</sub>; therefore, more dedicated research efforts are required.

#### 3.3.2.2. Aerodynamic Design Challenges

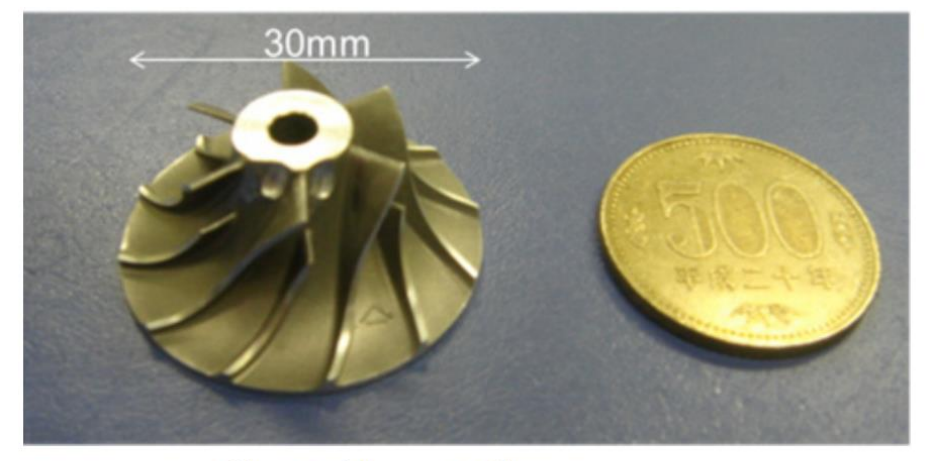
The primary advantage of the supercritical CO<sub>2</sub> system is the high-density feature leading to compact turbomachinery design. However, this advantage creates a serious challenge for compressor sizing. The s-CO<sub>2</sub> is extremely dense such that a compressor as small as 60 mm in overall diameter requires as much as 1 MW of electrical power to drive it. This small size also means a narrower flow channel, i.e., higher friction loss and higher leakage losses which are believed to be the main source of loss for an s-CO<sub>2</sub> compressor. The high density will also generate a high aerodynamic loading force affecting the compressor shaft, bearing, and hub size design. Since the thermodynamic properties are very sensitive near the critical point, the compressor

should be designed with a wide operation range and an advanced anti-surge system. So far, most of the compressor research has focused on simple unshrouded centrifugal impellers, but there is still no clear answer to which type of impeller configuration is more suitable for s-CO<sub>2</sub> applications, namely axial or centrifugal compressor, shrouded or unshrouded. Each configuration has its advantages and disadvantages that require further investigation.

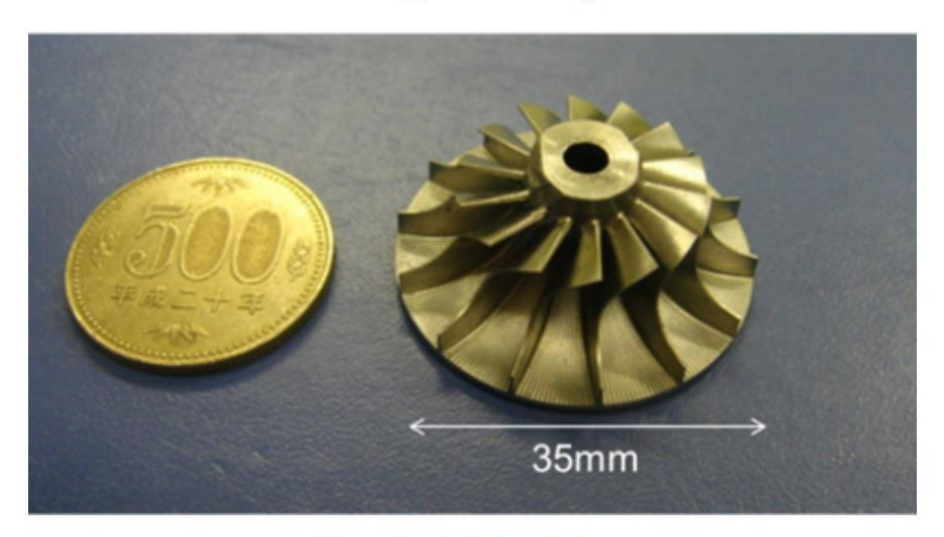
#### 3.3.2.3. Numerical Simulation and Testing Challenges

Numerical simulation is a powerful tool to understand compressor flow physics; however, it is a difficult task to simulate supercritical and two-phase flow simultaneously in the current commercial codes. Therefore, some open-source codes most likely work better for an accurate simulation. The open-source software provides enough flexibility for s-CO<sub>2</sub> compressor design, but more dedicated efforts are needed for algorithm development. At this point, because of the high energy consumption and size ratio, it is impossible to study the internal flow field of any s-CO<sub>2</sub> compressor experimentally in university labs. Figure 11 shows an example of a lab-scale s-CO<sub>2</sub> compressor from the Tokyo Institute of Technology for a 10-kW power cycle test facility. Additionally, traditional similitude laws based on ideal gases or liquids cannot be implemented for real gases such as s-CO<sub>2</sub>. Therefore, experimental testing is limited to three major results only: overall performance measurements, dynamic loading measurements, and operating range measurements. Also, it is important to maintain pure CO<sub>2</sub> conditions during the experiment since the mixture with water or oxygen will significantly affect the flow physics near the critical point.

It is worth noting that most of the compressors and turbines that have been either tested or under development up to the present time are not designed for reasonable commercial scales (10 MWe or higher). In other terms, the challenges that researchers have faced for the small-scale turbomachinery test and developments to date might be unnecessary for developing a large-scale



**Centrifugal Compressor** 



**Radial Turbine** 

Figure 11: The lab-scale compressor and turbine examples from the Tokyo Institute of Technology [45] for a 10 kW Brayton cycle.

s-CO<sub>2</sub> test facility. For this reason, more research is required to understand the aerodynamics and the challenges inside s-CO<sub>2</sub> turbomachinery.

## 3.3.3. New Seals, Bearings, and Other Design Considerations

While the high density of supercritical CO<sub>2</sub> brings some benefits, it also introduces some challenges in the design process of an s-CO<sub>2</sub> power cycle. The denser fluid compared to the conventional Brayton cycle result in compact turbomachinery design. However, they also entail

operating at high speeds to keep the isentropic efficiency of the machine high for multi-Megawatt power cycles [71]. The high rotational speed of compact impellers will result in higher aerodynamic losses including windage, and tip clearance losses. Further challenges are also introduced in the design of bearings, seals, and shafts for turbomachines working under high pressures and temperatures. So, selecting appropriate types of bearings and seals, materials, coating technologies and their compatibility with high temperatures and pressures become of high importance. Furthermore, challenges associated with rotordynamic analysis must be considered.

In general, rotordynamic analysis is related to the study of rotors which are supported by stators (bearings). As the rotational speed increases, the amplitude of vibration often crosses a maximum value known as critical speed. Normally, this amplitude increases by imbalance of the rotating component [81]. In this regard, a stable rotordynamic behavior in the high operating speeds will be also a challenge.

Regarding the challenges related to the bearings, there is a considerable pressure difference across a single-stage turbine and compressor also creates a new challenge in terms of the mechanical design of turbine blades, and turbine housing [71]. It will also lead to difficulty in controlling the axial thrust applied on the bearing and result in leakage to the surrounding when the turbomachine is radial.

It is worth mentioning that s-CO<sub>2</sub> also functions as a solvent, so any lubrication oil can introduce contamination into the system. Thus, new advanced bearing designs such as oil-free compliant foil bearing (CFB) and magnetic bearing have been proposed for high speeds (75,000 RPM) to intermediate speeds (~12,000 RPM) ranges of application in s-CO<sub>2</sub> turbomachines. In oil-free bearings, speed and temperature are not limitations leading to the improvement of turbomachinery performance [82]. Accordingly, Chapman [83] designed an oil-free foil bearing

in which s-CO<sub>2</sub> is used as the lubricating fluid, as shown in Figure 12. Alternatively, active magnetic bearings (AMB) technology controls the bearing behavior through an electronic system, as shown in Figure 13. These bearings support the rotor without any contact, lubrication, or wear [48]. Therefore, magnetic bearings are also suitable for high-speed compressors, turbines, and jet engines. However, CFB and AMB are in the developing phase and require further optimization and testing.

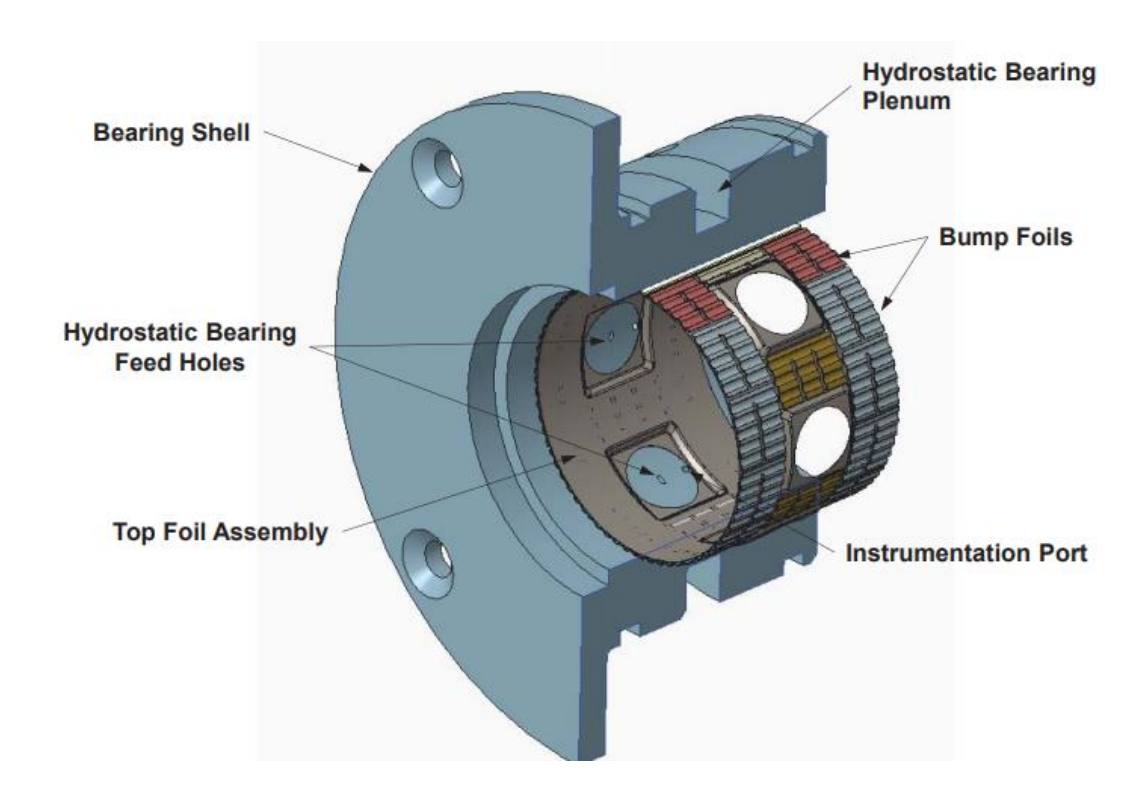


Figure 12: Advanced oil-free compliant foil bearing (CFB) [83].

Generally, to optimize the design of s-CO<sub>2</sub> compressors and turbines to reach high efficiencies, selecting components appropriately is quite crucial. Sienicki et al. [84] studied the technologies required to be employed for an s-CO<sub>2</sub> Brayton power cycle based on the power size of the cycle. They categorized the suitable technologies for the main components including turbine, compressor, bearings, seals, alternator, and shafts, as shown in Figure 14. It can be concluded from

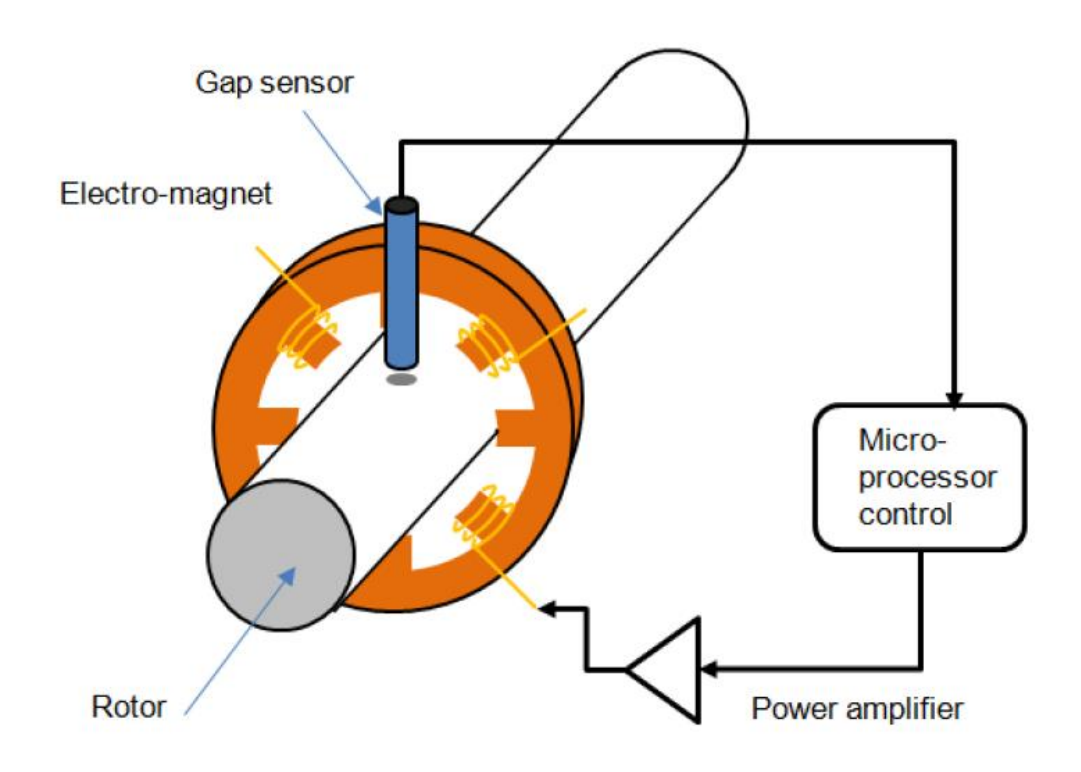


Figure 13: Active magnetic bearing (AMB) system [48].

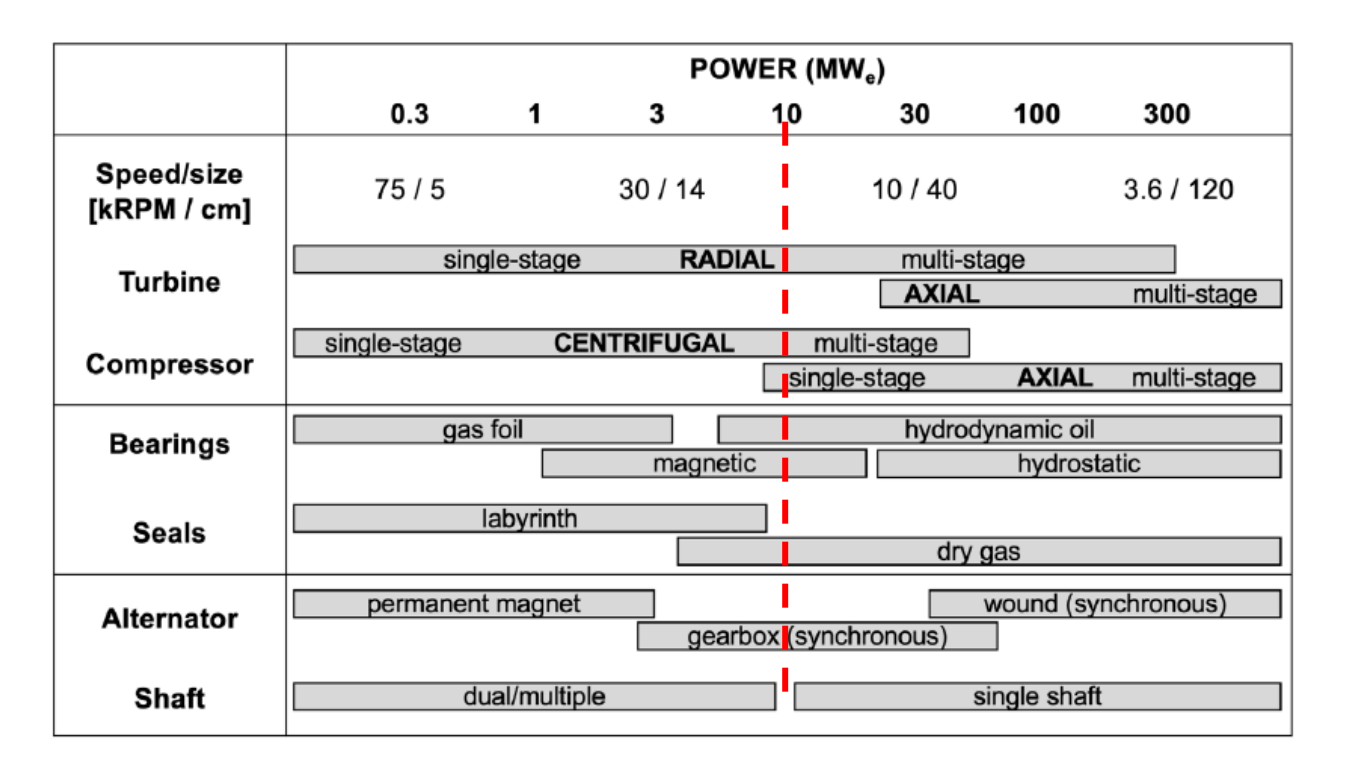


Figure 14: Application range of component and technology options for s-CO<sub>2</sub> Brayton cycle (reproduced by White et al. [71]).

this chart that radial turbines and centrifugal compressors are suitable to be used for a 10 MWe and below power generation with a rotational speed of approximately 20,000 RPM and higher.

## 3.3.4. Current Attempts to Design, Manufacture, and Test S-CO<sub>2</sub> Brayton Cycles

Several attempts have been made over the past decades to design, manufacture, and test the operability and understand the challenges involved in developing a commercialized size of an s-CO<sub>2</sub> Brayton power cycle. As previous studies showed and discussed earlier in this research study, in order to scale up a power generation facility successfully, a reasonable size of 10 MWe or higher needs to be built and tested. Considerable progress has been made in building and testing the components of the systems and few demonstration cycles were also developed or are under development to date. The current development of s-CO<sub>2</sub> facilities was summarized in Table 3.

Sandia National Laboratories (SNL) [34] in conjunction with Barber Nicolas Inc. developed and constructed the first s-CO<sub>2</sub> recompression Brayton cycle to generate 250 kWe operating in a closed-loop layout. The cycle efficiency of their test facility was reported to be 32% at the design condition. Bechtel Marine Propulsion Corporation (BMPC) [33] developed and tested a 100 kWe two-shaft recuperated Brayton cycle to study the controllability and operability of the s-CO<sub>2</sub> cycle. Their test facility could reach the maximum thermal efficiency of 4% due to windage losses. Tokyo Institute of Technology [45] designed and tested a 10-kW recuperated Brayton cycle but the cycle could achieve 110 W power generation. They reported that the windage in the impeller of the compressor was the major source of power loss because of the high range of rotational speed, 30,000 to 85,000 RPM. Korea Atomic Energy Research Institute (KAERI), Korea Advanced Institute of Science and Technology (KAIST), and Pohang University of Science and Technology (POSTECH) jointly designed a 300 kWe simple recuperated s-CO<sub>2</sub> Brayton cycle.

Korea Institute of Energy Research (KIER) has developed three experimental test loops for

Table 3: Current development of s-CO<sub>2</sub> power cycles (Some contents were adapted from [71] and [85]).

Davidanan	Power	Tmax	P <sub>max</sub>	PR	Configuration
Developer	[MWe]	[K]	[MPa]	[-]	— Configuration
SNL [34]	0.25	811	13.8	1.8	Recompression, indirect
BMPC [33]	0.1	572		1.8	Recuperated, indirect
Tokyo Institute of Technology [45]	0.01	550	11.9	1.45	Recuperated, indirect
KAERI/KAIST/POSTECH [86]	0.3	773	20	2.57	Recuperated, indirect
	0.001	473	13	2.27	Recuperated, indirect
KIER [87]	0.01	453	13	1.65	Simple
	0.12	865	13.5	1.5	Simple
NET Power [88, 89]	50 (MW <sub>th</sub> )	1423	30	10	Allam, direct, oxy- fuel combustion
SwRI/GE [37, 38, 90]	1	988	25.5	2.9	Recompression, indirect
Echogen Power System [91]	8	758			Recuperated, indirect
GTI/SwRI/GE (STEP Program) [92]	10	988	25	2.7	Recompression, indirect

the waste heat recovery application. In 2014, they launched a 10 kWe power generation facility to test the operability of small-scale s-CO<sub>2</sub> systems. They also developed a 670 We power cycle in 2016. KIER also built a 120-kW power cycle operating under the transcritical condition in 2018. The main objective of their investigation was to examine the axial-type turbine application in an s-CO<sub>2</sub> cycle to solve the bearing failure of small-scale turbomachinery. NET Power [88, 89] proposed and designed a new cycle termed as Allam cycle operating in a semi-closed loop Brayton cycle to generate 50 MWth power. Allam cycle employs oxy-fuel combustion to generate power within which 100% of CO<sub>2</sub> emission is captured and fed back for sequestration and reuse to control

the maximum temperature in the combustion chamber. They targeted to reach the cycle efficiencies of 59% and 51% (LHV) for natural gas and coal fuels. They also designed a 300 MWe natural gas plant concept for the next step toward the commercialization of the s-CO<sub>2</sub> power plant.

Southwest Research Institute (SwRI) in cooperation with General Electric (GE) developed a 1 MWe recompression s-CO<sub>2</sub> test for the concentrated solar power (CSP) application [37, 38, 90]. Their aim of constructing this power loop was not for demonstration but rather to provide a platform for mechanical testing and measuring the performance of s-CO<sub>2</sub> recuperators and turbines [37]. Echogen Power System [91] developed a 7-8 MW class s-CO<sub>2</sub> heat engine in a modified simple Brayton cycle for waste heat recovery (WHR) and exhaust heat recovery (EHR) applications. The design power cycles include two turbines, one compressor, two PCHE recuperators, and one PCHE cooler. Their initial testing showed that the amount of power generated by the turbine was approximately balanced with the required work for the compressor. That is the net power was approximately 150 kW.

Gas Technology Institute (GTI) leads a program known as STEP in collaboration with Southwest Research Institute (SwRI) in cooperation with General Electric (GE) to construct a 10 MWe s-CO<sub>2</sub> pilot plant [92]. Department of Energy (DOE) has invested \$124 million in the \$155 million STEP project to build the first reconfigurable 10 MWe supercritical carbon dioxide test facility at Southwest Research Institute in San Antonio, Texas campus. This project is ongoing and they plan to launch the plant with the simple recuperated cycle with the maximum temperature of 773 K at the inlet of the turbine and then proceed with the recompression Brayton cycle working at the maximum temperature of 988 K. Building this modifiable cycle which was projected to be finished by December 2024 is one of the first steps to understand the s-CO<sub>2</sub> concept in a reasonable

size of power generation and to move forward toward developing multi-hundred-Mega-Watt power cycles for commercial operations ultimately.

# CHAPTER 4: S-CO<sub>2</sub> BRAYTON CYCLE RECONFIGURATIONS

In this chapter, the simple (conventional) Brayton cycle is considered as the reference cycle, and three well-known closed-loop s-CO<sub>2</sub> Brayton cycles, namely the simple recuperated, recompression, and dual turbine cycles were reconfigured to generate 10 MW electric power. A supercritical CO<sub>2</sub> Brayton cycle design tool was developed in Microsoft Excel coupled with CoolProp real gas NIST database to optimize and obtain the best cycle efficiency and operating conditions for an s-CO<sub>2</sub> compressor working in a 10 MWe power cycle. It should be noted that for the cycle analysis, the following assumptions were made in this chapter:

- 1- The pressure drops (losses) in the cycle are neglected, and
- 2- The behavior of compressors and turbines is real (non-isentropic).

To compare the performance of each cycle in terms of thermal efficiency fairly, similar constraints were utilized for the cycle analysis. The assumptions used for each cycle are listed in Table 4.

Table 4: Cycle design assumptions.

	PR	$P_{0,min}$	$T_{0c,i}$	$T_{0t,i}$	$\dot{W}_{n}$	$\epsilon_{LT}$	$\epsilon_{HT}$	$\eta_{\boldsymbol{m}}$	$\eta_{\text{MC,s}}$	$\eta_{t,s}$
	[]	[MPa]	[K]	[K]	[MW]	[]	[]	[]	[]	[]
Simple	2.7	8.6	310	950	11.11			0.90	0.85	0.90
Simple Recuperated	2.7	8.6	310	950	11.11		0.80	0.90	0.85	0.90
Recompression	2.7	8.6	310	950	11.11	0.78	0.88	0.90	0.85	0.90
Dual Turbine	2.7	8.6	310	950	11.11		0.80	0.90	0.85	0.90

where  $\eta_{c,s}$ ,  $\eta_{t,s}$ ,  $\eta_m$ ,  $\varepsilon_{LT}$ , and  $\varepsilon_{HT}$  are compressor isentropic efficiency, turbine isentropic efficiency, mechanical efficiency, the effectiveness of low-temperature recuperator, and

effectiveness of high-temperature recuperator. These design param eters are defined for, e.g., the recompression cycle as follows:

$$\eta_{MC,s} = \frac{h_{02s} - h_{01}}{h_{02} - h_{01}} \tag{9}$$

$$\eta_{t,s} = \frac{h_{05} - h_{06}}{h_{05} - h_{06s}} \tag{10}$$

$$\eta_m = \frac{\dot{W}_{electric}}{\dot{W}_{net}} \tag{11}$$

$$\varepsilon_{LT} = \frac{h_{03} - h_{02}}{h_{07} - h_{02}} \tag{12}$$

$$\varepsilon_{HT} = \frac{h_{04} - h_{03}}{h_{06} - h_{03}} \tag{13}$$

The primary reasons for the chosen boundary conditions for the compressor, turbine, and recuperators are to capture the benefits of CO<sub>2</sub> close to the critical region (for the compressor) as possible, material consideration (for the turbine), and availability of current technology (for the recuperator). With these assumptions, a complete cycle analysis is performed for each of the cycles considered in this study. The state points for each cycle were calculated and then utilized in the design of the impellers for the compression system. The minimum mass flow rate, input heat, compressor-to-turbine power (back-work) ratio, and thermal efficiency were also calculated for each cycle. Considering the same conditions for all cycles enable us to make direct correlations between the cycles. This similarity allows us to directly observe the benefits and drawbacks of each cycle layout.

## 4.1. Simple (Conventional) S-CO<sub>2</sub> Brayton Cycle

The simple Brayton cycle is typically operating in a closed-loop cycle when the operating fluid is CO<sub>2</sub>, as shown in Figure 15. In this cycle, the cooled supercritical CO<sub>2</sub> at the temperature

and pressure of 310 K and 8.6 MPa enter the compressor to pressurize the working medium up to the maximum pressure of 23.3 MPa. Then the supercritical CO<sub>2</sub> is heated up indirectly in a heat exchanger, or heater, to reach the maximum temperature of the cycle, 950 K. In the turbine, the energy of the fluid is extracted for work generation as it expands. Finally, after expansion occurred in the turbine the working fluid is flowing through a second heat exchanger, cooler, to decrease the temperature of the fluid further before it enters the compressor for the next operation loop.

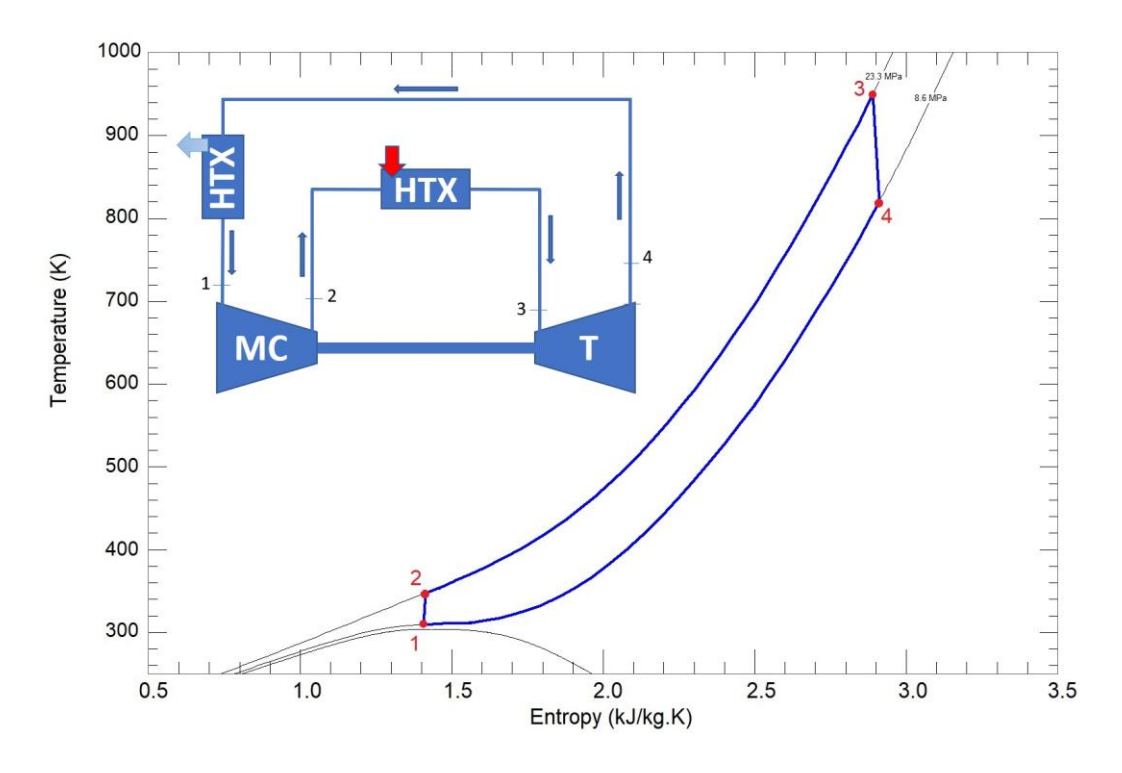


Figure 15: Conventional s-CO<sub>2</sub> Brayton cycle.

## 4.2. Evaluation of Currently Suggested S-CO<sub>2</sub> Brayton Cycles

### **4.2.1. Simple Recuperated Cycle**

The first reconfigured cycle in the s-CO<sub>2</sub> Brayton platform is the simple recuperated cycle. As shown in Figure 16, this cycle includes a compressor, a turbine, a recuperator, and two heat exchangers. Supercritical CO<sub>2</sub> at slightly higher values of temperature and pressure compared to the critical point of CO<sub>2</sub> flows into the compressor to increase the pressure from 8.6 MPa to 23.3

MPa. The recuperator recovers the heat allowing it to transfer most of the heat present at the turbine exit to preheat the s-CO<sub>2</sub> coming out of the compressor and before entering the heat exchanger. The heat exchanger rises the temperature of the working fluid to a maximum of 950 K. Supercritical carbon dioxide expands in the turbine and generates work leading to the temperature and pressure drop. The fluid then passes through the recuperator to not only increase the temperature of the compressor outlet stream but also to pre-cool the s-CO<sub>2</sub> before going into the low-temperature heat exchanger. Lastly, the temperature of the s-CO<sub>2</sub> is cooled to the minimum temperature of 310 K and the cycle maintains. The details of cycle performance parameters are shown in Table 5.

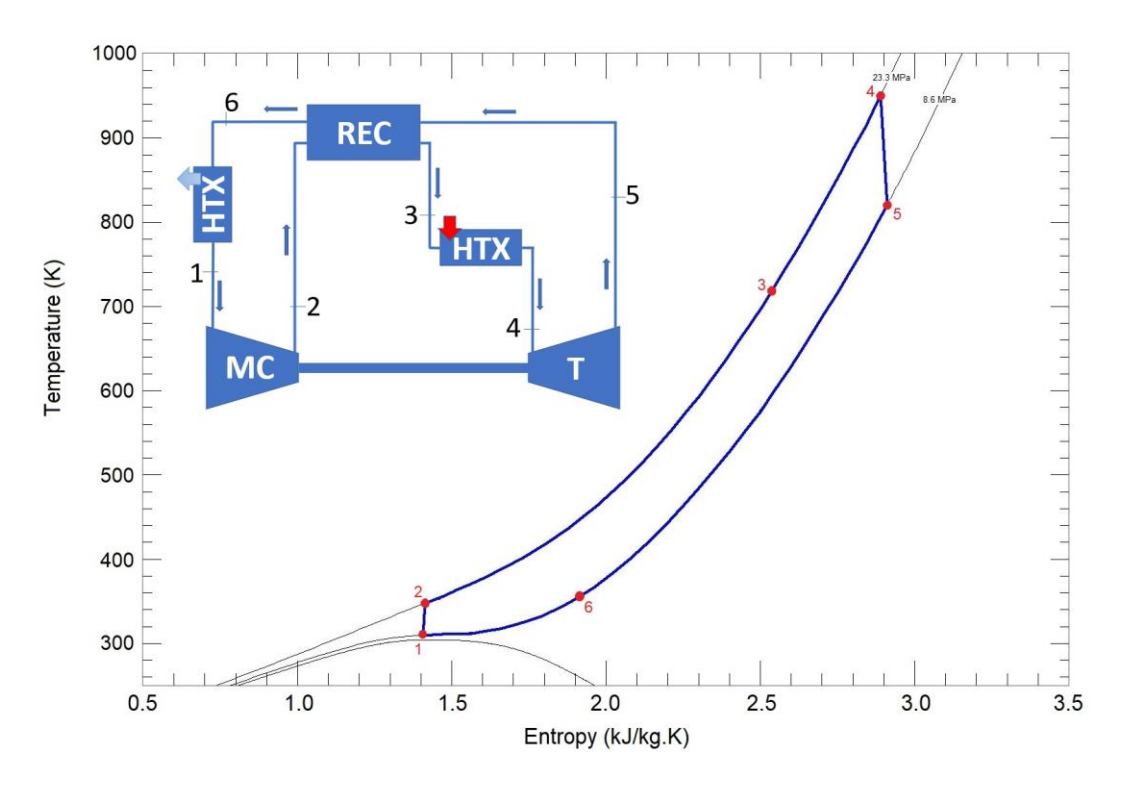


Figure 16: Simple recuperated s-CO<sub>2</sub> Brayton cycle.

#### 4.2.2. Recompression Cycle

The recompression Brayton cycle consists of two compressors, a turbine, two recuperators, and two heat exchangers, as shown in Figure 17. The pre-cooled highly dense carbon dioxide

enters the main compressor at the temperature and pressure of 310 K and 8.6 MPa respectively and exits at the temperature and pressure of 348.2 K and 23.3 MPa. Then, the compressed working fluid enters the LT recuperator, to absorb the remaining energy of CO<sub>2</sub> coming out of the HT recuperator, resulting in the increase of temperature at the constant pressure condition. On the other hand, the compressed carbon dioxide coming from the recompressor merges the stream of LT recuperator. The joint paths flow into the HT recuperator to absorb the remaining energy of CO<sub>2</sub> departed from the turbine increasing the temperature of the CO<sub>2</sub> up to 789.8 K. Subsequently, more heat is added to the working fluid in a heat exchanger, heater, and the temperature of fluid reaches a maximum in the cycle at 950 K before entering the turbine. Supercritical CO<sub>2</sub> expands in the turbine and leaves it at the temperature and pressure of 820.0 K and 8.6 MPa. Then, the energy of the leaving fluid medium from the turbine exit is transferred to the low-temperature line in the HT and LT recuperators. Afterward, the s-CO<sub>2</sub> flow splits between the main compressor and the recompressor with a share of 61.1% and 38.9% respectively. The fractions of mass flow rate between the main compressor and the recompressor were opted such that the cycle efficiency became maximum. Finally, more heat is rejected from the returning s-CO<sub>2</sub> in a heat exchanger before entering the main compressor and the cycle continues. The main parameters of the cycle performance are shown in Table 5.

It is noted that to obtain the optimized proportion of mass flow between the main compressor and the recompressor, the Approach Temperature, the temperature difference of the LT recuperator at the cold end (AT=  $T_8$ - $T_2$ ), and the efficiency of the recompressor were considered to develop a practical configuration. The former is important to ensure the pinch point does not occur in the recuperator, as previously shown in Figure 10.

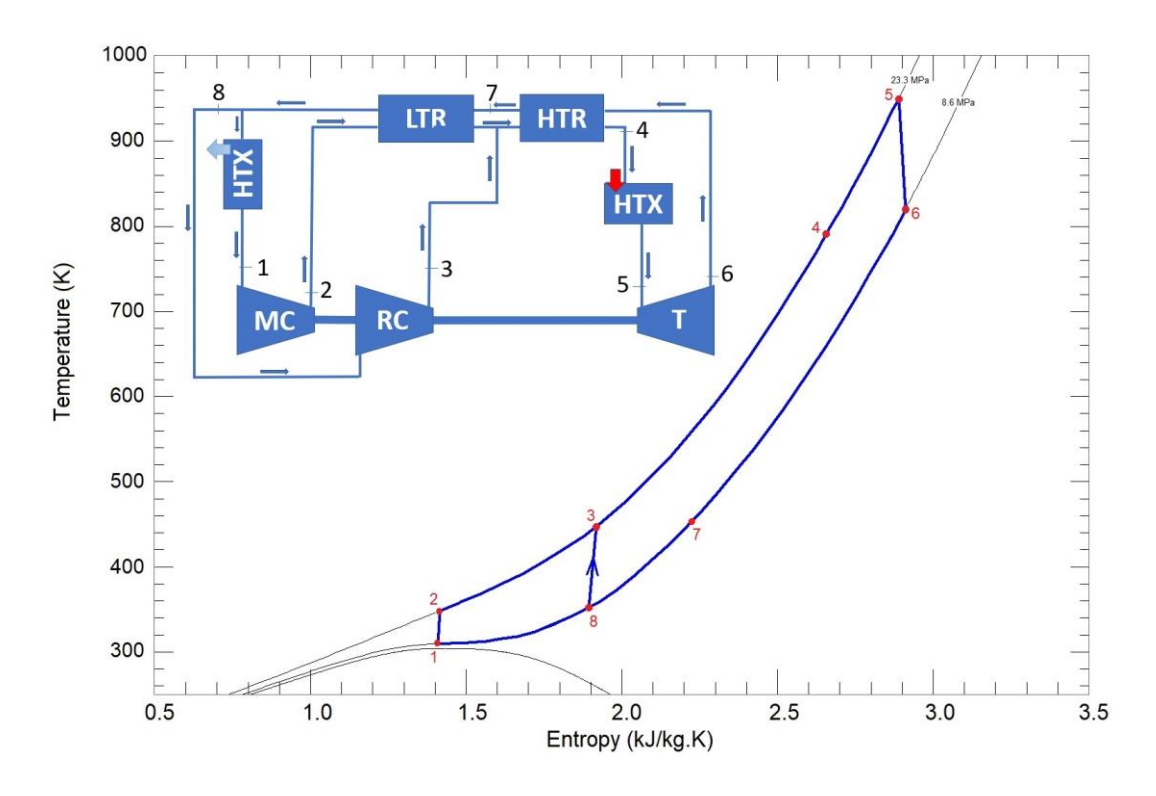


Figure 17: Recompression s-CO<sub>2</sub> Brayton cycle.

Additionally, to avoid excess assumptions in the cycle analysis, the recompressor isentropic efficiency is calculated based on the design values. Hence, it is crucial to opt for a proper mass flow split to result in a feasible compressor efficiency of close to 85%. As shown in Figure 18, for the mass flow percentage less than 58% for the main compressor, the efficiency of RC passes over 96% which is not possible. On the other hand, when the proportion of mass flow exceeds 67% for the MC, the approach temperature becomes negative implying the existence of a pinch point in the recuperator. Being said that, 61.1% was selected to obtain 85% efficiency for the recompressor which is more practical for an s-CO<sub>2</sub> compressor. The opted point is shown in black color in Figure 18.

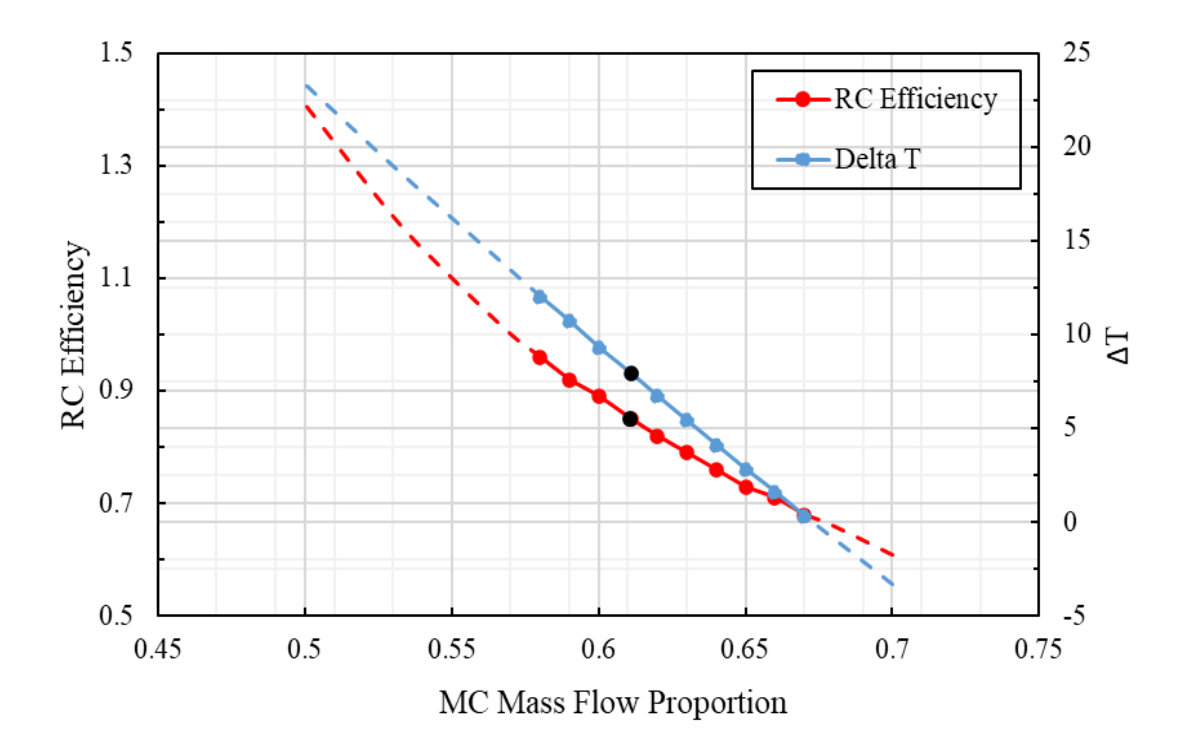


Figure 18: Acceptable range of selecting proper mass flow proportions for the main compressor and the recompressor in the recompression cycle.

### 4.2.3. Dual Turbine Cycle

The third designed s-CO<sub>2</sub> Brayton cycle is a dual turbine loop that involves two compressors, two turbines, a recuperator, and four heat exchangers, as presented in Figure 19. The cycle begins with the condensed s-CO<sub>2</sub> entering the compressor at the pressure and temperature of 8.6 MPa and 310 K accordingly and leaving it at the pressure and temperature of 14.1 MPa and 328.4 K. After rejecting some of the heat in a heat exchanger it passes through the recompressor and reaches the maximum pressure in the cycle, 23.3 MPa. The high-pressure s-CO<sub>2</sub> is then preheated in the recuperator and absorbs more heat in the heat exchanger to increase the temperature of the working medium to the highest temperature of the cycle, 950 K. The supercritical CO<sub>2</sub> expands in the first turbine losing the energy of the fluid to some extent. The second heat exchanger allows more energy to be added to the system to raise the temperature of s-CO<sub>2</sub> once again to the temperature of 950 K before entering the second turbine. The s-CO<sub>2</sub> expands further and flows into the

recuperator to transfer the remaining energy of the turbine exit to the exit of the recompressor for obtaining higher efficiency. Lastly, a heat exchanger cools down s-CO<sub>2</sub> further before entering the main compressor.

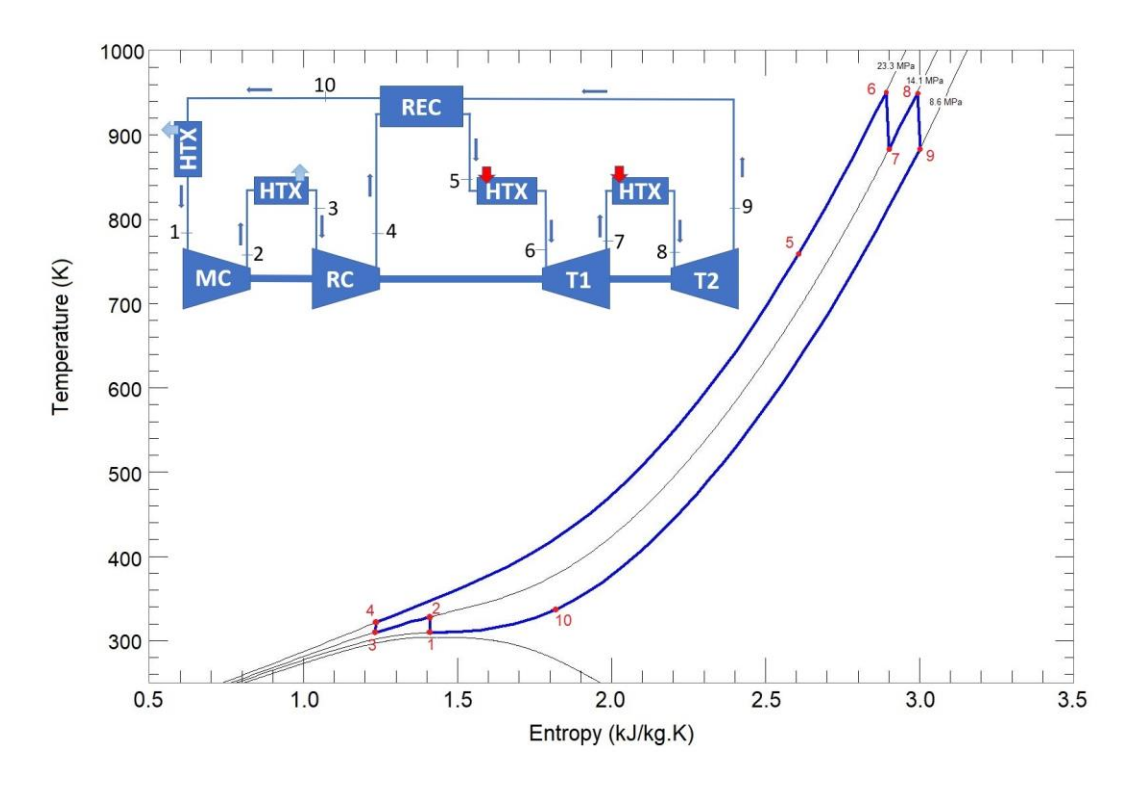


Figure 19: Dual turbine s-CO<sub>2</sub> Brayton cycle.

## 4.3. Cycle Analysis

To analyze the performance of each s-CO<sub>2</sub> Brayton cycle, several parameters such as thermal efficiency, back-work ratio  $(\dot{W}_c/\dot{W}_t)$ , and specific work will be compared. The results of the cycle reconfigurations for simple, simple recuperated, recompression, and dual turbine cycles were presented in Table 5. As shown in this table, the thermal efficiency of the simple cycle is the lowest, 14.9%. The reason for the low efficiency of the conventional s-CO<sub>2</sub> cycle is that the remaining energy of the fluid at the turbine exhaust should be rejected before entering the compressor. Given that the compressor pressure ratio (PR), the highest temperature, and the peak pressure of the cycles are the same, the cycle efficiencies of simple recuperated, and dual turbine

are 43.2%, 41.6%, respectively. Further, the recompression cycle is the most efficient cycle among the s-CO<sub>2</sub> Brayton cycles investigated, as previous studies [8] reported. The calculated efficiency for the recompression cycle in the current work also confirms that it has the highest value of thermal efficiency, 54.2%, compared to other cycle layouts. While the calculated cycle efficiency for the recompression cycle is slightly higher than the thermal efficiency evaluated in literature [93], reported to be 43%-49% for the turbine inlet temperature of 903 K-953 K accordingly, it could be due to not considering the losses in the cycle analysis.

As to the back-work ratio, the compressors of the recompression cycle expend higher turbine-produced power with a ratio of 28.3% compared to the simple, simple recuperated cycles with a similar value of 17.8%. The rationale for the same back-work ratios obtained for the latter schemes is that the number of compressors and turbines is the same for these cycles, and the assumed maximum and minimum pressure, and temperatures are also alike resulting in the same value. Besides, the back-work ratio for the dual turbine cycle was the lowest, 15.3%, which is an advantage of this cycle, however, the capital cost is high for this cycle because two compressors and two turbines are required for the dual turbine cycle.

It is evident from the data in Table 4 and Table 5 that although the net output power is the same for each cycle, 11.11 MW, the mass flow rates for each cycle are different, interpreted as different specific work. In other words, the lowest mass flow rate required for a cycle indicates that the specific work is the highest resulting in higher compactness and lower capital cost. In the current cycle layouts, the specific work for simple, simple recuperated, recompression, and dual turbine cycles are 125.13, 125.13, 109.16, and 134.59 kJ/kg, respectively. Hence, although the recompression cycle is the most efficient layout, the operating cost of this cycle is higher. That is more investment is required to set up a recompression s-CO<sub>2</sub> Brayton cycle because it has the

lowest specific work compared to the simple, and simple recuperated cycles. The lowest value for the specific work of the recompression cycle was also reported in the modeling performed by Wang et al. [36].

Table 5: Performance parameters of various layouts of s-CO<sub>2</sub> Brayton cycles.

	Simple	Simple Recuperated	Recompression	Dual Turbine
<b>ṁ</b> [kg/s]	88.79	88.79	101.78	82.55
$\eta_{RC,s}$ []			0.85	0.85
$\dot{\mathbf{Q}}_{\mathbf{H}}\left[\mathbf{MW}\right]$	74.61	25.74	20.50	26.74
$\dot{\mathbf{Q}}_{\mathbf{L}}\left[\mathbf{MW}\right]$	63.50	14.63	9.39	15.63
η <sub>T</sub> []	0.149	0.432	0.542	0.416
$\dot{W}_c/\dot{W}_t$ []	0.178	0.178	0.283	0.153
$\dot{\mathbf{W}}_{n}/\dot{m}[\mathrm{kJ/kg}]$	125.13	125.13	109.16	134.59

Further, while the dual turbine cycle is the least efficient cycle, 41.6%, the specific work is the highest, 134.59 kJ/kg, and the back-work ratio is the lowest, 15.3%. Hence, this conclusion can be drawn that the simple recuperated is a compromise between the benefits of the dual turbine cycle and the recompression cycle when cycle efficiency,  $\dot{W}_c/\dot{W}_t$  ratio, and specific work are considered in opting for a suitable 10 MWe s-CO<sub>2</sub> Brayton power cycle.

## CHAPTER 5: 1-D COMPRESSOR DESIGN METHODOLOGTY

The design procedure involves a centrifugal impeller and a pinched diffuser sizing within which Acceleration to Condensation Margin (AMC) was considered in the methodology to avoid condensation in the inlet and outlet design. The 1-D meanline centrifugal compressor design methodology was developed in MATLAB within which the CoolProp NIST database, based on the SW EOS, was integrated to obtain the real-time values of the fluid properties. The design code is based on the continuity equation and Euler equation, which relates the conservation of energy to the conservation of momentum, as follows:

$$\dot{m} = \rho A C_m \tag{14}$$

$$\Delta h_{0,Euler} = h_{02} - h_{01} = U_2 C_{u2} - U_1 C_{u1} \tag{15}$$

In the design process, the enthalpy loss correlations were considered to calculate the total pressure ratio and the actual efficiency of the compressor as:

$$\eta_{act} = \frac{\Delta h_{0,Euler} - \sum \Delta h_{0,int}}{\Delta h_{0,act}} = \frac{\Delta h_{0,Euler} - \sum \Delta h_{0,int}}{\Delta h_{0,Euler} + \sum \Delta h_{0,ext}}$$
(16)

where  $\Sigma \Delta h_{int}$ ,  $\Sigma \Delta h_{ext}$ , and  $\Delta h_{act}$  are the internal losses, external (parasitic) losses, and the actual input enthalpy change, including the parasitic works, respectively. The schematic of the 1-D design procedure for a centrifugal compressor with a pinched diffuser is presented in Figure 20.

In the developed design procedure, inlet total temperature  $(T_{01})$ , inlet total pressure  $(P_{01})$ , pressure ratio (PR), and the mass flow rate  $(\dot{m})$  are the inputs obtained from cycle analysis, and the values for the rotational speed (N), blade tip speed  $(U_2)$ , blade thickness  $(t_b)$ , inlet blade angle  $(\beta_1)$ , the ratio of outlet to inlet radii of the impeller  $(r_2/r_1)$ , and the number of the blades (Z) are assumed. Also, by assuming an initial value for the isentropic efficiency of the compressor, the design process starts, and the actual compressor efficiency is calculated and compared with the

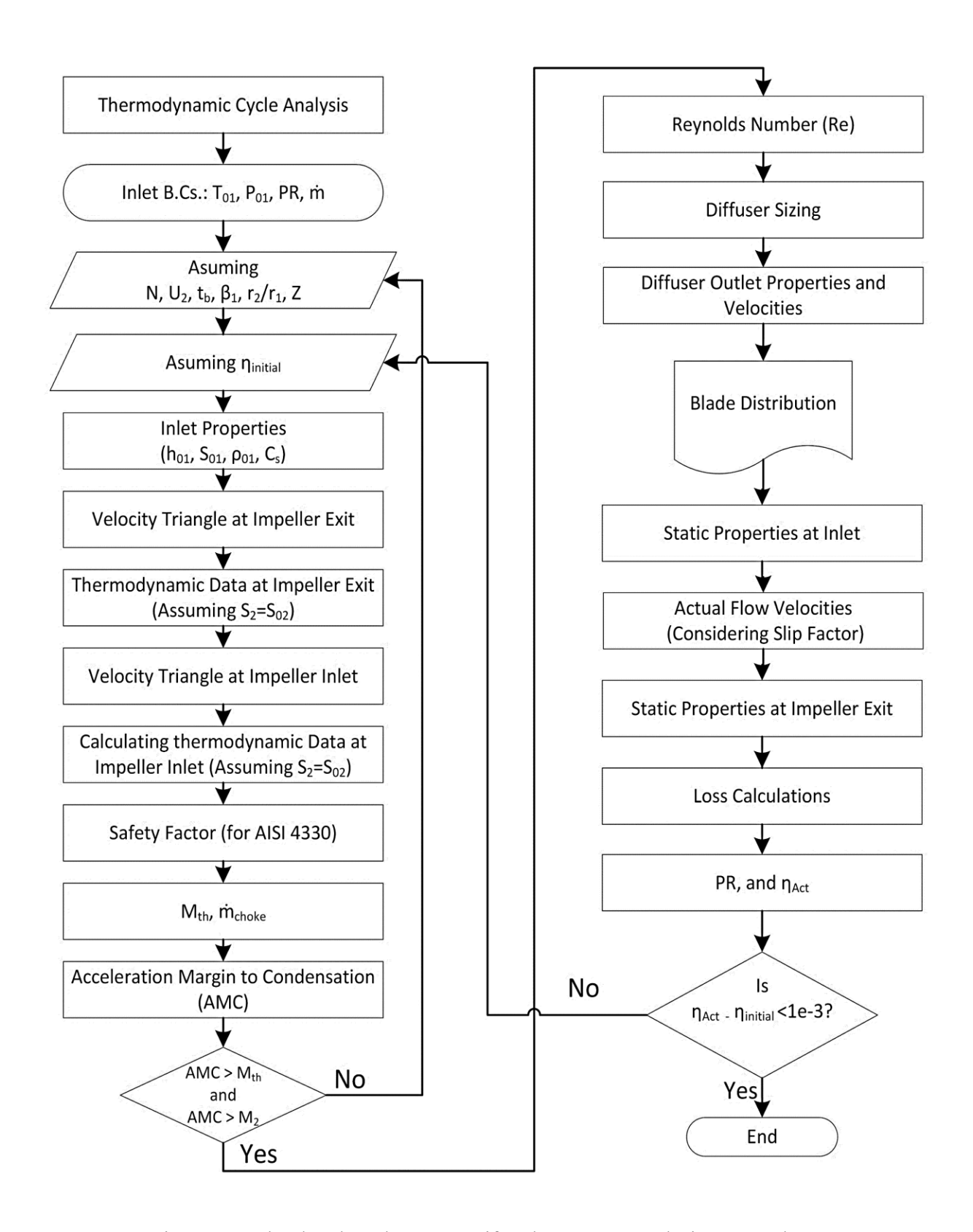


Figure 20: The developed 1-D centrifugal compressor design procedure.

initial value. If the difference between these two values is greater than an error criterion (e.g., 1e-3) then another value for efficiency is chosen until this condition is met. This section is divided into four parts including inlet condition criterion, impeller design, diffuser design, and loss models which will be discussed in detail.

#### **5.1. Inlet Condition Criterion**

Selecting an appropriate boundary condition is the first step to obtaining a stable compressor design. While it is desired to opt for inlet conditions close to the critical point to capture the benefits of supercritical CO<sub>2</sub> in full, it is essential that it does not affect the compressor's stability. That is, a careful evaluation is required when choosing the inlet boundary conditions of an s-CO<sub>2</sub> compressor. The design point candidate must fulfill two primary criteria: first, the inlet pressure and temperature of the compressor must be close to the critical point as feasible, and second, the inlet conditions must not fall into the Widom region. The Widom or pseudocritical region is a wedge-shaped area in the phase (P-T) diagram pointing to the critical point. The principal reason that this region must be avoided is the abnormal and unpredictable behavior of CO<sub>2</sub> in this region. The Widom region is a transitional zone between the liquid-like and vapor-like sections of the supercritical area. In this region, each property behaves anomalously along its Widom line, as shown in Figure 21. Therefore, it is vital to select a temperature and pressure that is not located in the Widom region; otherwise, the flow in the compressor will become unstable and also leads to convergence problems in the CFD simulations.

Imre et al. [63] estimated the Widom lines for density  $(\rho)$ , speed of sound  $(C_s)$ , isobaric heat capacity  $(C_p)$ , isochoric heat capacity  $(C_v)$ , isothermal compressibility  $(\kappa_T)$ , and thermal expansivity  $(\alpha_p)$  by using cubic polynomial equations to fit different Widom lines obtained from the Span-Wagner equation of state as follows:

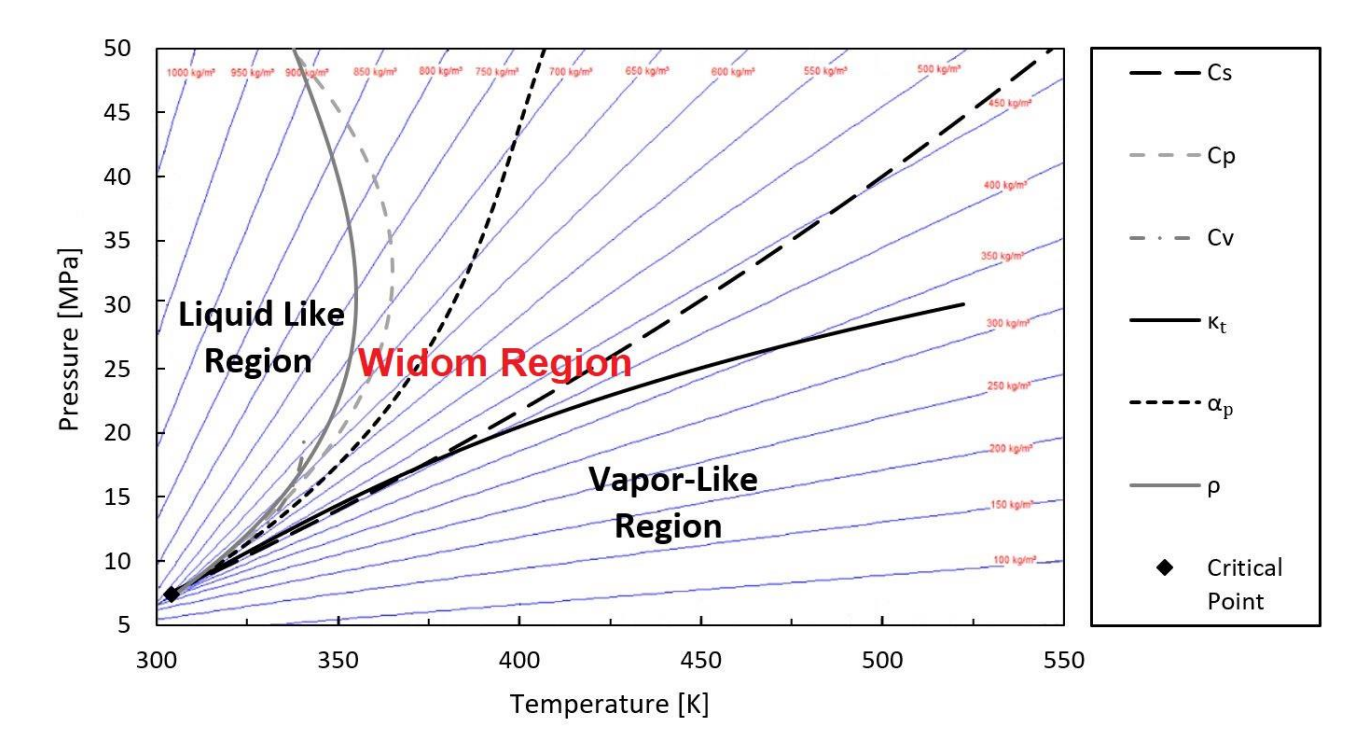


Figure 21: CO<sub>2</sub> density contours along with different areas of supercritical region in the phase diagram: Liquid-like, Vapor-Like, and Widom. The Widom lines of CO<sub>2</sub> were obtained from a polynomial fit of the SW equation of state (the polynomial relations adapted from Imre [63]).

$$T = A + BP + CP^2 + DP^3 \tag{17}$$

in which A, B, C, and D are the coefficients of the polynomials and compiled in Table 6.

Table 6: Coefficients of cubic polynomials for Widom lines approximation [63].

Quantity	A (K)	B (K/MPa)	C (K/MPa^2)	D (K/MPa^3)	Range (MPa)
$C_s$	244.5	8.37	-0.062	0.00031	7.5-50
$C_p$	265.3	6.18	-0.097	0.00004	7.5-50
$C_{v}$	233.2	12.73	-0.464	0.00482	7.5-20
ρ	260.6	7.22	-0.169	0.00111	7.5-50
$lpha_p$	255.7	7.65	-0.149	0.00113	7.5-50
$\kappa_T$	249.2	8.57	-0.221	0.00796	7.5-30

In the developed 1-D code for the s-CO<sub>2</sub> compressor, a subroutine was written to check the location of the inlet boundary conditions in the supercritical region. Also, to ensure avoiding these anomalies at the exit of the compressor, the outlet temperature and pressure of the designed compressor is checked to warrant both inlet and outlet conditions lying in either liquid-like or vapor-like region. It is worth mentioning that the compressor operating in the liquid-like region is more stable than working in the vapor-like region, as discussed in [20, 24].

A secondary factor that is also critical to consider in the inlet boundary condition selection is the Acceleration to Condensation Margin (AMC). AMC is the Mach number at the inlet of the compressor corresponding to the static pressure  $(P_{lim})$  and static temperature  $(T_{lim})$  where condensation takes place (saturation line), as shown in Figure 22. This characteristic is important

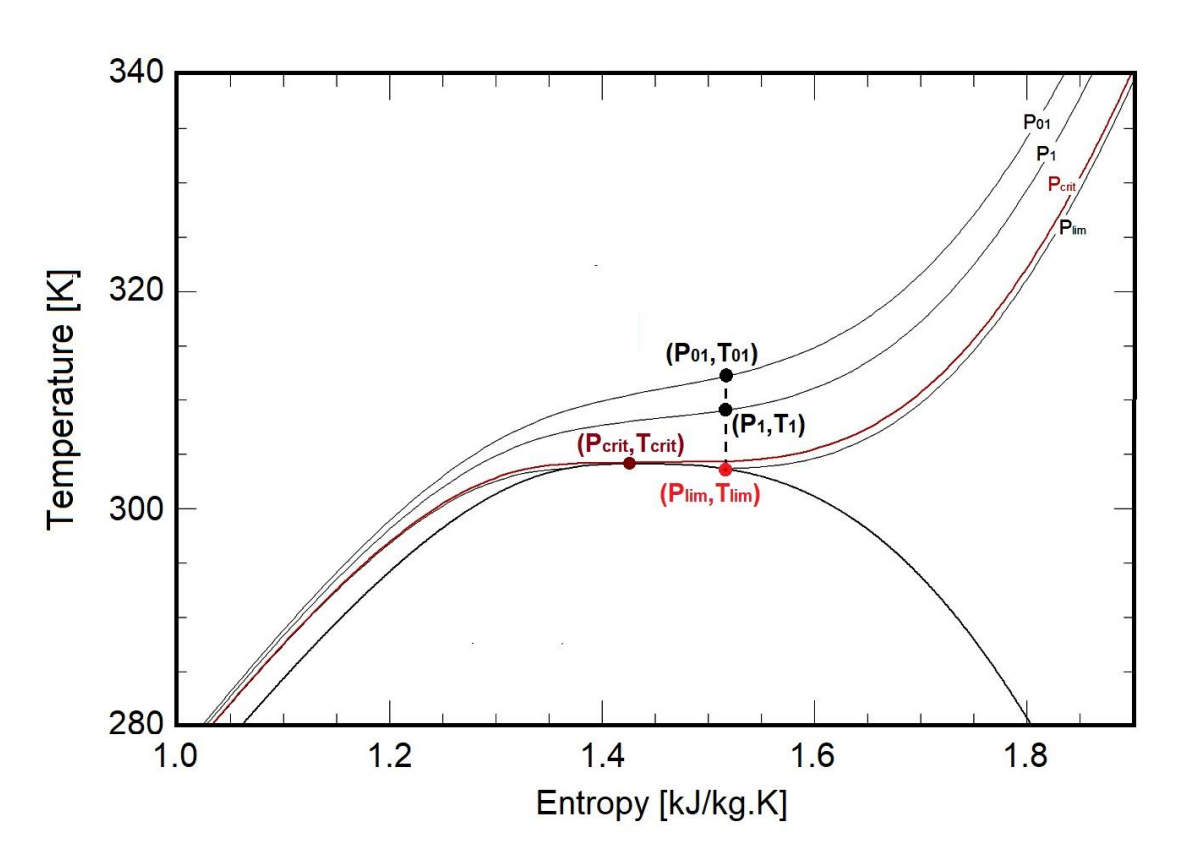


Figure 22: AMC calculation based on the static pressure and temperature at the inlet of the compressor.

because it indicates whether condensation will occur at the inlet of the designed compressor or not and is given by:

$$AMC = \frac{V_{limit}}{C_{s,limit}} \tag{18}$$

where,

$$V_{limit} = \sqrt{2(h_{01} - h_{limit})} \tag{19}$$

## 5.2. Impeller Design

In the current research, the impeller sizing correlations defined by Aungier [94] are utilized. The correlations are based on the aerodynamic performance and geometry of a few successful industrial compressor designs and are valid for the stage flow coefficients 0.009-0.125. Thus, the same method was opted for the supercritical CO<sub>2</sub> impeller sizing as follows:

$$\beta_s = \beta_{1s} + (\beta_2 - \beta_{1s})(3\zeta^2 - 2\zeta^3) \tag{20}$$

$$\beta_h = \beta_{1h} + A\zeta + B\zeta^2 + C\zeta^3 \tag{21}$$

$$A = -4(\beta_2 - 2\bar{\beta_h} + \beta_{1h}) \tag{22}$$

$$B = 11\beta_2 - 16\bar{\beta}_h + 5\beta_{1h} \tag{23}$$

$$C = -6\beta_2 + 8\bar{\beta}_h - 2\beta_{1h} \tag{24}$$

$$\bar{\beta}_h = 90K + \frac{(1 - K)(\beta_2 + \beta_{1h})}{2} \tag{25}$$

where  $\zeta$ ,  $\beta_s$ , and  $\beta_h$  are the normalized meridional distance, the blade distribution (blade angle) from the leading edge to the trailing edge at the shroud and hub, respectively. It is worth noting the K value is a factor that adjusts the hub blade angle allowing to have control over the rake angles. The rake angle is the angle between the hub and the shroud in the circumferential direction and the suggested value by Aungier [94] is less than 1 to have rake angles less than 15°.

## 5.3. Diffuser Design

In the current design procedure, a pinched vaneless diffuser was utilized based on the Aungier [94] sizing. The advantage of using a pinched diffuser is mainly to avoid backflow and separation within the diffuser. Also, the pinch makes the flow field more uniform before and after the diffuser. The sizing and the design of the pinched section of the diffuser are as follows:

$$r_4 = r_2 \left( 1.55 + \varphi_{Stage} \right) \tag{26}$$

$$\alpha_4 = 30 + \left(\frac{\varphi_{Stage}}{0.06}\right)^2 \tag{27}$$

$$b_4 = k_b \ b_2 \tag{28}$$

where  $r_2$ ,  $r_4$ , and  $k_b$  are the tip radius, diffuser exit radius, and the ratio of diffuser exit width to impeller exit width, respectively. The radius and the width where the pinching ends are defined as:

$$r_3 = k_p r_2 \tag{29}$$

$$b_3 = b_2 \tag{30}$$

in which  $k_p$  is the ratio of the pinched radius to the tip radius. The width of the impeller exit to the pinch ending point at the shroud of the diffuser is obtained as:

$$b_{2-3,s} = D + E * r + F * r^2 \tag{31}$$

where,

$$F = \frac{b_2 - b_3 + b'_3(r_3 - r_2)}{(r_3 - r_2)^2}$$
 (32)

$$E = b'_3 - 2 r_3 * F (33)$$

$$D = b_2 + E * r_2 - F * r_2^2 (34)$$

$$b'_{3} = \frac{b_{4} - b_{3}}{r_{4} - r_{3}} \tag{35}$$

### 5.4. Loss Models

In the current design code, internal and external (parasitic) losses were considered to obtain a more realistic s-CO<sub>2</sub> compressor design. The procedure is based on the ratio of total pressure leaving the compressor to the total pressure entering the compressor and the actual efficiency within which the internal and external losses are included, as shown in Eq. (16). The internal losses include incidence, blade loading, skin friction, tip-clearance, mixing, choke and, vaneless diffuser losses. On the other hand, leakage, recirculation, and disc friction losses are categorized as parasitic losses. That is,

$$\sum \Delta h_{0,int} = \Delta h_{0,Inc} + \Delta h_{0,BL} + \Delta h_{0,SF} + \Delta h_{0,Cl} + \Delta h_{0,Mix} + \Delta h_{0,Ch} + \Delta h_{0,VLD}$$
(36)

$$\sum \Delta h_{0,ext} = \Delta h_{0,LK} + \Delta h_{0,DF} + \Delta h_{0,RC}$$
 (37)

The loss models are explained in detail below.

Incidence Loss. The incidence loss is associated with the mismatch of the relative flow velocity with the blade angle at the entry of the impeller passage. This misalignment resulted in a flow separation when the relative velocity  $W_1$  tried to comply with the blade's relative velocity  $W_{1b}$ , as shown in Figure 23. The change in the kinetic energy resulted from the relative velocity will be lost as the flow adjusted to the blade direction according to NASA theory [95, 96]. Therefore, the enthalpy loss because of the incidence is estimated as follows:

$$\Delta h_{0,inc} = f_I \left( \frac{W_{\theta 1}^2}{2} \right) = f_I \left( \frac{(U_1 - C_{u1} - \cot \beta_{1b} C_{m1})^2}{2} \right)$$
 (38)

where  $f_I$  is the correction factor ranges between 0.5 and 0.7, as suggested by Conrad et al. [97], and  $W_{\theta 1}$  is the loss of the tangential component of the relative velocity at the inlet of the impeller.

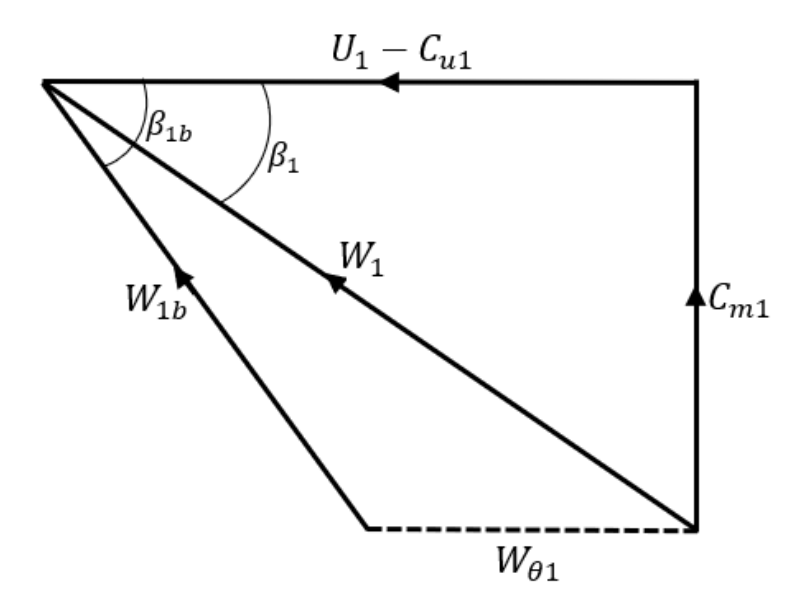


Figure 23: Incidence loss at the inlet of the impeller [98].

**Blade Loading Loss.** The blade loading loss is arisen due to the boundary layer growth along the blade leading to the momentum loss and separation in the impeller. The energy loss estimation was given by Coppage et al. [99]:

$$\Delta h_{0.BL} = 0.05 \ D_f^2 U_2^2 \tag{39}$$

where  $D_f$  is the diffusion factor and defined as:

$$D_f = 1 - \frac{W_2}{W_{1s}} + \frac{0.75\Delta h_0}{U_2^2} \left( \frac{\frac{W_2}{W_{1s}}}{\frac{Z}{\pi} \left( 1 - \frac{d_{1s}}{d_2} \right) + 2\frac{d_{1s}}{d_2}} \right)$$
(40)

**Skin Friction Loss.** This loss is generated due to the shear flow on the bounded walls of the impeller's blade. The model proposed by Jansen [100] considers the flow passage of the impeller as a fully-developed circular pipe flow with the average hydraulic diameter and the average length of the flow passage in the impeller estimated as:

$$\Delta h_{0,SF} = 2C_f L_B \frac{\overline{W}^2}{d_{Hvd}} \tag{41}$$

in which  $d_{Hyd}$ , and  $L_B$  are the hydraulic diameter, and flow length respectively as:

$$d_{Hyd} = d_2 \left( \frac{\sin \beta_2}{\frac{Z}{\pi} + \frac{d_2}{b_2} \cos \beta_2} + \frac{0.5 \left( \frac{r_{1s} + r_{1h}}{r_2} \right) \left( \frac{\sin \beta_{1s} + \sin \beta_{1h}}{2} \right)}{\frac{Z}{\pi} + \frac{r_{1s} + r_{1h}}{r_{1s} - r_{1h}} \left( \frac{\sin \beta_{1s} + \sin \beta_{1h}}{2} \right)} \right)$$
(42)

$$L_{B} = \frac{\pi}{8} \left( d_{2} - \frac{d_{1h} + d_{1s}}{2} - b_{2} + 2L_{ax} \right) \left( \frac{4}{\sin \beta_{1s} + \sin \beta_{1h} + 2\sin \beta_{2}} \right)$$
(43)

where  $L_{ax}$  is the axial length of the impeller expressed by Birdi [101] as:

$$\frac{L_{ax}}{d_2} = \sqrt{\left[0.28(M_{w1s} + 0.8)\left(1 - \frac{d_{1m}}{d_2}\right)\frac{d_{1s} - d_{1h}}{d_2}\right]}$$
(44)

and  $C_f$  is friction coefficient defined by Mehrewan P. Boyce [102] as:

$$\begin{cases} C_f = \frac{2.67}{Re^{0.5}} , & if Re < 300,000 \\ C_f = \frac{0.0622}{Re^{0.2}} , & if Re \ge 300,000 \end{cases}$$
 (45)

The Reynolds number (Re) and its average values  $(\bar{\rho}, \bar{\mu}, \text{ and } \bar{W})$  are obtained from:

$$Re = \frac{\bar{\rho}\bar{W}d_{Hyd}}{\bar{\mu}} \tag{46}$$

$$\bar{\rho} = \frac{\rho_1 + \rho_2}{2}$$

$$\bar{\mu} = \frac{\mu_1 + \mu_2}{2}$$

$$\bar{W} = \frac{W_{1s} + W_{1h} + 2W_2}{4}$$
(47)

Clearance Loss. In an unshrouded impeller, there is a gap between the impeller tip and the shroud resulting in the leakage flow from the pressure side to the suction side of the blade, as shown in Figure 24. This escape of working fluid from the impeller tip is known as the clearance loss and results in efficiency and pressure losses. The enthalpy loss because of the clearance is given by Jansen [100] as:

$$\Delta h_{0,Cl} = 0.6 \left(\frac{t_{cl}}{b_2}\right) C_{u2} \sqrt{\frac{4\pi}{Z} \left[\frac{r_{1s}^2 - r_{1h}^2}{b_2 (r_2 - r_{1s}) (1 - \rho_2/\rho_1)}\right] C_{m1} C_{u2}}$$
(48)

in which  $t_{cl}$  is the clearance between the impeller tip and the shroud.

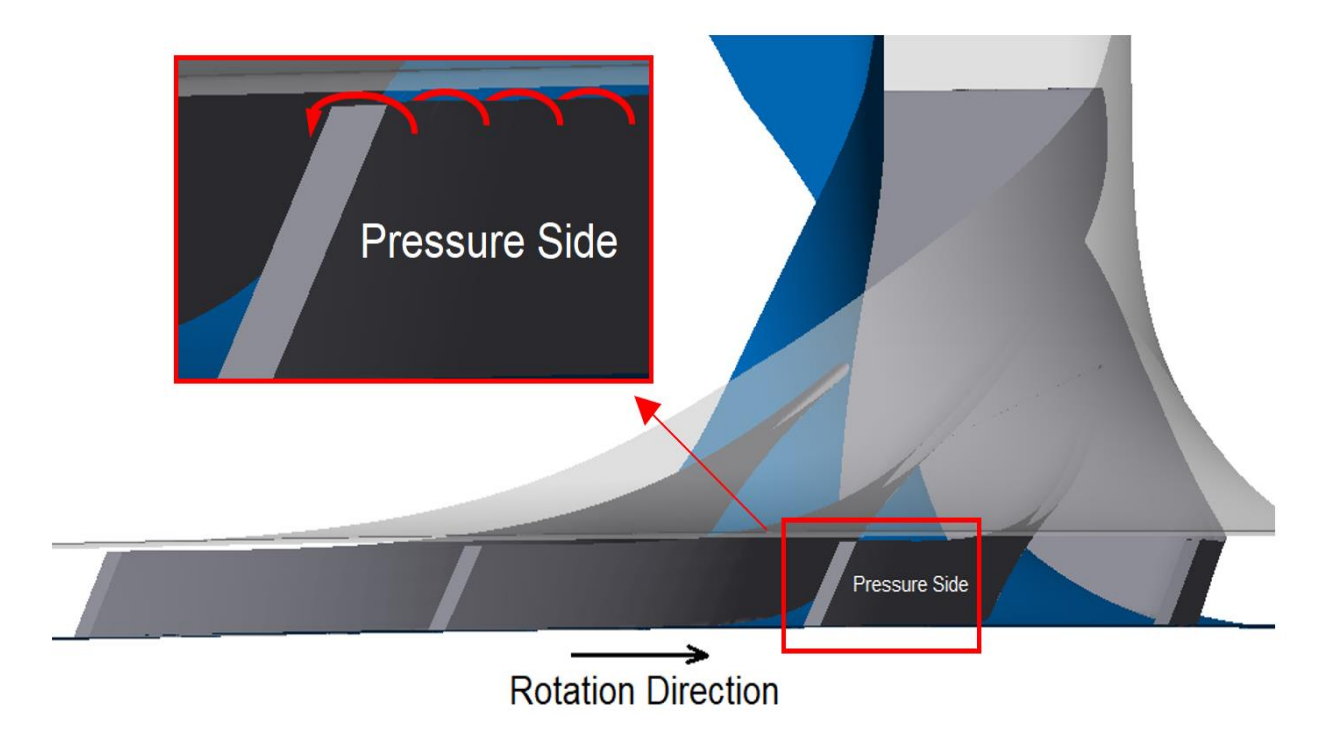


Figure 24: Energy loss due to the tip clearance of the impeller.

**Mixing Loss.** Previous studies [103, 104] showed that, on one hand, a secondary flow is generated at the tip of the blade at the trailing edge similar to a jet wake due to the blade thickness and the non-uniform flows at the pressure and the suction sides of the blade. On the other hand, the boundary layer is developed on the shroud and then mixed with the secondary flow in the nozzle. This turbulent mixing gives rise to the mixing loss. The mixing loss proposed by Johnston and Dean [103] is as follows:

$$\Delta h_{0,Mix} = \frac{1}{1 + \cot^2 \alpha_2} \left( \frac{1 - \varepsilon_{wake} - b^*}{1 - \varepsilon_{wake}} \right)^2 \frac{C^2}{2}$$
 (49)

where  $b^*$  is the ratio of diffuser height at the inlet to the impeller height at the outlet  $(b^* = b_{i,d}/b_2)$  ranging from 0.8 to 0.95 according to [103]. Also,  $\varepsilon_{wake}$  is the fraction of the blade-to-blade distance occupied by the wake calculated based on the model proposed by Stuart et al. [105] and given by:

$$\varepsilon_{wake} = \frac{0.78 \frac{\chi}{\varphi_2}}{0.88 + \frac{\chi}{\varphi_2}} \tag{50}$$

in which  $\chi$  is the wake mass fraction and  $\varphi_2$  is flow coefficient at the exit of the impeller defined as follows:

$$\chi = 3.05 \,\varphi_2^2 - 2.65 \,\varphi_2 + 0.778 \tag{51}$$

$$\varphi_2 = \frac{\dot{m}}{\rho_2 U_2 A_2 (1 - B_2)} \tag{52}$$

**Choke Loss.** If the flow in the impeller, especially at the throat, becomes sonic, then the choke loss model must be considered in the performance estimation. The mathematical model of choke loss proposed by Aungier [94] is:

$$\Delta h_{0,Ch} = \begin{cases} 0, & X \le 0\\ 0.5 * (0.05X + X^7) \frac{W_1^2}{2}, & X > 0 \end{cases}$$
 (53)

where X is a modified criterion suggested by Klausner and Gampe [106]:

$$X = \frac{\dot{m}}{\dot{m}_{Ch}} - \left(11 - 10\frac{\dot{m}}{\dot{m}_{Ch}}\right)^4 \tag{54}$$

$$\dot{m}_{Ch} = \rho_{Ch} C_{s,Ch} A_{Th} (1 - B_1) \tag{55}$$

and  $\dot{m}_{Ch}$  is the choke mass flow rate,  $B_1$  is the inlet blockage, and  $C_{s,Ch}$  is the speed of sound at choke defined as:

$$C_{s,Ch} = \sqrt{Z_{Ch}\gamma_{CO2}R_{CO2}T_{Ch}} \tag{56}$$

To calculate the throat area  $(A_{Th})$  of the main blades, the finite difference method was used by dividing the area into **n** sections as follows:

$$\Delta d = \frac{r_{1s} - r_{1h}}{n}$$

$$\Delta \beta = \frac{\beta_{1s} - \beta_{1h}}{n}$$
(57)

$$d_{1}(i) = d_{1h} + (i-1) * \Delta d$$
  

$$\beta_{1h}(i) = \beta_{1h} + (i-1) * \Delta \beta$$
(58)

$$\Delta A_{Th}(i) = \left(\frac{\pi * d_1(i)}{Z/2} - t\right) * \sin\beta_{1b}(i) * \Delta d$$
 (59)

Thus, the total throat area of the impeller will be obtained as follows:

$$A_{Th} = \left(\frac{Z}{2}\right) * \sum_{i=1}^{n} \Delta A_{Th}(i) \tag{60}$$

The geometric calculation of the throat area is shown in Figure 25.

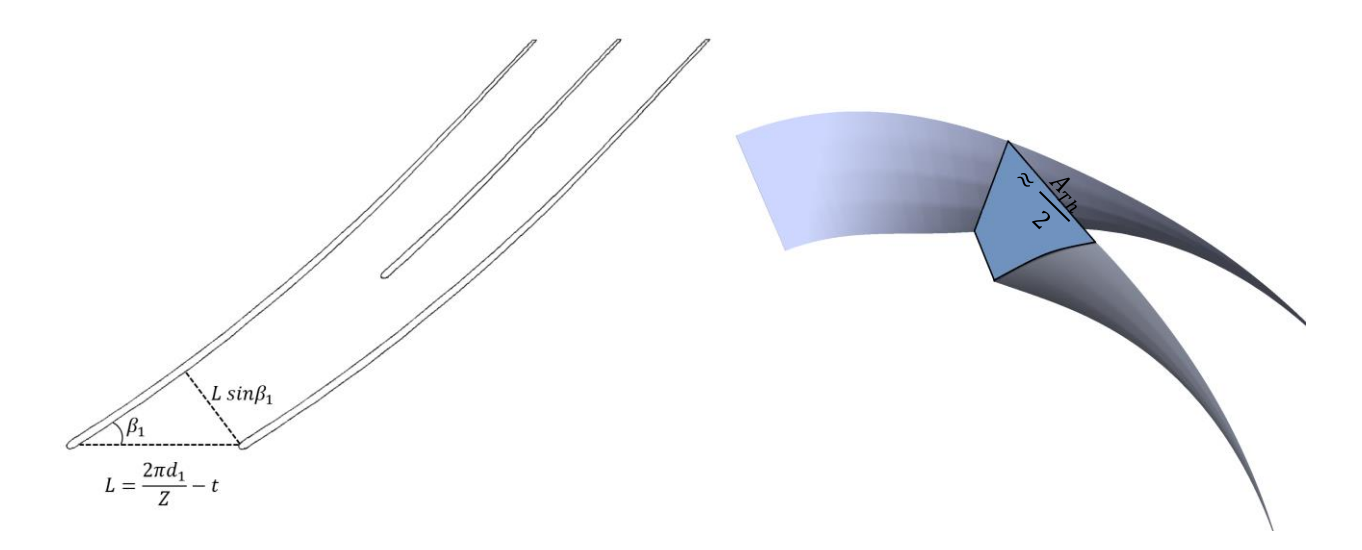


Figure 25: Throat area calculation.

Vaneless Diffuser Loss. In the vaneless diffuser, part of the energy will be lost because of friction. Therefore, it is crucial to estimate the vaneless diffuser in the design. The model to estimate the total pressure loss is based on the experiments performed by Zhu and Sjolander [107]:

$$p_{04} = p_{02} - \Omega \left( \frac{\rho_2 c_2^2}{2} \right) \tag{61}$$

In this relation,  $\Omega$  is the total pressure loss coefficient which can be looked up from the graphs Zhu and Sjolander [107] reported in their work. This graph is based on the absolute flow angle at the inlet of the diffuser, and the type of diffuser: expanding width, constant width, or pinched (contracting width) diffuser. Being found the pressure at the exit of the diffuser  $(p_{04})$ , one can estimate the enthalpy loss from the following equation, assuming  $S_{04} = S_{02}$ :

$$\Delta h_{0,VLD} = h_{02} - h_{04}(p_{04}, S_{02}) \tag{62}$$

**Leakage Losses.** In centrifugal compressors, there exists a gap between the impeller and the stationary component with lower pressure compared to the exit of the impeller. Thus, some fluid flow through the gap and exits through the seal known as the leakage loss, as shown in Figure 26. The Aungier [94] method for the leakage loss is expressed as:

$$\Delta h_{0,LK} = \frac{\dot{m}_{LK} U_{LK}}{2\dot{m} U_2} \tag{63}$$

where  $\dot{m}_{LK}$  is the leakage mass flow rate in the tip clearance as well as the gap between the impeller and the back wall and defined as follows:

$$\dot{m}_{LK} = \rho_2 U_{LK} \left[ 2\pi r_2 (t_{Gap} + t_{cl}) \right] \tag{64}$$

It is noted that the area considered to calculate the leakage mass flow rate in Eq. (64) was modified by the author. Also,  $U_{LK}$  is the velocity in the leakage pathways given by:

$$U_{LK} = 0.816 \sqrt{\frac{2\Delta P_{LK}}{\rho_2}} \tag{65}$$

in which  $\Delta P_{LK}$  is the pressure difference between the exit of the impeller and the gap space obtained from:

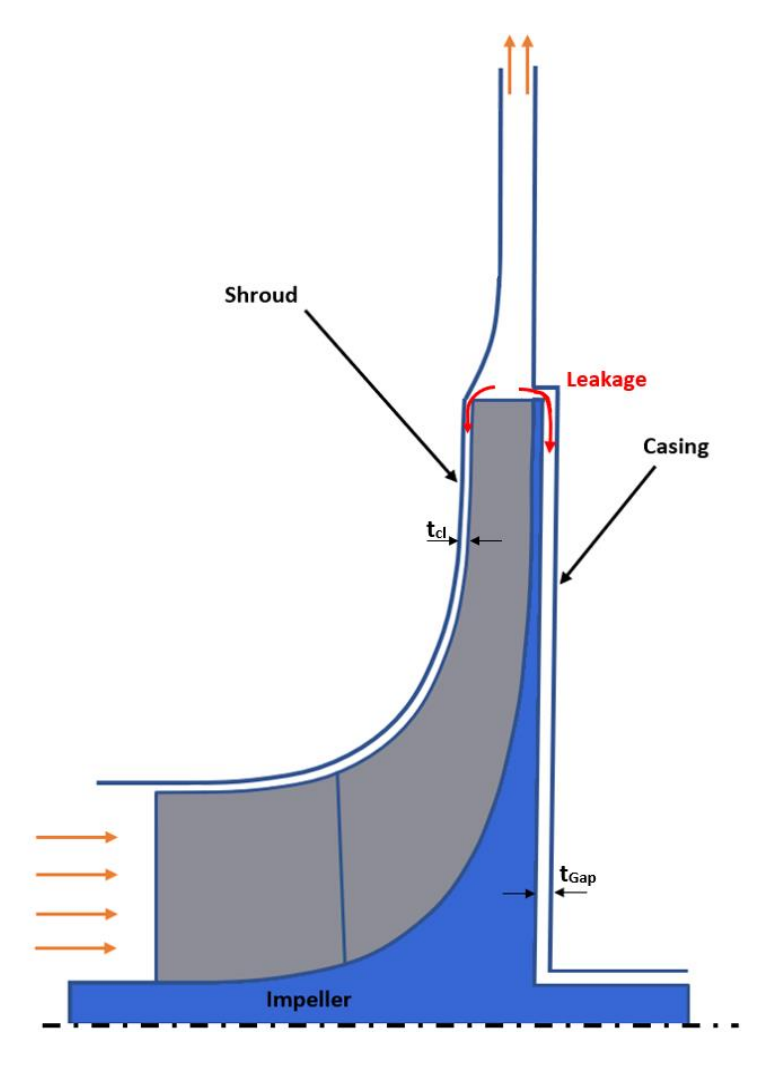


Figure 26: Leakage flow in centrifugal compressors.

$$\Delta P_{LK} = \frac{\dot{m}(r_2 C_{u2} - r_1 C_{u1})}{z \bar{r} \bar{b} L_B}$$
 (66)

where  $\bar{r}$ , and  $\bar{b}$  are the average radius and blade width defined as:

$$\bar{r} = \frac{r_1 + r_2}{2}$$

$$\bar{b} = \frac{b_1 + b_2}{2}$$
(67)

It is worth noting that these equations assume the inlet condition of the compressor is the same as the flow condition leaving the compressor through the air gap and then through the seal. **Disc Friction Loss.** This loss is generated because of the friction of the leakage flow with the back wall of the rotating impeller. The disk friction loss of Daily and Nece [108] is calculated as:

$$\Delta h_{0,DF} = f_{DF} \frac{\bar{\rho} r_2^2 U_2^3}{4\dot{m}} \tag{68}$$

where  $\bar{\rho}$  is the average density and  $f_{DF}$  is the friction factor of the disc, which is as follows:

$$f_{DF} = \begin{cases} \frac{2.67}{Re_{DF}^{0.5}} & Re_{DF} < 3 \times 10^5\\ \frac{0.0622}{Re_{DF}^{0.2}} & Re_{DF} \ge 3 \times 10^5 \end{cases}$$
(69)

in which,

$$Re_{DF} = \frac{U_2 r_2}{v_2} \tag{70}$$

**Recirculation Loss.** The third parasitic loss is recirculation loss which occurs at the exit of the impeller. In other words, the high-pressure flow returns back to the impeller due to the low-pressure condition at the inlet of the impeller resulting in the loss of pressure as well as efficiency. The loss model proposed by Oh et al. [109] is expressed as:

$$\Delta h_{0,RC} = 8 \times 10^{-5} \sinh\left(3.5 * (\frac{\pi}{2} - \alpha_2)^3\right) * D_f^2 U_2^2$$
 (71)

# 5.5. Characteristic Design Parameters

Characteristic design parameters are parameters that should be met in a compressor design to establish whether the design is satisfactory; hence, the characteristic design parameters are calculated to complement the outlet design. The methodology to determine the design characteristics is as follows:

$$\psi = \frac{\Delta h_{0s}}{U_2^2} \tag{72}$$

$$\mu = \frac{\Delta h_0}{U_2^2} \tag{73}$$

$$\varphi_{Stage} = \frac{Q_1}{\pi r_2^2 U_2} \tag{74}$$

$$\begin{cases} N_{s,Dixon} = \left(\frac{\varphi^{0.5}}{\psi^{0.75}}\right)_{Dixon} = \frac{U_{avg} \cdot C_m^{0.5}}{\Delta h_0^{0.75}} \\ N_{s,Balje} = \frac{\omega \cdot \sqrt{Q_1}}{(g \cdot H_{ad})^{0.75}} \text{, where } H_{ad} = \frac{\Delta P}{\rho_{avg} \cdot g} \end{cases}$$
(75)

$$\begin{cases} D_{s,Dixon} = \left(\frac{\psi^{0.25}}{\varphi^{0.5}}\right)_{Dixon} = \frac{\Delta h_0^{0.25}}{C_{m,avg}^{0.5}} \\ D_{s,Balje} = \frac{d_2(g \cdot H_{ad})^{0.25}}{Q_1} \end{cases}$$
(76)

where  $\psi$ ,  $\mu$ ,  $\varphi_{Stage}$ ,  $N_s$ , and  $D_s$  are head coefficient, input work coefficient, stage flow coefficient, specific speed, and specific diameter, respectively. It is worth noting that AMC is also an important parameter to ensure that an s-CO<sub>2</sub> compressor does not fall below the saturation line at the inlet and outlet of the compressor. Regarding the specific speed and diameter, the criteria were estimated through Dixon estimation [110], and Balje formulation [111].

### **CHAPTER 6: VALIDATION**

To evaluate the fidelity of the 1-D developed design code, it is essential to be validated against experimental data. For this reason, this chapter is dedicated to validating the code with available measured data for an air compressor and an s-CO<sub>2</sub> compressor from the literature. Also, the performance plot will be compared with the CFD simulation by using ANSYS CFX; however, the CFD governing equations, CFD setup details, and results will be described and discussed in the next chapter. It is noted that the contents of air compressor validation first appeared as [112].

### 6.1. Air Compressor

The 1-D code was validated with the experimental results performed by Eckardt [113-115] for the air compressors. His extensive results have become a benchmark for centrifugal compressors. He designed three impellers known as Impeller-O, Impeller-A, and Impeller-B and carried out extensive measurements. His results including complete performance characteristics and the flow field measurements are used extensively for validation, accuracy test, and design robustness in 1-D codes, 2-D codes and CFD. In the present study, a secondary code was developed for the air compressor within which ideal gas law was utilized to validate the procedure of the compressor design by using the 1-D code with the Eckardt Impeller-A to produce his results and geometry with reasonable accuracy. The design conditions of Eckardt impeller-A as well as the important parameters obtained from the 1-D code are reported in Table 7.

Table 7: The design conditions for Eckardt Impeller-A. Design parameters were obtained from the 1-D code.

m (kg/s)	N (RPM)	T <sub>01</sub> (K)	P <sub>01</sub> (kPa)	PR ()	<i>U</i> <sub>2</sub> (m/s)	<b>Z</b> ()	$\eta_{t-t}$ ()
4.54	14000	288.1	101.3	1.91	295	18	0.8825

Further, a 3-D impeller was generated in ANSYS BladeGen by utilizing the data obtained from the developed 1-D code and then CFD simulation was conducted in ANSYS CFX. In Figure 27, the performance plots, efficiency, and pressure ratio, obtained from the 1-D code and CFD simulation were compared against the measured data from Impeller-A. It is evident from this figure that the trend fairly matches the experimental data and the overprediction of 1-D code and CFD simulation at the higher mass flow rates could be due to not considering the volute in the design.

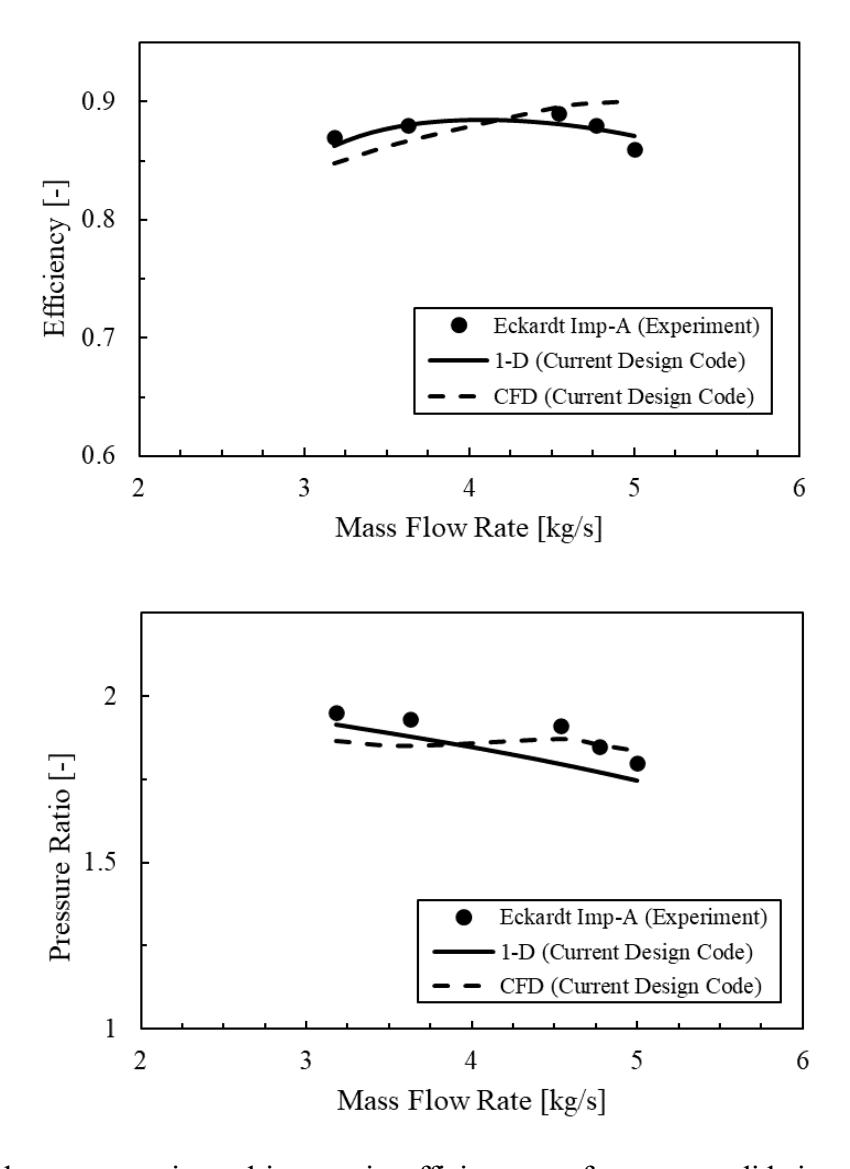


Figure 27: Total pressure ratio and isentropic efficiency performance validation for the Eckardt Impeller-A by using the current 1-D code developed and CFD simulation for various mass flow rates at 14,000 RPM with the blade tip speed of 295 m/s.

## 6.2. S-CO<sub>2</sub> Compressor

While the 1-D code was validated with an air compressor, it is necessary to investigate the validity of the developed meanline code with an s-CO<sub>2</sub> compressor data since supercritical CO<sub>2</sub> behaves differently. Based on this ground, the available experimental data reported by Sandia [44] for a small-scale s-CO<sub>2</sub> compressor employed in a Brayton cycle test facility was utilized for comparison purposes. In this regard, the 1-D code was modified to replicate Sandia's compressor, and then the design parameters obtained from the on-design code were imported to an off-design code to reproduce the performance map. Further, the 3-D impeller was generated in BladeGen and meshed in Turbogrid and CFD simulation was performed to include and compare the results with the measured data. The s-CO<sub>2</sub> compressor used by Sandia includes 6 main blades and 6 splitters with a 17-wedged-shaped vane diffuser. The compressor they utilized is an open impeller with the operating conditions and design parameters listed in Table 8, and Table 9, respectively.

Table 8: Operating conditions (design point) of Sandia's s-CO<sub>2</sub> compressor.

N	T <sub>01</sub>	P <sub>01</sub>	ṁ	PR
[RPM]	[K]	[MPa]	[kg/s]	[-]
75,000	305.3	7.69	3.53	1.819

Table 9: Design parameters of Sandia's s-CO<sub>2</sub> compressor.

<b>Z</b> [-]	S [-]	<b>Z</b> <sub>v</sub> [-]				$eta_{1s,tang} \ [ ext{deg}]$		
12	6	17	18.68	2.54	9.37	40	40	0.762

where  $Z_v$  is the number of vanes. Regarding the sizing of the vaned diffuser, the Aungier [94] method was utilized in the 1-D code due to the lack of information as follows:

$$r_3 = r_2 \left( 1 + \frac{\alpha_{2,deg}}{360} + \frac{M_2^2}{15} \right) \tag{77}$$

$$r_4 = r_2 \left( 1.5 + \varphi_{Stage} \right) \tag{78}$$

$$\alpha_{4,deg} = 30 + \left(\frac{\varphi_{Stage}}{0.06}\right)^2 \tag{79}$$

where the subscripts 2, 3, and 4 denote the impeller outlet, vane inlet, and vane outlet accordingly. It is worth noting that the following values were assumed:

$$b_4 = b_3 = b_2$$

$$\beta_3 = \beta_2/2$$

$$\theta_C = 7^{\circ}$$
(80)

where  $2\theta_C$  is known as the divergence angle of the vane. Based on the abovementioned design criteria, the geometry of the impeller generated in ANSYS BladeGen is shown in Figure 28. Besides, the geometry Meshed in ANSYS Turbogrid and the total number of nodes being generated in the domain is approximately 921,000. The generated mesh is shown in Figure 29.

The CFD simulation was performed in ANSYS CFX by considering a two-phase model to capture the condensation. The boundary condition at the inlet was set to total pressure and temperature and the mass flow rate was utilized at the outlet. In addition, the  $k-\omega$  shear stress turbulence model was employed along with viscous heating. As an additional note, the impeller was treated as a rotating domain at the interface with a mixing-plane model. Furthermore, since the inlet condition is fairly close to the critical point, a slight change in temperature and pressure in the compressor channel would result in condensation. Phase change in CFX can be considered by using a homogeneous binary mixture multiphase model. The results of CFD simulation at different mass flow rates were compared to the 1-D code and the experimental data from Sandia, as shown in Figure 30. It must be noted that the compressor geometry is based on the design

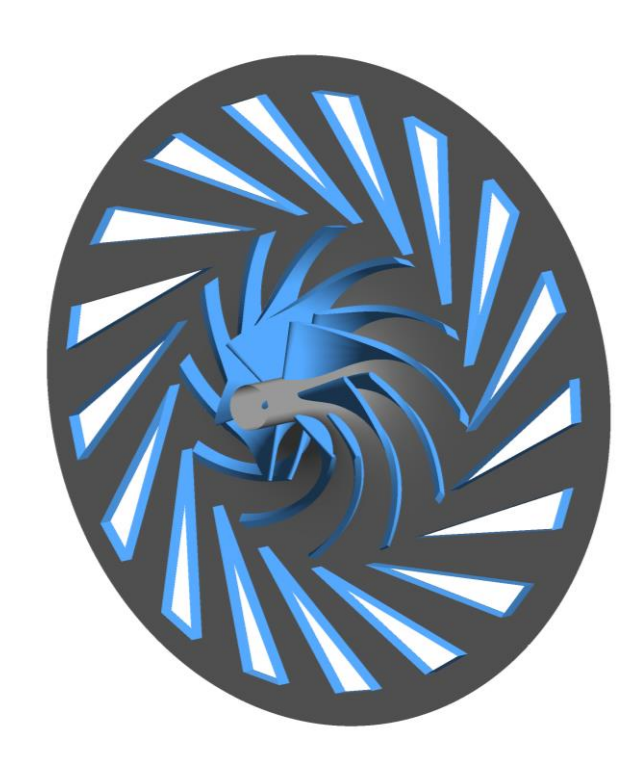


Figure 28: The geometry of Sandia's compressor generated in BladeGen by obtaining the design parameters from the current 1-D design code.

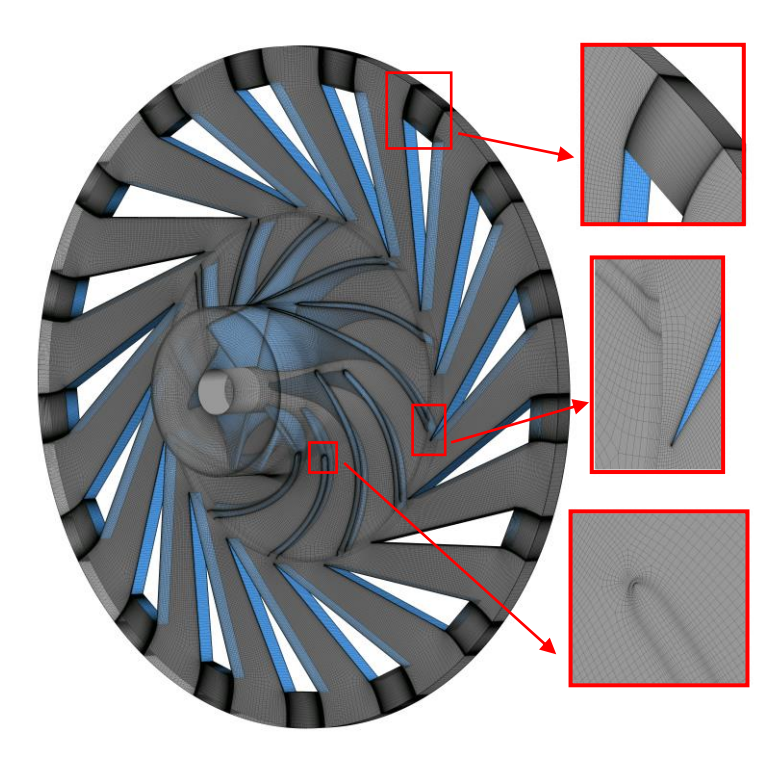


Figure 29: The mesh domain of Sandia's compressor generated in Turbogrid by obtaining the design parameters from the current 1-D design code.

speedline (75,000 RPM) while the validation is made with the available data for 50,000 RPM.

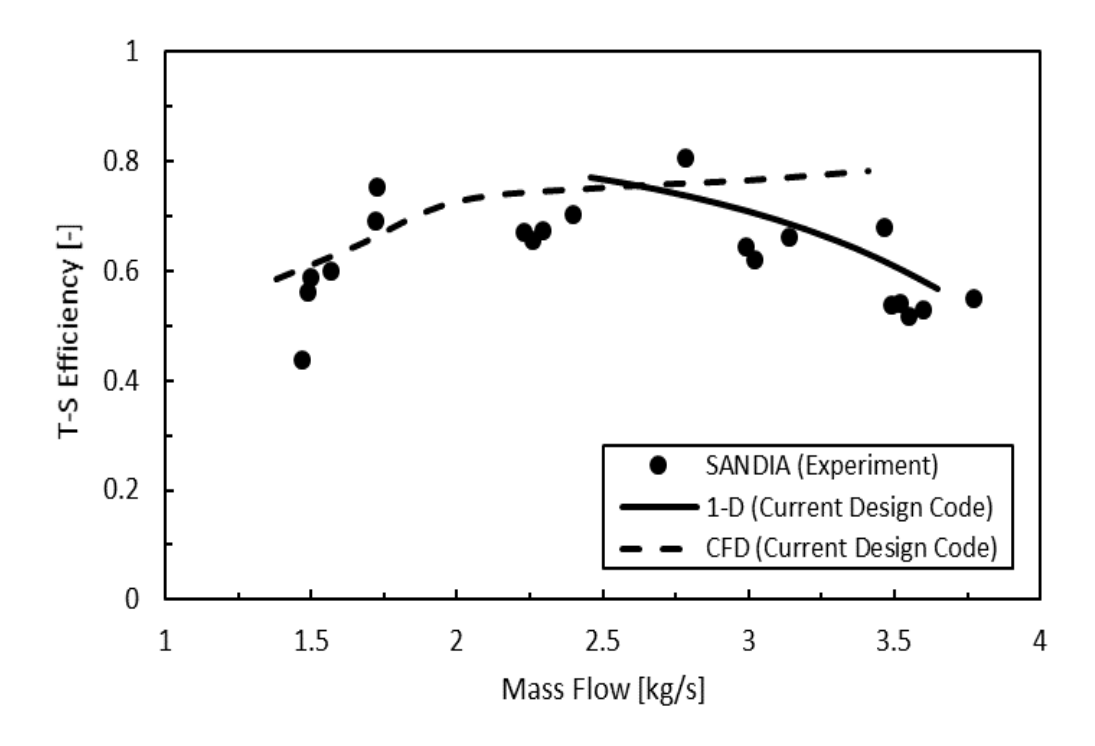


Figure 30: Performance maps of the current 1-D code, and the CFD simulation in comparison with the measured data from Sandia for the 50,000 RPM speedline.

It is evident from Figure 30 that while CFD results match the experimental data, the 1-D code couldn't calculate the total-to-static efficiency of the Sandia's compressor for the mass flow rates below 2.5 kg/s. The author believes that it could be due to the following reasons: (1) some assumptions were made in the design procedure, i.e., the Aungier method was used for vaned diffuser sizing to replicate the Sandia compressor in the 1-D code and details of vane's shape was not reported, (2) the measured data were reported in terms of corrected mass flow based on a reference value not known to the author, resulting in a misalignment between the measured data, the CFD results, and the 1-D code, and (3) the total temperature and pressure at the inlet of the Sandia's compressor are 305.3 K and 7.69 MPa which are equivalent to the static temperature and pressure of 293.7 K and 5.8 MPa which are well below the saturation line. Since the code is unable to evaluate the speed of sound in the two-phase region based on the available NIST database, the

code cannot run the performance map below this value. Based on the results of the CFD simulation for the Sandia compressor at the design speedline (75,000 RPM), this conclusion can also be drawn that the condensation at the inlet of the compressor is due to the inlet conditions resulting in an unstable CFD simulation, as shown in Figure 31. Therefore, this conclusion is made that a slight difference in the validation was expected based on the abovementioned valid grounds.

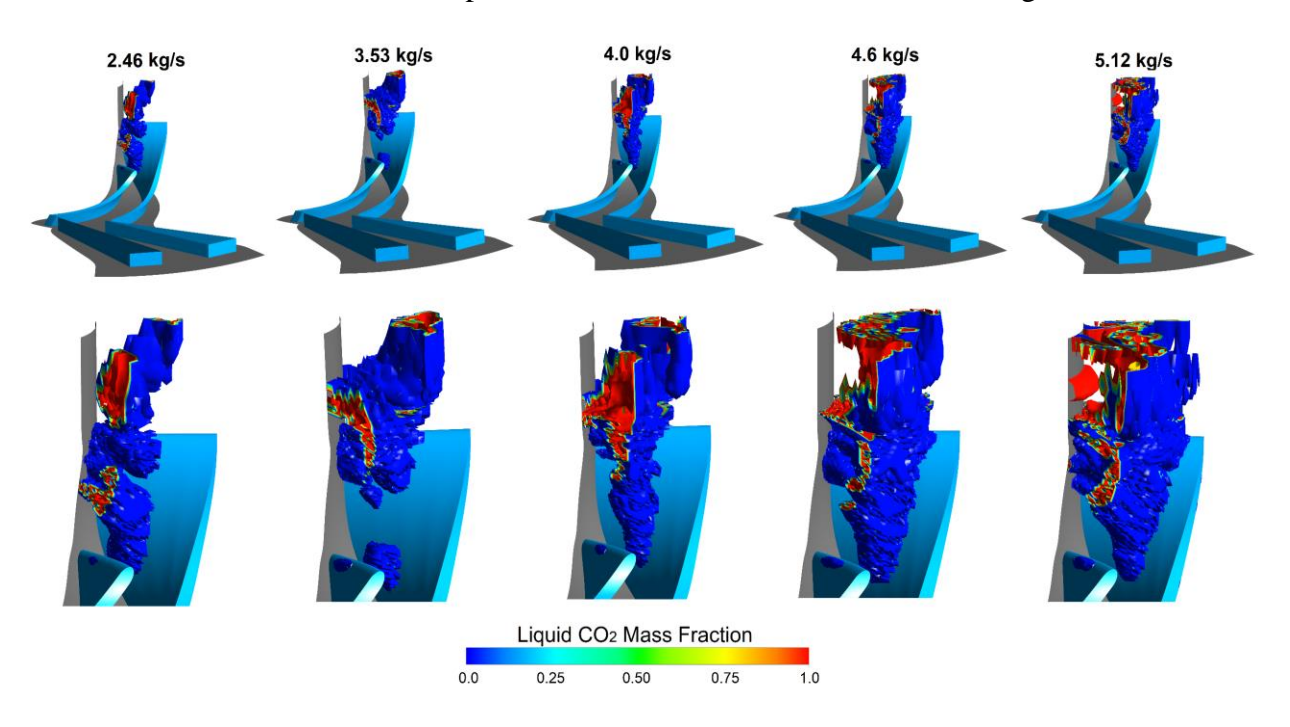


Figure 31: Liquid mass fraction contours inside the impeller at different mass flow rates.

# CHAPTER 7: CFD ANALYSIS AND COMPRESSOR PERFORMANCE

In this chapter, the governing equation of the flow field inside the compressor will be elaborated. Further, the CFD setup used in the s-CO<sub>2</sub> compressor simulation will be described in detail. Besides, the result of mesh dependency on the mass flow rate, pressure ratio, and efficiency will be presented. Finally, a new stable s-CO<sub>2</sub> compressor is proposed and the CFD results will be discussed. This chapter is adapted and expanded from [116].

# 7.1. Governing Equations

The instantaneous governing equation for the flow field in a stationary frame are the continuity, momentum, and total enthalpy energy equations, given by [117]:

$$\frac{\partial \rho}{\partial t} + \nabla \cdot (\rho \mathbf{C}) = 0 \tag{81}$$

$$\frac{\partial(\rho C)}{\partial t} + \nabla \cdot (\rho CC) = -\nabla p + \nabla \cdot \overline{\overline{\tau}} + S_M$$
 (82)

$$\frac{\partial(\rho h_{tot})}{\partial t} - \frac{\partial p}{\partial t} + \nabla \cdot (\rho C h_{tot}) = \nabla \cdot (\lambda \nabla T) + \nabla \cdot (C \cdot \bar{\tau}) + C \cdot S_M + S_E$$
(83)

where  $S_M$ , and  $S_E$  are the momentum and energy source terms, respectively. Also, C,  $\overline{\overline{\tau}}$ , and  $h_{tot}$  are absolute velocity, shear stress tensor and total enthalpy defined as follows:

$$\overline{\overline{\tau}} = \mu \left( \nabla \mathbf{C} + (\nabla \mathbf{C})^T - \frac{2}{3} \delta \nabla \cdot \mathbf{C} \right)$$
(84)

$$h_{tot} = h + \frac{C^2}{2} \tag{85}$$

It is worth mentioning that the  $\nabla \cdot (\mathbf{C} \cdot \overline{\tau})$  is viscous work term which is due to the viscous stresses. While in most cases it is negligible, it should be included in a simulation involving multiple frames of reference (rotating frame).

It is noted that w is substituted for C in Eq. (82) since the impeller is rotating. Further, three source terms must be considered for the momentum equation in a rotating frame as follows:

$$S_{M,Coriolis} = -2 \rho (\boldsymbol{\omega} \times \boldsymbol{w})$$
 (86)

$$S_{M,Centrifugal} = -\rho \ \omega \times (\omega \times r)$$
 (87)

$$\mathbf{S}_{M,Ang.\ Acc.} = -\rho \ \frac{\partial \boldsymbol{\omega}}{\partial t} \times \boldsymbol{r} \tag{88}$$

where  $\boldsymbol{\omega}$  and  $\boldsymbol{w}$  are angular velocity and relative velocity, respectively. Also,  $\boldsymbol{S}_{M,Coriolis}$ ,  $\boldsymbol{S}_{M,Coriolis}$ , and  $\boldsymbol{S}_{M,Ang.\ Acc.}$  are Coriolis force, centrifugal force, and angular acceleration source terms, accordingly. Moreover, the total enthalpy term  $(h_{tot})$  will be substituted by rothalpy (I) in the total enthalpy equation (Eq. (83)) when the frame is rotating, as follows:

$$I = h + \frac{w^2}{2} - \frac{\omega^2 R^2}{2} \tag{89}$$

Besides, an additional source term is required to consider the angular acceleration in the energy equation, given by:

$$S_{E,Ang.Acc.} = -\rho \left[ \mathbf{w} \cdot \left( \frac{\partial \mathbf{\omega}}{\partial t} \times \mathbf{r} \right) + (\mathbf{\omega} \times \mathbf{r}) \cdot \left( \frac{\partial \mathbf{\omega}}{\partial t} \times \mathbf{r} \right) \right]$$
(90)

To close the system of equations with 6 unknowns  $(w_x, w_y, w_z, T, p, \rho)$ , an equation of state is required to be solved apart from the continuity, momentum, and total enthalpy equations. The importance of opting for an appropriate equation of state for supercritical CO<sub>2</sub> application was already discussed in section 3.2. The equation of state selected for the simulation in the current work is Span-Wagner EOS which is based on the Helmholtz energy. Other thermodynamic properties are derived directly from the Helmholtz energy. This model is based on the non-dimensional temperature  $(\tau)$  and density  $(\delta)$  defined as [70]:

$$\tau = \frac{T_c}{T} \tag{91}$$

$$\delta = \frac{\rho}{\rho_c} \tag{92}$$

where  $T_c$ , and  $\rho_c$  are critical temperature and density. The non-dimensional Helmholtz energy  $(\phi)$  is then described as:

$$\phi(\delta, \tau) = \frac{A(\rho, T)}{RT} = \phi^{0}(\delta, \tau) + \phi^{r}(\delta, \tau)$$
(93)

where  $\phi^0$  is the term that accounts for the ideal-gas portion of the Helmholtz energy and  $\phi^r$  is the residual term accounting for the non-ideal behavior of the Helmholtz energy, defined as follows:

$$\phi^{0}(\delta,\tau) = \ln(\delta) + a_{1}^{0} + a_{2}^{0}\tau + a_{3}^{0}\ln(\tau) + \sum_{i=4}^{8} a_{i}^{0}\ln[1 - \exp(-\tau \theta_{i}^{0})]$$
 (94)

$$\phi^{r}(\delta,\tau) = \sum_{i=1}^{7} n_{i} \, \delta^{d_{i}} \, \tau^{t_{i}} + \sum_{i=8}^{34} n_{i} \, \delta^{d_{i}} \, \tau^{t_{i}} \, e^{-\delta^{C_{i}}}$$

$$+ \sum_{i=35}^{39} n_{i} \, \delta^{d_{i}} \, \tau^{t_{i}} \, e^{-\alpha_{i}(\delta - \epsilon_{i})^{2} - \beta_{i}(\tau - \gamma_{i})^{2}} + \sum_{i=40}^{42} n_{i} \, \Delta^{b_{i}} \, \delta \, e^{-C_{i}(\delta - 1)^{2} - D_{i}(\tau - 1)^{2}}$$

$$(95)$$

with,

$$\Delta = \left\{ (1 - \tau) + A_i (\delta - 1)^{1/\beta_i} \right\}^2 \tag{96}$$

where  $n_i$ ,  $d_i$ ,  $t_i$ ,  $a_i$ ,  $b_i$ ,  $A_i$ ,  $B_i$ ,  $C_i$ ,  $D_i$ ,  $\alpha_i$ ,  $\beta_i$ ,  $\gamma_i$ ,  $\epsilon_i$ , and  $\theta_i$  are exponents and coefficients that are listed in detail in the literature [70].

In addition, since Reynolds-Averaged-Navier-Stokes (RANS) approach was chosen for the CFD simulation, a Reynolds stress term  $< u_i'u_j' >$  is added to the RANS equations in the averaging process which requires modeling. In this research,  $k - \omega$  Shear Stress Transport (SST) model was used due to the high accuracy in predicting the onset and amount of flow separation under positive (adverse) pressure gradients. This turbulence model is a form of eddy viscosity model that assumes the proportionality of the Reynolds stress to the mean velocity gradients ( $\bar{S}_{ij}$ ) and turbulent (eddy)

viscosity  $(v_t)$ , that is:

$$< u'_{i}u'_{j}> = -2\nu_{t}\bar{S}_{ij} + \frac{2}{3}k\delta_{ij}$$
 (97)

In this model, k, and  $\omega$  are turbulent kinetic energy, and turbulent frequency equations described as follows:

$$\frac{\partial(\rho k)}{\partial t} + \nabla \cdot (\rho \mathbf{C} k) = \nabla \cdot \left[ \left( \mu + \frac{\mu_t}{\sigma_\nu} \right) \nabla k \right] + P_k - \beta' \rho k \omega + P_{kb}$$
 (98)

$$\frac{\partial(\rho\omega)}{\partial t} + \nabla \cdot (\rho \mathbf{C}\omega) = \nabla \cdot \left[ \left( \mu + \frac{\mu_t}{\sigma_{\omega 1}} \right) \nabla \omega \right] 
+ P_{\omega} - \beta \rho \omega^2 + \frac{2(1 - F_1)\rho}{\sigma_{\omega 2} \omega} \nabla k \cdot \nabla \omega + P_{\omega b}$$
(99)

where  $P_{kb}$ , and  $P_{\omega b}$  are the production terms in the kinetic energy and turbulent frequency equations due to the buoyancy which are negligible in the current simulation studies. Furthermore,  $P_k$ , and  $P_{\omega}$  are the production rate of kinetic energy and turbulent frequency, respectively, where:

$$P_{\omega} = \frac{\alpha}{v_t} P_k \tag{100}$$

and the turbulent viscosity is computed from:

$$v_t = \frac{a_1 k}{\max\left(a_1 \omega_t S F_2\right)} \tag{101}$$

where  $F_1$ ,  $F_2$  are blending factors, S is the magnitude of strain rate, and  $\alpha$ ,  $\beta$ ,  $\beta'$ ,  $\alpha_1$ ,  $\sigma_k$ ,  $\sigma_{\omega 1}$ , and  $\sigma_{\omega 2}$  are constant values. Detailed definitions of the blending functions and the constant values can be found in the literature [117, 118].

# 7.2. A Proposed Design

In this section, a new impeller with a vaneless pinched diffuser is proposed according to the design procedure developed and the results will be investigated by considering the condensation margin (AMC). An inlet boundary condition in the liquid-like region, 310 K and 8.6 MPa, was

adopted to avoid the Widom region. It must be noted that the boundary conditions were chosen for the proposed compressor to operate in a 10 MWe s-CO<sub>2</sub> simple recuperated Brayton cycle and the design parameters were optimized to achieve the best possible design performance. The operating conditions and design parameters were shown in Table 10.

The results show that the inlet relative Mach number at the shroud  $(M_{w1s})$ , outlet tangential Mach number  $(M_{u2})$ , and exit Mach number  $(M_2)$  are well below the AMC to avoid condensation and stable compressor operation at the inlet and the outlet of the compressor. Moreover, according to Aungier [94], the relative velocity ratio  $(W_2/W_1)$  known as diffusion is a parameter to evaluate the effectiveness of the compressor design and stability. He suggested that a value around 0.75 is Table 10: Operating conditions and the design characteristics for the design point of the proposed s-CO<sub>2</sub> compressor suitable for 10 MWe power generation.

Rotational Speed, N (RPM)	20,000	Number of Blades, Z ()	18
•	88.79	Number of Splitters, S ()	9
Mass Flow Rate, $\dot{m}$ (kg/s)	00.19	Number of Spiniers, S ()	9
Inlet Total Pressure, $P_{01}$ (MPa)	8.6	Actual Stage Isentropic Efficiency, $\eta_{Act}$ ()	0.906
Inlet Total Temperature, $T_{01}$ (K)	310	Actual Total Pressure Ratio, $\pi_{Act}$ ()	2.38
Total Pressure Ratio, $\pi_0$ ()	2.7	AMC ()	0.56
Exit Blade Velocity, $u_2$ (m/s)	180	Inlet Shroud Relative Mach Number, $M_{w1s}$ ()	0.50
Inlet Hub Diameter, $d_{1,h}$ (mm)	45.1	Outlet Tangential Mach Number, $M_{u2}$ ()	0.54
Inlet Shroud Diameter, $d_{1,S}$ (mm)	86.2	Absolute Exit Mach Number, M <sub>2</sub> ()	0.45
Outlet Diameter, $d_2$ (mm)	17.9	Diffusion Along the Blade, $W_2/W_1$ ()	0.71
Outlet Blade Width, $b_2$ (mm)	6.5	Specific Speed, $N_{s,Balje}$ ()	0.694
Impeller Axial Length, $L_{axial}$ (mm)	39.3	Specific Diameter, $D_{s,Balje}$ ()	4.52
Inlet Hub Relative Angle, $\beta_{1,h}$ (deg)	32.9	Head Coefficient, $\psi$ ()	0.71
Inlet Shroud Relative Angle, $\beta_{1,S}$ (de	eg) 22	Stage Flow Coefficient, $\varphi_{Stage}$ ()	0.039
Relative Angle of Blade Outlet, $\beta_2$ (deg)	49.5	Wisner Slip Factor, $\sigma_{Wis.}$ ()	0.885

preferred; however, a design with a diffusion of less than 0.65 should be avoided for a stable operation. In the proposed design, the diffusion along the blades is 0.71 and is in the acceptable range as recommended by Aungier [94]. The detailed geometry, the impeller's blade angle distribution ( $\beta$ ), obtained from the developed 1-D code is shown in Figure 32.

Regarding the loss contributions in the compressor, it was found that 75.8% of the total enthalpy loss is due to internal losses. Specifically, the mixing loss has the highest portion of the total loss with the value of 17.8% while the incident loss of 6.5% has the lowest share of the total loss. On the other hand, the major external loss is due to the leakage with a value of 12.6% versus disk friction with only 4.4% of the total loss, as shown in Figure 33.

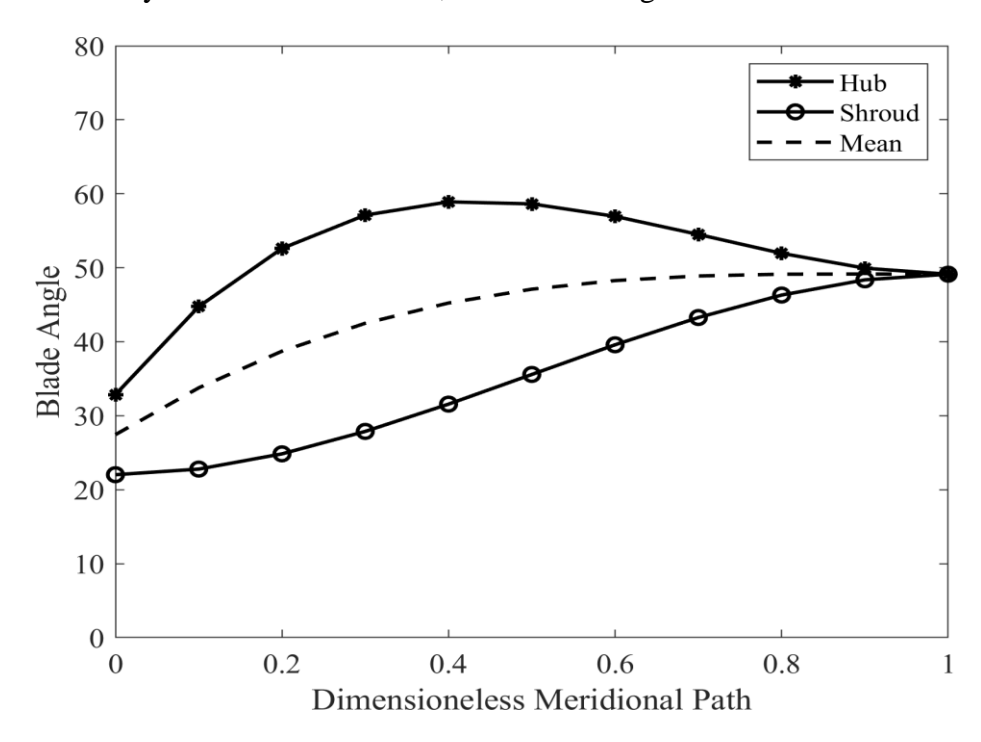


Figure 32: Blade angle distribution (β) of the proposed impeller for the s-CO<sub>2</sub> compressor.

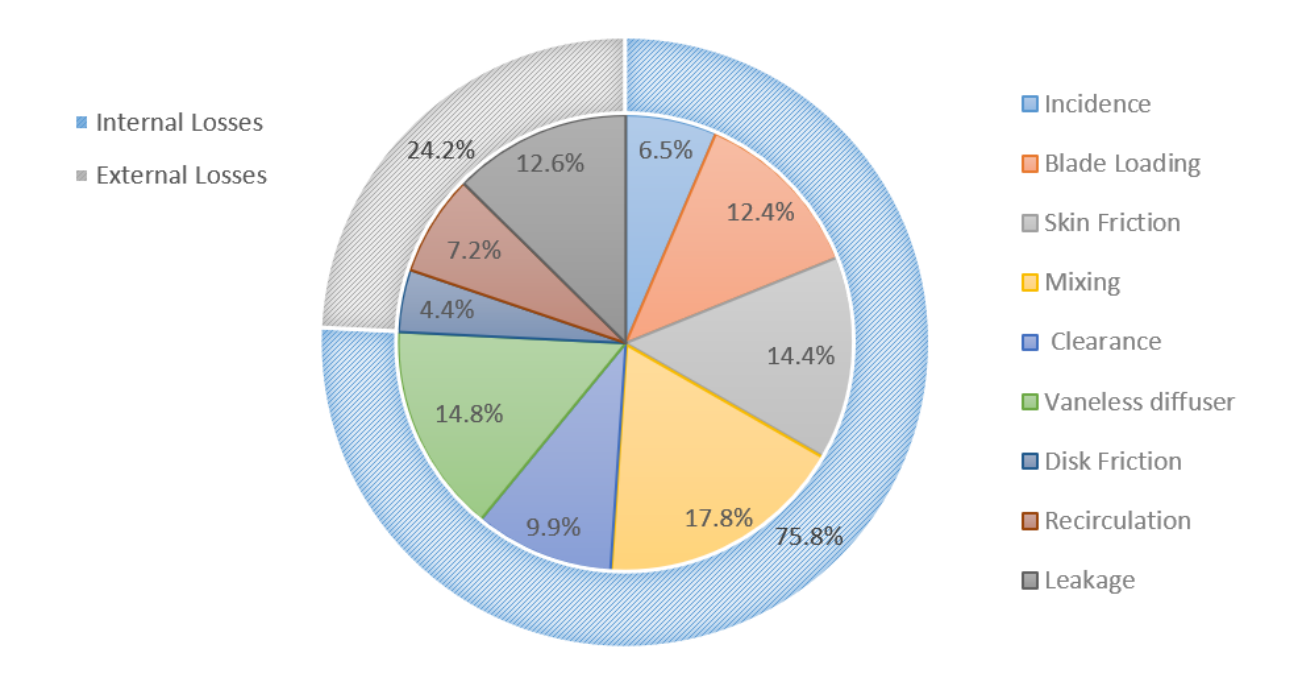


Figure 33: Internal and external loss distributions of the proposed s-CO<sub>2</sub> compressor at the design point.

However, the trends of the losses incurred are not similar at different mass flow rates and they can be categorized into three groups. The first group of losses such as blade loading and mixing losses decreases as the mass flow increases. The behavior of the second group of losses is marginal changes. That is, the losses either increase slightly, namely skin friction and clearance, or decrease marginally, i.e., vaneless diffuser, disk friction, and leakage, by increasing the mass flow rate. Finally, the losses of the third group involve exponential changes by increasing or decreasing the mass flow rate. Specifically, as the mass flow rate decreases, the recirculation loss increases dramatically and as the mass flow increases, the incidence loss increases markedly. These behaviors are demonstrated in Figure 34.

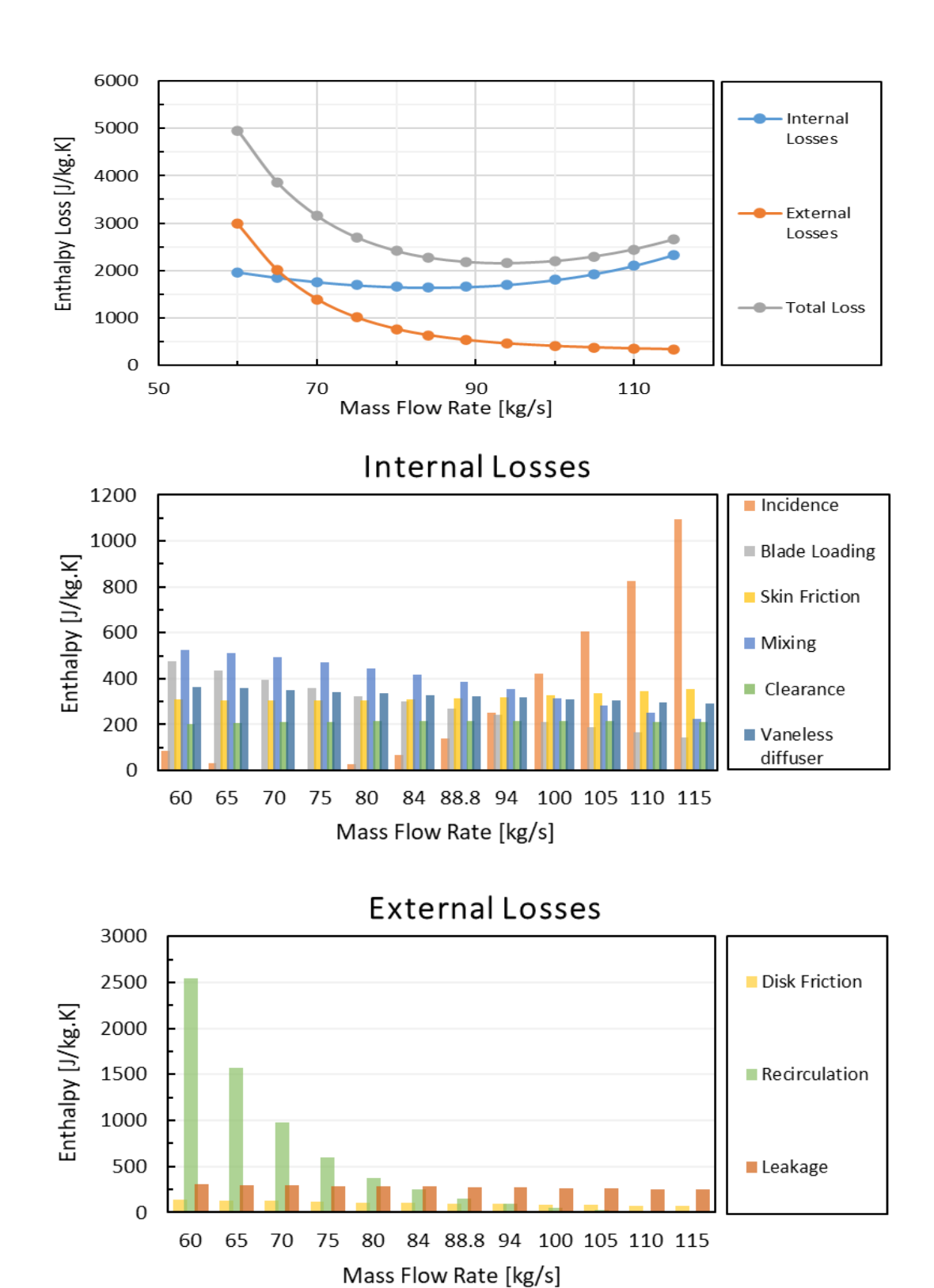


Figure 34: Internal and external loss distribution of the proposed s-CO<sub>2</sub> compressor at different mass flow rates obtained from the 1-D code.

To compare CFD with the 1-D results, the design parameters obtained from the 1-D code were utilized to generate the impeller. The design parameters were implemented in ANSYS BladeGen in the first place to obtain the 3-D geometry of the impeller. Then, a fully structured mesh of a single compressor passage is prepared in Turbogrid by using ATM topology for the numerical study. The mesh near-wall cell thickness is set in Turbogrid by targeting a Y+ value greater than 30 to minimize the element count of the model while keeping the mesh quality high. The dependency of the numerical solutions on mesh refinement [119-121] was checked by comparing the design-point CFD results obtained for four meshes with approximately 510k, 716k, 907k, and 1.34 million elements. Therefore, the finest mesh was selected as the baseline mesh for evaluating mesh dependence on important parameters such as  $\dot{m}$ , PR and  $\eta_{c,s}$ , and then the values obtained from simulations with other mesh sizes were compared and presented in Table 11. Mesh with approximately 716,000 elements produced acceptable results without any need for further mesh refinement. That is, the results for the selected mesh state that the mass flow rate, pressure ratio, and isentropic efficiency errors are below 1.05%. The 3-D geometry of the proposed compressor based on the 1-D code and the opted mesh are shown in Figure 35, and Figure 36, accordingly.

Table 11: Mesh independency study (the method adapted from [122]).

Number of Mesh	Mesh Size [mm]	<i>i</i> n [kg/s]	т <sub>егг</sub> [%]	<i>PR</i> [ - ]	PR <sub>err</sub> [%]	$oldsymbol{\eta}_{c,s}$ [%]	$oldsymbol{\eta_{cs,err}} [\%]$	Skewness [-]
509,549	0.46	89.12	0.73	2.356	1.41	91.075	0.51	0.704
715,636	0.41	89.27	0.56	2.365	1.02	91.166	0.41	0.705
907,149	0.38	89.49	0.32	2.368	0.92	91.241	0.33	0.705
1,343,354	0.34	89.77	base	2.390	base	91.540	base	0.704

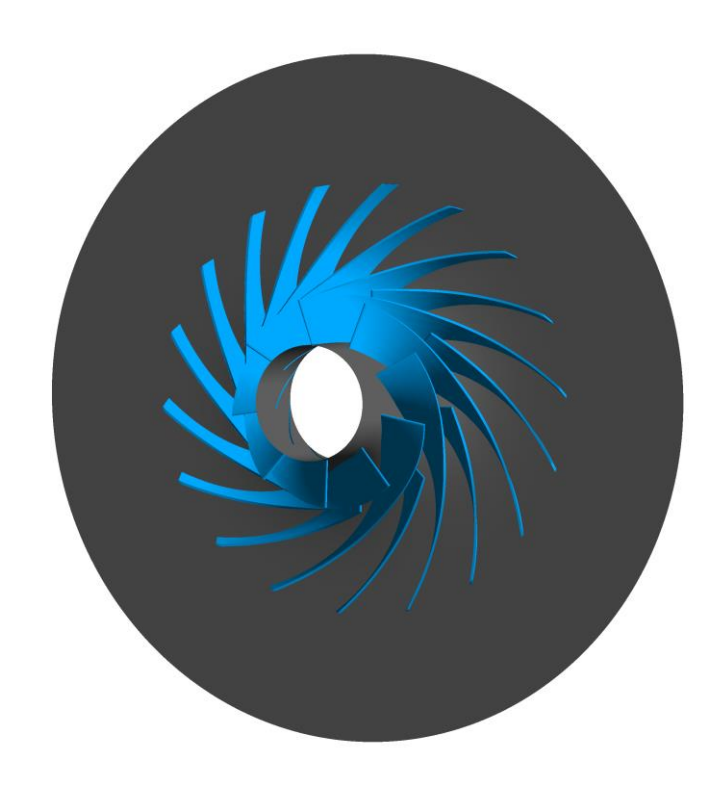


Figure 35: The 3-D geometry of the proposed compressor with a pinched diffuser generated in ANSYS BladeGen.

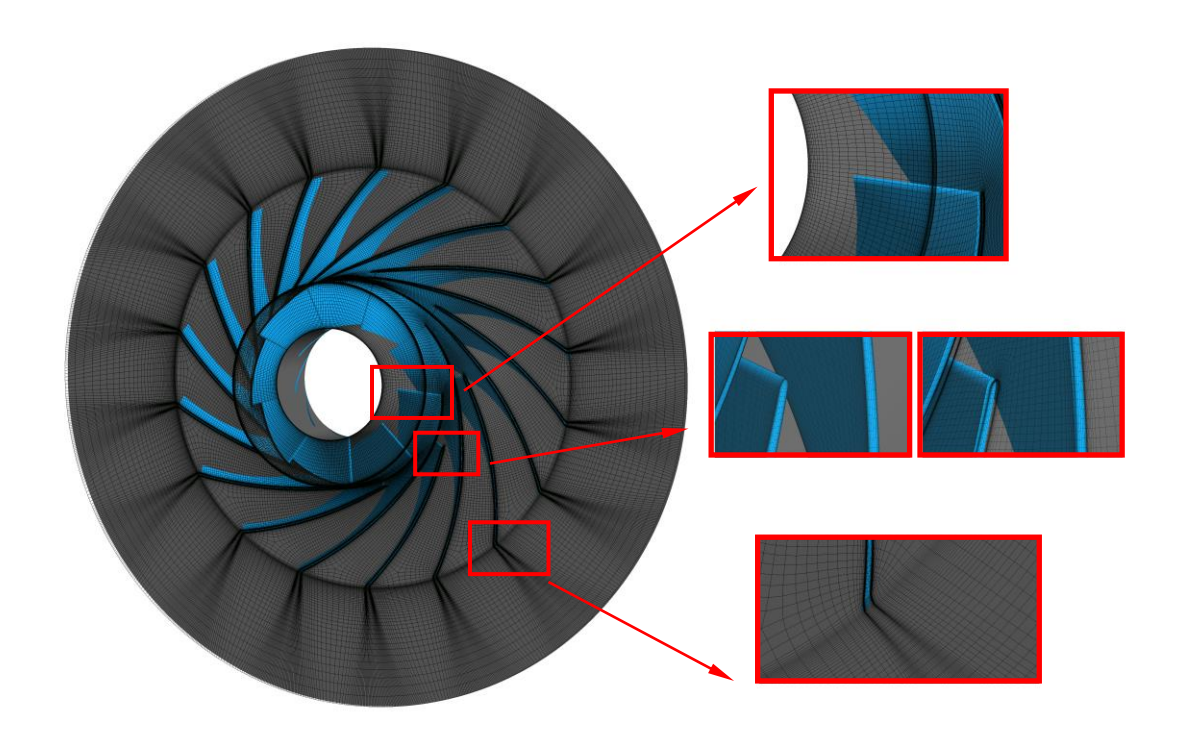


Figure 36: The opted mesh for the proposed compressor generated in ANSYS Turbogrid.

The generated mesh was imported to ANSYS CFX which is a CFD commercial tool specialized in turbomachinery simulations. In this software, steady-state Reynolds-Averaged Navier-Stokes (RANS) equations were solved with double precision to validate the compressor design at the design point of the simple recuperated cycle. The k-ω Shear Stress Transport (SST) was selected for the CFD study. Further, the flow advection schemes, and the turbulence model were set at high resolution.

Regarding the boundary conditions, total pressure and total temperature were used at the compressor inlet with the values of 8.6 MPa, and 310 K, respectively. Also, the mass flow rate boundary condition is applied at the outlet of the compressor with a magnitude of 88.79 kg/s for the hole machine at the design point. Adiabatic wall boundary condition was selected for the blade's wall. Besides, three domains were defined including the inlet, rotor, and diffuser sections. While the inlet and the diffuser sections were considered stationary domains, the rotor domain was set to rotating. On the shroud side of the impeller, the boundary condition was defined as a counterrotating wall to assign the no-slip condition at the shroud. Further, the Mixing-Plane model was utilized for the interfaces between the rotating (impeller) and the stationary domains. It is noted that due to the closeness of the compressor inlet conditions to the critical point, a slight drop in temperature and pressure of the flow in the compressor channel would result in a phase change. Phase change flows in CFX can be studied using homogeneous or inhomogeneous multiphase models. For this study, a homogeneous binary mixture model is employed to predict the mass fraction of the condensed vapor. The real gas properties of CO<sub>2</sub> for liquid, vapor, and saturated states are defined by look-up tables generated from the NIST REFPROP fluid library. The NIST REFPROP database uses the Span-Wagner equation of states which is known as the most accurate EOS for supercritical fluids. Four real gas property (RGP) tables with sampling resolutions ranging

from low to very high were prepared using a Python script obtained from Fluent Beta Features Manual [123]. A very-high-resolution (interpolation error of 1e-5) RGP table in the temperature range of 250-600 K and pressure range of 0.01-90 MPa was defined to compute the thermophysical properties in the CFD tool. To address the convergence challenge faced in the simulation process, the first-order upwind method was used for the discretization of the turbulence model and advection terms at the beginning of the simulation. As the solution progressed, the discretization method was changed to high resolution to achieve higher accuracy. Also, pressure-velocity coupling with high resolution was employed later in the simulation process to improve the accuracy and lead to the reduction of mass imbalance. Furthermore, the physical time step was used and set to 1e-7 s and increased gradually during the simulation for stability purposes. It is worth mentioning that the CFX solver employs a false time step in a steady-state simulation to under-relax the equations until reaching the final solution. The result of the CFD simulation was compared with the 1-D code for the design point and presented in Table 12.

Table 12: The comparison between the developed 1-D code and the CFD results.

	T-T Actual Efficiency	Total Pressure Ratio
1-D	90.62%	2.38
CFD	91.46%	2.39

Further, the performance plots from the 1-D design code stipulate that the code could perfectly follow and fairly match the CFD results with the error margin of 2.3% and 0.6% on average for the total-to-total efficiency and pressure ratio respectively, as shown in Figure 37.

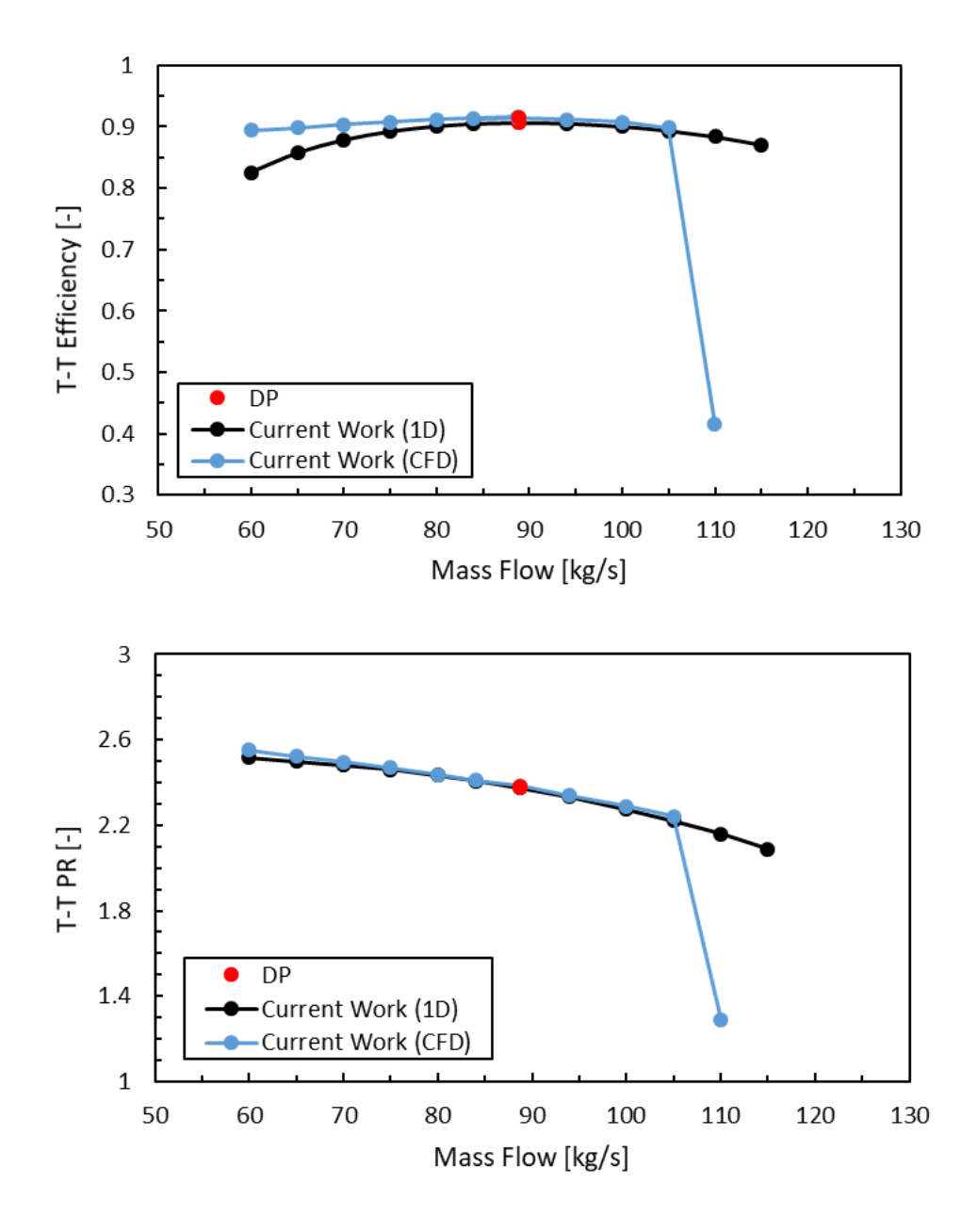


Figure 37: Comparison of the developed 1-D code and CFD performance plots.

One of the characteristics the current design boasts is the high operation range (OR) which is defined as follows:

$$OR = \frac{\dot{m}_{Choke} - \dot{m}_{Surge}}{\dot{m}_{Choke}} \tag{102}$$

The results confirm an excellent operational range of approximately 47.8%, and 42.8% based on the 1-D code, and CFD results, respectively. The high operating range denotes that there is a safe margin, far from choke and surge conditions that the compressor can operate safely.

#### 7.3. CFD Results

To study the flow behavior inside the impeller, relative Mach number contours were studied at 10%, 50%, and 90% spans, as shown in Figure 38. It is evident from this figure that for the lower limit in the performance map, the mass flow of 60 kg/s, the impeller is close to the surge condition. That is, local mild stalls are present in the impeller where the flow was separated from the blade, especially at 10% and 90%, as predicted by the developed 1-D code. On the other hand, the flow is completely choked at the entrance of the splitters for the higher limit in the performance map, the mass flow of 110 kg/s, and behaves the same as the throat of a converging-diverging nozzle, as shown in Figure 39. In simpler terms, the supercritical CO<sub>2</sub> with a high speed enters the flow path of the impeller's main blade and acts as the converging part of a converging-diverging nozzle. Further, the relative Mach number increases until the flow is choked at the entrance of the splitters, in which functions as the throat of the converging-diverging nozzle, and it reaches  $M_{Rel}$ =1. Since the flow path expands close to the exit of the impeller, the relative Mach number keeps developing and serves as the diverging part of the converging-diverging nozzle, until it reaches  $M_{Rel}=1.3$  at the exit of the impeller. Finally, the flow tries to adapt itself to the exit of the impeller and a complex shock pattern is formed with a mixture of supersonic and subsonic flow. This conclusion can be also drawn from the Area Circumferential Averaged (ACA) Relative Mach Number plot, as shown in Figure 39. It must be noted that the graphs plotted in this figure are the area circumferential averaged values of the relative Mach number. In other words, while there

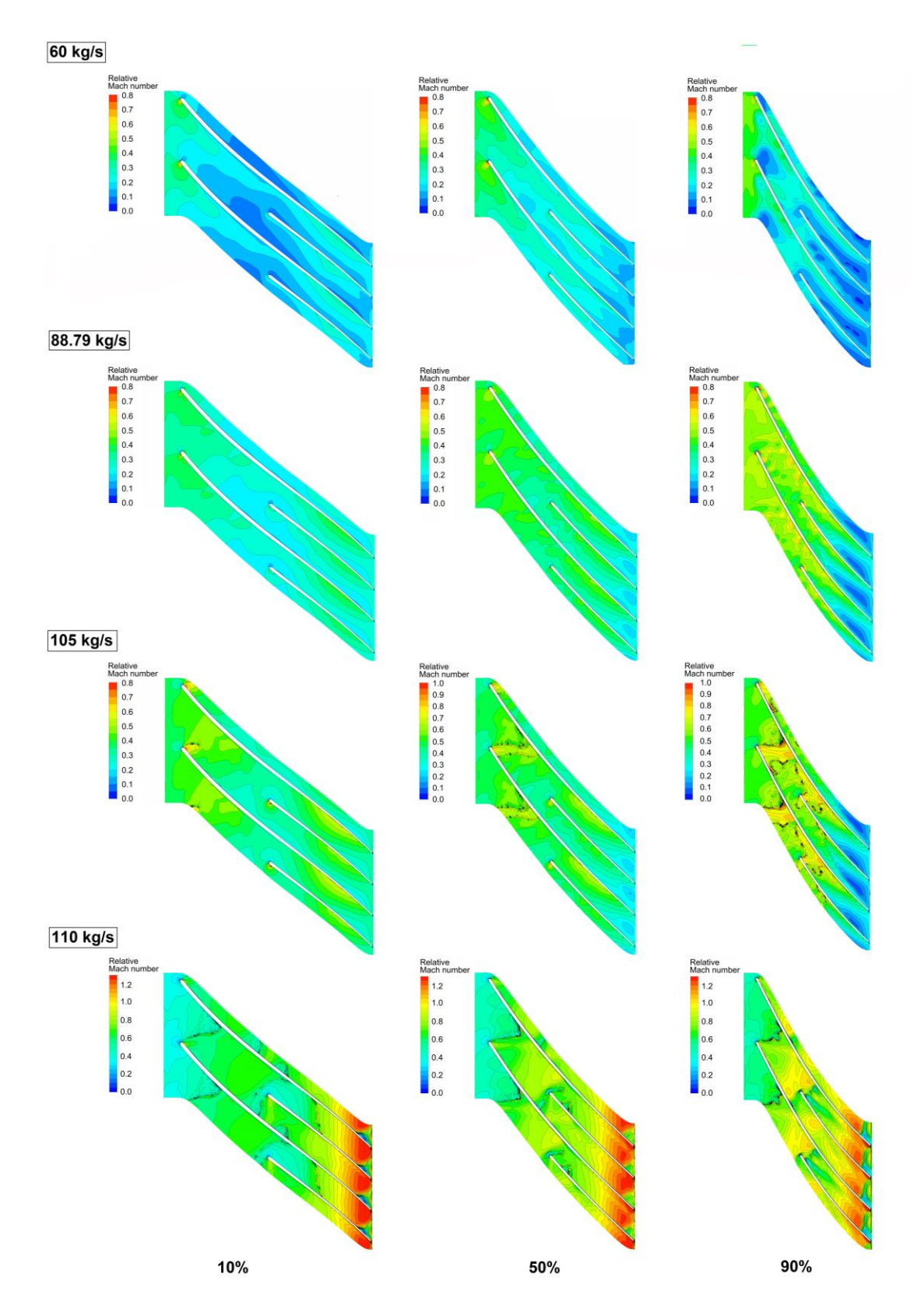


Figure 38: Relative Mach number contours at different mass flow rates for 10%, 50%, and 90% spans.

could be locally higher Mach numbers in a fixed meridional path, in another pitch value the relative Mach number might be lower. Moreover, the high relative Mach number in the impeller implies the low local pressures leading to condensation and it increases as the operating point of the compressor gets closer to the choke point, as also discussed in [57]. Furthermore, the impeller is flooded with liquid carbon dioxide for a mass flow rate of 110 kg/s, as shown in Figure 40. The results demonstrate that condensation is an inevitable part of an s-CO<sub>2</sub> compressor's operation. However, an important question to be answered is if the condensation is interfering with the compressor's performance or causing any damage to the blades. To answer this question, a closer examination of the liquid mass fraction contours shows that a small area of condensation occurs only on the suction side of the impeller for the mass flow rates below 70 kg/s. However, as the flow rate increases, the condensation develops further to the pressure section of the blades. Further, for the mass flow beyond the higher limit in the compressor performance map (105kg/s), flow is choked with a mixture of liquid and vapor CO<sub>2</sub>. So, this conclusion can be drawn from Figure 37 that condensation does not affect the compressor performance. Also, since pure CO<sub>2</sub> is not corrosive, this is not a major concern unless water or other contaminations such as metal particulates are entrained into the compressing system which may result in corrosion, as discussed in [124, 125]. In other words, when carbon dioxide (CO<sub>2</sub>) reacts with water (H<sub>2</sub>O) produces carbonic acid (H<sub>2</sub>CO<sub>3</sub>) which is corrosive. The chemical reaction is as follows:

$$CO_2 + H_2O \rightarrow H_2CO_3$$
 (103)

Nonetheless, while the 1-D code underestimates the choking line at the high limit marginally, the performance plots obtained from CFD fairly match the results from the developed 1-D code.

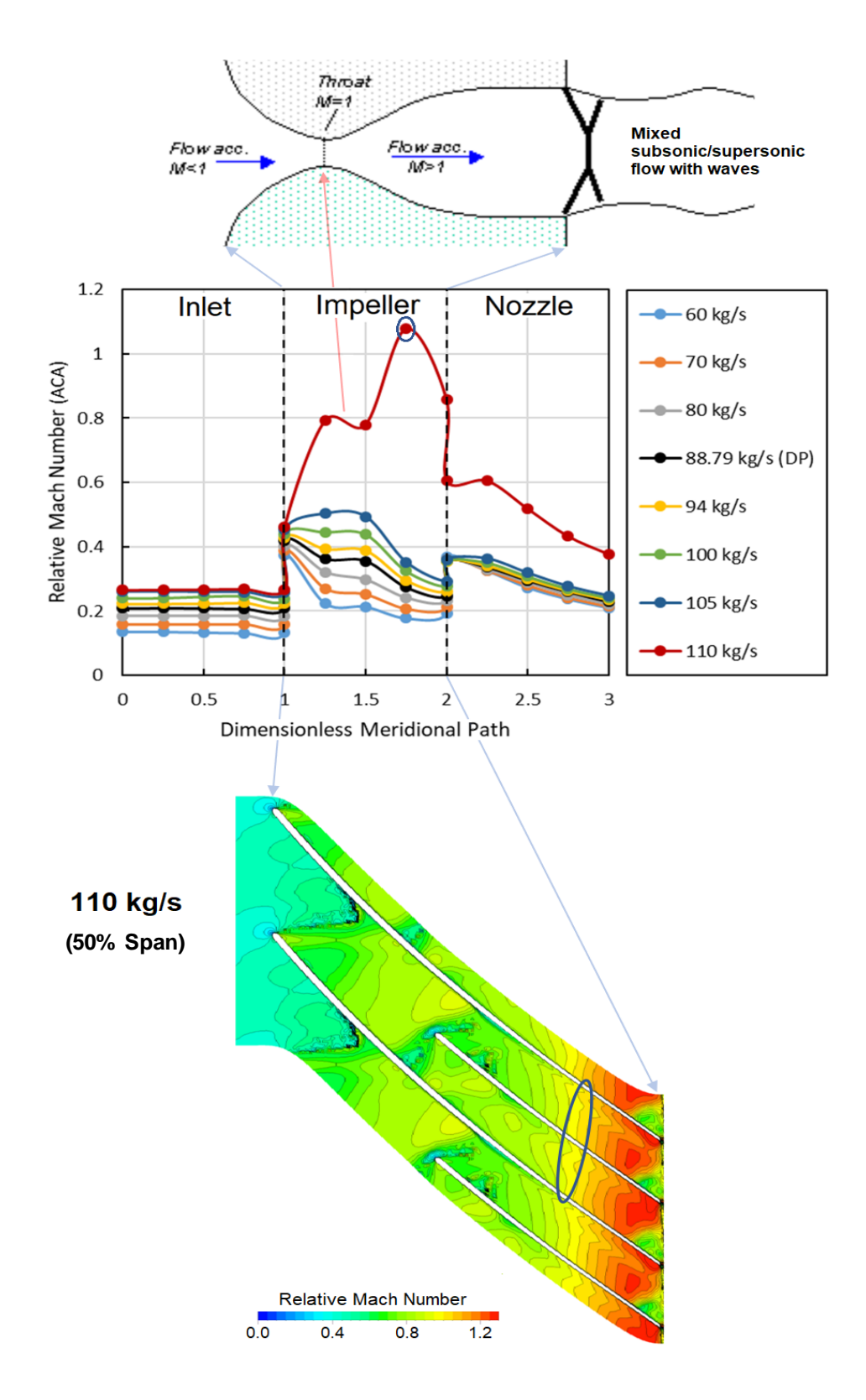


Figure 39: Relative Mach number (ACA) behavior inside the compressor at different mass flow rates (the converging-diverging nozzle figure was adapted from [126]).

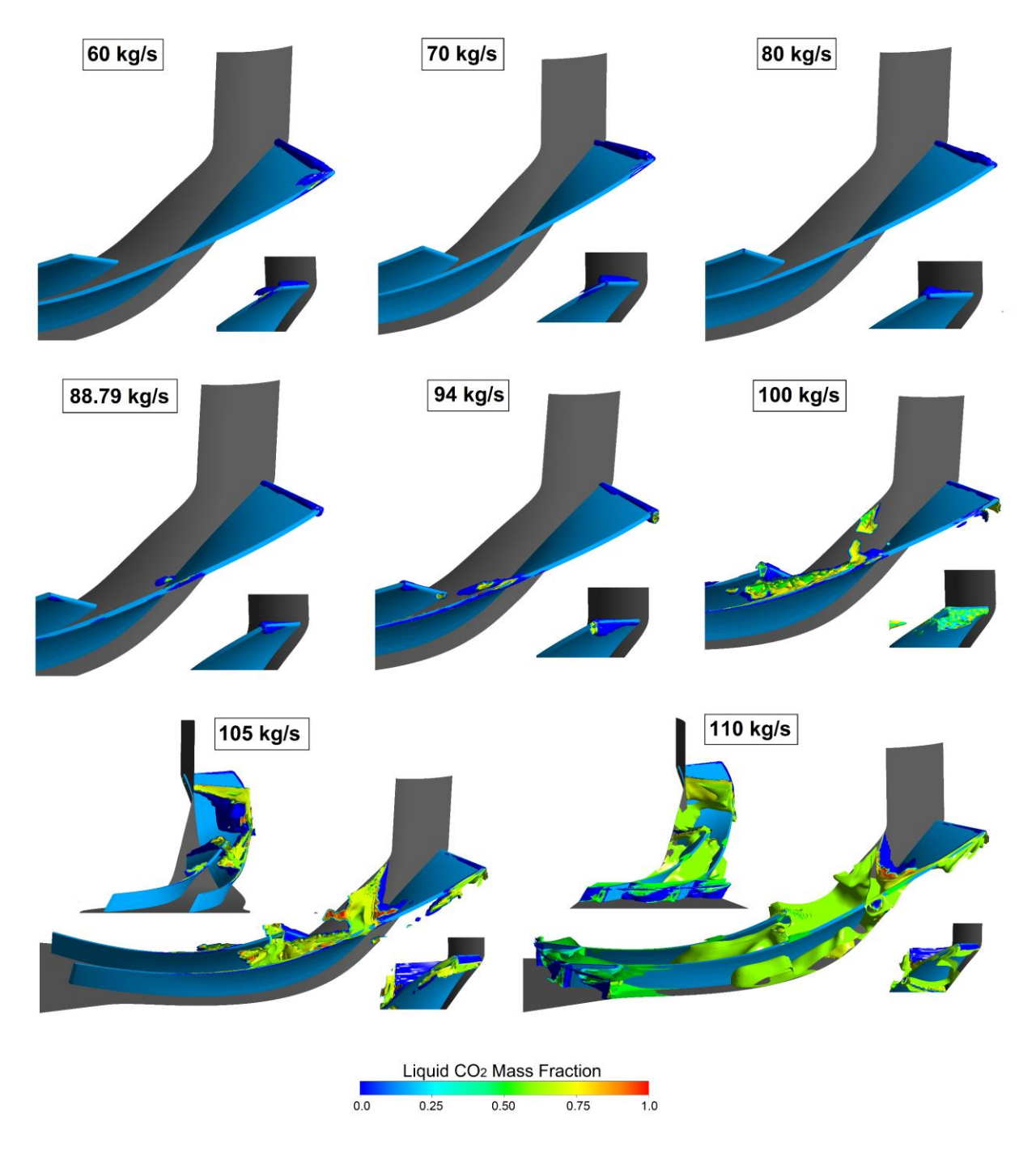


Figure 40: Liquid mass fraction contours inside the impeller at different mass flow rates.

### **CHAPTER 8: CONCLUSION**

While s-CO<sub>2</sub> power generation is highly attractive and promising, there are several design challenges that need to be addressed including developing turbomachinery (mainly the compressor), heat exchangers, and seals and bearings. Currently, in s-CO<sub>2</sub> technology, the race is to develop a working 10 MWe s-CO<sub>2</sub> Brayton Cycle Gas Turbine. Priority-wise, since the compressor development is the likely component that needs more attention, the main focus of this work was dedicated to the compressor design for the 10 MWe s-CO<sub>2</sub> Brayton cycle.

In this dissertation, three s-CO<sub>2</sub> Brayton cycles were reconfigured, namely simple recuperated, recompression, and dual turbine cycles. The performance parameters of the cycles were opted such that to produce 11.11 MW output net power, or 10 MWe (electric) power. To better compare the efficiency and the performance of the cycles, the same input parameters, namely maximum temperature and pressure, isentropic efficiency of compressor and turbine, mechanical efficiency, and compressor pressure ratio were considered in the cycle analysis. The results were compared to the simple (conventional) Brayton cycle as the basic s-CO<sub>2</sub> layout. Regarding the cycle efficiency, the recompression scheme had the highest value of 54.2% compared to the simple, simple recuperated, and dual turbine. However, the ratio of compressor input power to turbine output power (back-work ratio) was the highest, 28.3%, for the recompression cycle with the lowest specific work, 109.16 kJ/kg. The thermal efficiency for the simple recuperated cycle was 43.2% with the specific work of 125.13 kJ/kg which is in the moderate range between the two limits of the dual turbine cycle (lowest efficiency but highest specific work) and recompression cycle (highest efficiency but lowest specific work). Hence, the simple cycle can be a viable option for 10 MWe s-CO<sub>2</sub> Brayton cycle commercialization. The lower capital cost compared to the recompression cycle, namely, fewer turbomachinery components underpin this suggestion.

Further, a new compressor design procedure was introduced based on the continuity and Euler equations within which internal and external (parasitic) losses were considered. The internal losses include incidence, blade loading, skin friction, tip-clearance, mixing, choke, and vaneless diffuser losses while leakage, recirculation, and disc friction losses are categorized as external losses. In the design procedure, Acceleration to Condensation Margin (AMC) and Widom region checks were included in the code to ensure avoiding reaching AMC and Widom regions when the appropriate boundary condition is desired for the s-CO<sub>2</sub> compressors. The developed 1-D code includes a pinched diffuser based on the Aungier method [94].

To test the accuracy of the 1-D developed design code, it was validated with the experimental results performed by Eckardt [113-115] for the air compressors. The code was modified for the air compressor within which ideal gas law was utilized to validate the procedure of the compressor design by using the 1-D code with the Eckardt Impeller-A to produce his results and geometry with reasonable accuracy. The efficiency and pressure ratio obtained from the 1-D code were compared to CFD results and showed reasonable agreement with experimental data. However, at higher mass flow rates, there was overprediction due to the lack of consideration of the volute in the design. While the 1-D code was validated with an air compressor, it was essential to examine the validity of the developed meanline code with an s-CO<sub>2</sub> compressor data since supercritical CO<sub>2</sub> behaves differently. Thus, the 1-D code was modified to replicate Sandia's compressor by using the Span-Wagner equation of state. Then, the design parameters were implemented in BladeGen to obtain the 3-D geometry of the impeller and a fully structured mesh of a single compressor passage was prepared in Turbogrid by using ATM topology for the numerical study. The CFD simulation was performed in ANSYS CFX by considering a two-phase model to capture the condensation. By comparing the total-to-static efficiency of Sandia's compressor (the only

available performance plot) at 50,000 RPM with 1-D code and CFD, it was found that while the CFD results match the experimental data, the 1-D code could not calculate the total-to-static efficiency of Sandia's compressor for the mass flow rates below 2.5 kg/s. The author believes it could be due to the following reasons:

- (1) some assumptions were made in the design procedure, i.e., the Aungier method was used for vaned diffuser sizing to replicate the Sandia compressor in the 1-D code and the details of the vane's shape were not reported,
- (2) the measured data were reported in terms of corrected mass flow based on a reference value not known to the author, resulting in a misalignment between the measured data, the CFD results, and the 1-D code, and
- (3) the total temperature and pressure at the inlet of the Sandia's compressor are 305.3 K and 7.69 MPa which are equivalent to the static temperature and pressure of 293.7 K and 5.8 MPa which are well below the saturation line. Since the code cannot evaluate the speed of sound in the two-phase region, the code cannot run the performance map below this value.

Furthermore, a new impeller with a vaneless pinched diffuser was proposed according to the design procedure developed and the results were investigated while considering the condensation margin (AMC). To avoid the Widom region, an inlet boundary condition was selected in the liquid-like region, 310 K and 8.6 MPa. The boundary conditions were chosen such that to operate in a 10 MWe s-CO<sub>2</sub> Brayton cycle and the design parameters were optimized to achieve the best possible design performance. The result showed that the compressor efficiency was 90.62% with an excellent operating range of 47.8%. The 1-D results were also compared with the simulation for different mass flow rates at the design speedline of 20,000 RPM, which closely matched. Additionally, the internal behavior of s-CO<sub>2</sub> was studied at the choked condition, and a new

analogy between the compressor and a converging-diverging nozzle was made for the high limit of the performance map. Besides, a loss analysis in the proposed s-CO<sub>2</sub> compressor was performed, revealing that 75.8% of the total enthalpy loss was due to internal losses. Specifically, the mixing loss had the highest portion, 17.8%, while the incident loss of 6.5% possessed the lowest share of the total loss. On the other hand, the majority of the external loss was due to leakage with a value of 12.6% versus disk friction with only 4.4% of the total loss. Finally, the condensation plots illuminated that condensation is unavoidable in an s-CO<sub>2</sub> centrifugal compressor; however, the condensation does not cause damage or affect the compressor's performance.

Future work is required to focus on developing compressor test facilities to obtain more reliable experimental data with boundary conditions not being close to the saturation line and supercritical point, preferably in the liquid-like region. Having the experimental data helps to develop new correlations for the internal and external losses that predict the performance plots of s-CO<sub>2</sub> compressors more accurately. Also, examining boundary selection in the vapor-like region and its effect on the performance plots (efficiency and pressure ratio) must be studied. Although it was found that selecting a boundary condition in the liquid-like region leads to the higher efficiency of the compressor and power cycle accordingly, the results show that condensation is inevitable in this region. Therefore, examining the performance plots of an s-CO<sub>2</sub> compressor working in the vapor-like region must be studied in detail to evaluate whether the lower efficiency of the s-CO<sub>2</sub> compressor in the vapor-like region is worth avoiding condensation or not.

## **BIBLIOGRAPHY**

- [1] D. Fleming, T. Holschuh, T. Conboy, J. Pasch, S. Wright and G. Rochau, "Scaling Considerations for a Multi-Megawatt Class Supercritical CO<sub>2</sub> Brayton Cycle and Path Forward for Commercialization," in ASME Turbo Expo, Copenhagen, Denmark, 2012.
- [2] H. D. Madhawa Hettiarachchi, M. Golubovic, W. M. Worek and Y. Ikegami, "Optimum design criteria for an Organic Rankine cycle using low-temperature geothermal heat sources," Energy, vol. 32, pp. 1698-1706, 2007.
- [3] S. J. Zarrouk and M. Hyungsul, "Efficiency of Geothermal Power Plants: A Worldwide Review," Geothermics, vol. 51, pp. 142-153, 2014.
- [4] S. Qazi, Standalone Photovoltaic (PV) Systems for Disaster Relief and Remote Areas, Elsevier, 2016.
- [5] T. Tanuma, Advances in Steam Turbines for Modern Power Plants, 1st ed., Woodhead Publishing, 2017.
- [6] M. Wiatros-Motyka, An Overview of HELE Technology Deployment in the Coal Power Plant Fleets of China, EU, Japan and USA, IEA Clean Coal Center, 2016.
- [7] G. Locatelli, M. Mancini and N. Todeschini, "Generation IV Nuclear Reactors: Current Status and Future Prospects," Energy Policy, vol. 61, pp. 1503-1520, 2013.
- [8] Y. Ahn, S. J. Bae, M. Kim, S. K. Cho, S. Baik, J. I. Lee and J. E. Cha, "A Review of Supercritical CO<sub>2</sub> Power Cycle Technology and Current Status of Research and Development," Nuclear Engineering and Technology, vol. 47, pp. 647-661, 2015.
- [9] P. Jansohn, Modern Gas Turbine Systems: High Efficiency, Low Emission, Fuel Flexible Power Generation, 1st ed., Elsevier, 2013.
- [10] J. Chen and A. Engeda, "A Review of The Prospect and Challenges for Developing and Marketing a Brayton-Cycle Based Power Genset Gas-Turbine Using Supercritical CO<sub>2</sub>: Part I," in ASME Turbo Expo, Virtual, Online, 2020.
- [11] G. Sulzer, "Verfahren zur Erzeugung von Arbeit aus Warme". Swiss Patent 269599, 1950.
- [12] G. Angelino, "Carbon Dioxide Condensation Cycles for Power Production," Engineering Power, vol. 90, pp. 287-295, 1968.
- [13] E. G. Feher, "The Supercritical Thermodynamic Power Cycle," Energy Conversion, vol. 8, pp. 85-90, 1968.
- [14] K. Brun, P. Friedman and R. Dennis, Fundamentals and Applications of Supercritical Carbon Dioxide (sCO<sub>2</sub>) Based Power Cycles, 1st ed., Woodhead Publishing, 2017.

- [15] M. J. Moran and H. N. Shapiro, Fundamentals of Engineering Thermodynamics, Wiley, 2004.
- [16] A. U. Schroder, A Study of Power Cycles Using Supercritical Carbon Dioxide as the Working Fluid, PhD dissertation, University of Cincinnati, 2016.
- [17] J. R. Culham, "Brayton Cycles," [Online]. Available: <a href="http://www.mhtl.uwaterloo.ca/courses/me354/lectures/pdffiles/c8.pdf">http://www.mhtl.uwaterloo.ca/courses/me354/lectures/pdffiles/c8.pdf</a>. [Accessed 12 April 2021].
- [18] G. Subbaraman, J. A. Mays, B. Jazayeri, K. M. Sprouse, A. H. Eastland, S. Ravishankar and C. G. Sonwane, "Energy Systems, Pratt and Whitney Rocketdyne, ZEPS Plant Model: A High Efficiency Power Cycle with Pressurized Fluidized Bed Combustion Process," in 2nd Oxyfuel Combustion Conference, Queensland, Australia, 2011.
- [19] A. Kacludis, S. Lyons, D. Nadav and E. Zdankiewicz, "Waste Heat to Power (WH2P) Applications Using a Supercritical CO<sub>2</sub>-Based Power Cycle," in Power-Gen International, Orlando, FL, 2012.
- [20] W. W. Shelton, N. Weiland, C. White, J. Plunkett and D. Gray, "Oxy-Coal-Fired Circulating Fluid Bed Combustion with a Commercial Utility-Size Supercritical CO<sub>2</sub> Power Cycle," in 5th Supercritical CO<sub>2</sub> Power Cycles Symposium, San Antonio, TX, 2016.
- [21] J. I. Linares, M. J. Montes, A. Cantizano and C. and Sánchez, "A novel Supercritical CO<sub>2</sub> Recompression Brayton Power Cycle for Power Tower Concentrating Solar Plants," Applied, vol. 263, 2020.
- [22] S. Wright, C. Davidson and W. Scammell, "Thermo-Economic Analysis of Four SCO<sub>2</sub> Waste Heat Recovery Power Cycle Systems," in 5th Supercritical CO<sub>2</sub> Power Cycles Symposium, San Antonio, TX, 2016.
- [23] M. Bauer, "Pathway to Cost Competitive Concentrated Solar Power Via Supercritical CO<sub>2</sub> Power Cycles," in 5th Supercritical CO<sub>2</sub> Power Cycles Symposium, San Antonio, TX, 2016.
- [24] J. D. Osorio, R. Hovsapian and J. C. Ordonez, "Effect of Multi-Tank Thermal Energy Storage, Recuperator Effectiveness, and Solar Receiver Conductance on the Performance of a Concentrated Solar Supercritical CO<sub>2</sub>-Based Power Plant Operating Under Different Seasonal Conditions," Energy, vol. 115, pp. 353-368, 2016.
- [25] T. Abram and S. Ion, "Generation-IV Nuclear Power: A Review of the State of the Science," Energy Policy, vol. 36, pp. 4323-4330, 2088.
- [26] E. Lemmon, I. Bell, M. Huber and M. McLinden, NIST Standard Reference Database 23: Reference Fluid Thermodynamic and Transport Properties-REFPROP, Version 10.0, National Institute of Standards and Technology, Standard Reference Data Program, Gaithersburg, 2018.

- [27] R. Drew, "Special Report Supercritical CO<sub>2</sub> the Next Big Step?," The Global Journal of Energy Equipment Turbomachinery International, vol. 53, pp. 22-28, 2012.
- [28] V. Dostal, A Supercritical Carbon Dioxide Cycle for Next Generation Nuclear Reactors, PhD dissertation, Advanced Nuclear Power Technology Program, Boston, MA: Advanced Nuclear Power Technology Program, MIT, 2004.
- [29] S. Patel, "What Are Supercritical CO<sub>2</sub> Power Cycles," Power Mag, April 1, 2019.
- [30] Y. L. Moullec, "Conceptual Study of a High Efficiency Coal-Fired Power Plant with CO<sub>2</sub> Capture Using a Supercritical CO<sub>2</sub> Brayton Cycle," Energy, vol. 49, pp. 32-46, 2013.
- [31] J. A. Ashcroft, K. J. Kimball and M. R. Corcoran, "Overview of Naval Reactors Program Development of the Supercritical Carbon Dioxide Brayton System," in Power Cycle Symposium, Troy, NY, 2009.
- [32] K. J. Kimball and E. M. Clementoni, "Supercritical Carbon Dioxide Brayton Power Cycle Development Overview," in ASME Turbo Expo, Copenhagen, Denmark, 2012.
- [33] E. M. Clementoni, T. L. Cox and C. P. Sprague, "Startup and Operation of a Supercritical Carbon Dioxide Brayton Cycle," Journal of Engineering for Gas Turbines and Power, vol. 136, 2014.
- [34] J. Pasch, T. Conboy, D. Fleming and G. Rochau, "Supercritical CO<sub>2</sub> Recompression Brayton Cycle: Completed Assembly Description," Sandia National Laboratories, Albuquerque, New Mexico and Livermore, California, 2012.
- [35] B. D. Iverson, T. M. Conboy, J. J. Pasch and A. M. Kruizenga, "Supercritical CO<sub>2</sub> Brayton Cycles for Solar-Thermal Energy," Applied Energy, vol. 111, pp. 957-970, 2013.
- [36] K. Wang, Y.-L. He and H.-H. Zhu, "Integration Between Supercritical CO<sub>2</sub> Brayton Cycles and Molten Salt Solar Power Towers: A Review and a Comprehensive Comparison of Different Cycle Layouts," Applied Energy, vol. 195, pp. 819-836, 2017.
- [37] J. Moore, Brun, E. N. K. and K. Chiranjeev, "Development of 1 MWe Supercritical CO<sub>2</sub> Test loop," in ASME Turbo Expo, Montréal, Canada, 2015.
- [38] J. Moore, C. S., M. Towler, T. Allison, J. Wade and D. Hofer, "Commissioning of a 1 MWe Supercritical CO<sub>2</sub> Test Loop," in Supercritical CO<sub>2</sub> Power Cycle Symposium, Pittsburgh, PA, 2018.
- [39] H. Li, Y. Zhang, M. Yao, Y. Yang, W. Han and W. Bai, "Design Assessment of a 5 MW Fossil-Fired Supercritical CO<sub>2</sub> Power Cycle Pilot Loop," Energy, vol. 174, pp. 792-804, 2019.
- [40] Y. L. Moullec, Z. Qi, J. Zhang, P. Zhou, Z. Yang, X. Wang, W. Chen and S. Wang, "Shouhang-EDF 10MWe Supercritical CO<sub>2</sub> Cycle + CSP Demonstration Project," in 3rd European Supercritical CO<sub>2</sub> Conference, Paris, France, 2019.

- [41] F. Crespi, G. Gavagnin, D. Sanchez and G. S. Martınez, "Analysis of the Thermodynamic Potential of Supercritical Carbon Dioxide Cycles: A Systematic Approach," Journal of Engineering for Gas Turbines and Power, vol. 140, 2018.
- [42] Y. Wang, G. Guenette, P. Hejzlar and M. Driscoll, "Compressor Design for the Supercritical CO<sub>2</sub> Brayton cycle," in 2nd International Energy Conversion Engineering Conference, Providence, Rhode Island, 2004.
- [43] Y. Gong, N. A. Carstens, M. J. Driscoll and I. A. Mathews, "Analysis of Radial Compressor Options for Supercritical CO<sub>2</sub> Power Conversion Cycles," Center for Advanced Nuclear, MIT, Cambridge, MA, 2006.
- [44] S. A. Wright, R. F. Radel, M. E. Vernon, G. E. Rochau and P. S. Pickard, "Operation and Analysis of a Supercritical CO<sub>2</sub> Brayton Cycle," Sandia National Laboratories, Albuquerque, New Mexico, and Livermore, California, 2010.
- [45] M. Utamura, H. Hasuike, K. Ogawa, T. Yamamoto, T. Fukushima, T. Watanabe and T. Himeno, "Demonstration of Supercritical CO<sub>2</sub> Closed Regenerative Brayton Cycle in a Bench Scale Experiment," in ASME Turbo Expo, Copenhagen, Denmark, 2012.
- [46] S. J. Bae, Y. Ahn, H.-S. Lim, J. E. Cha and J. I. Lee, "Comparison of Gas System Analysis Code GAMMA+ to S-CO<sub>2</sub> Compressor Test Data," in ASME Turbo Expo, Montréal, Canada, 2015.
- [47] J. Lee, J. I. Lee, Y. Ahn and H. Yoon, "Design Methodology of Supercritical CO<sub>2</sub> Brayton Cycle Turbomachineries," in ASME Turbo Expo, Copenhagen, Denmark, 2012.
- [48] B. Bartosz Kus, Oil-Free Turbocompressors for CO<sub>2</sub> as Working Fluid, Ph.D. Thesis, Norway: Noewgian University of Science and Technology, 2013.
- [49] J. Lee, S. K. Cho, J. E. Cha and J. I. Lee, "Sensitivity Study of S-CO<sub>2</sub> Compressor Design for Different Real Gas Approximations," in ASME Turbo Expo, Seoul, South Korea, 2016.
- [50] [Online]. Available: <a href="https://www.conceptsnrec.com/blog/does-meanline-design-still-make-sense-in-the-era-ofcfd-and-optimization">https://www.conceptsnrec.com/blog/does-meanline-design-still-make-sense-in-the-era-ofcfd-and-optimization</a>. [Accessed 9 6 2021].
- [51] N. D. Baltadjiev, C. Lettieri and Z. S. Spakovszky, "An Investigation of Real Gas Effects in Supercritical CO<sub>2</sub> Centrifugal Compressors," Journal of Turbomachinery, vol. 137, 2015.
- [52] R. Pecnik, E. Rinaldi and P. Colonna, "Computational Fluid Dynamics of a Radial Compressor Operating with Supercritical CO<sub>2</sub>," Journal of Engineering for Gas Turbines and Power, vol. 134, 2012.
- [53] B. Monje, D. Sánchez, M. Savill, P. Pilidis and T. Sánchez, "A Design Strategy for Supercritical CO<sub>2</sub> Compressors," in ASME Turbo Expo, Düsseldorf, Germany, 2014.

- [54] B. Monge Brenes, Design of Supercritical Carbon Dioxide Centrifugal Compressors, Ph.D. Thesis, Spain: University of Seville, 2014.
- [55] W. Shao, X. Wang, J. Yang, H. Liu and Z. Huang, "Design Parameters Exploration for Supercritical CO<sub>2</sub> Centrifugal Compressors Under Multiple Constraints," in ASME Turbo Expo, Seoul, South Korea, 2016.
- [56] A. J. M. Matos, Preliminary Aerodynamic Design of a Supercritical Carbon Dioxide Centrifugal Compressor, MSc. Thesis,, Canada: University of Carleton, 2017.
- [57] S. Saxena, R. Mallina, F. Moraga and D. Hofer, "Numerical Approach for Real Gas Simulations Part II: Flow Simulation for Supercritical CO<sub>2</sub> Centrifugal Compressor," in ASME Turbo Expo, Charlotte, NC, 2017.
- [58] A. Ameli, A. Afzalifar, T. Turunen-Saaresti and J. Backman, "Centrifugal Compressor Design for Near-Critical Point Applications," Journal of Engineering for Gas Turbines and Power, vol. 141, 2019.
- [59] A. Ameli, Supercritical CO<sub>2</sub> Numerical Modeling and Turbomachinery Design, PhD Thesis, Finland: Lappeenranta-Lahti University of Technology, 2019.
- [60] A. Ameli, T. Turunen-Saaresti, A. Gronman and J. Backman, "Compressor Design Method in the Supercritical CO<sub>2</sub> Applications," in The 6th International Supercritical CO<sub>2</sub> Power Cycles Symposium, Pittsburgh, PA, 2018.
- [61] S. S. Saravi and S. A. Tassou, "An Investigation into sCO<sub>2</sub> Compressor Performance Prediction in The Supercritical Region for Power Systems," Energy Procedia, vol. 161, pp. 403-411, 2019.
- [62] C. Borgnakke and R. E. Sonntag, Fundamentals of Thermodynamics, 8th ed., John Wiley & Sons, 2013.
- [63] A. R. Imre, C. Ramboz, U. K. Deiters and K. T., "Anomalous Fluid Properties of Carbon Dioxide in The Supercritical Region: Application to Geological CO<sub>2</sub> Storage and Related Hazards," Environmental Earth Sciences, vol. 73, pp. 4373-4384, 2015.
- [64] R. Benintendi, "Non-equilibrium phenomena in carbon dioxide expansion," Process Safety and Environmental Protection, vol. 92, pp. 47-59, 2014.
- [65] X. Li, Y. Zhao, H. Yao, M. Zhao and Z. Liu, "A New Method for Impeller Inlet Design of Supercritical CO<sub>2</sub> Centrifugal Compressors in Brayton Cycles," Energies, vol. 13, 2020.
- [66] A. Ameli, T. Turunen-Saaresti and J. Backman, "Numerical Investigation of the Flow Behavior Inside a Supercritical CO<sub>2</sub> Centrifugal Compressor," Journal of Engineering for Gas Turbines and Power, vol. 140, 2018.

- [67] A. Hacks, S. Schuster, H. J. Dohmen, F.-K. Benra and D. Brillert, "Turbomachine Design for Supercritical Carbon Dioxide within the SCO<sub>2</sub>-HeRo.eu Project," Journal of Engineering for Gas Turbines and Power, vol. 140, 2018.
- [68] A. Engeda and J. Chen, "A Review of the Prospect and Challenges for Developing and Marketing a Brayton-Cycle Based Power Genset Gas-Turbine Using Supercritical CO<sub>2</sub>: Part II," in ASME Turbo Expo, Virtual, Online, 2020.
- [69] Q. Zhao, M. Mecheri, T. Neveux, J.-N. Jaubert and R. Privat, "Thermodynamic Model Investigation for Supercritical CO<sub>2</sub> Brayton Cycle for Coal-Fired Power Plant Application," in 5th International Supercritical CO<sub>2</sub> Symposium, San-Antonio, TX, 2016.
- [70] R. Span and W. Wagner, "A New Equation of State for Carbon Dioxide Covering the Fluid Region from the Triple-Point Temperature to 1100 K at Pressures up to 800 MPa," Physical and Chemical Reference Data, vol. 25, pp. 1509-1596, 1996.
- [71] M. T. White, G. Bianchi, L. Chai, S. A. Tassou and A. I. Sayma, "Review of supercritical CO<sub>2</sub> technologies and systems for power generation," Applied Thermal Engineering, vol. 185, 2021.
- [72] L. Chordia, M. Portnoff and E. Green, "High Temperature Heat Exchanger Design and Fabrication for Systems with Large Pressure Differentials, DE-FE0024012," Department of Energy, 2017.
- [73] J. S. Kwon, S. Son, J. Y. Heo and J. I. Lee, "Compact Heat Exchangers for Supercritical CO<sub>2</sub> Power Cycle Application," Energy Conversion and Management, vol. 209, 2020.
- [74] L. Chai and S. Tassou, "A review of printed circuit heat exchangers for helium and supercritical CO<sub>2</sub> Brayton cycles," Thermal Science and Engineering Progress, vol. 18, 2020.
- [75] Q. Zhu, Power Generation from Coal Using Supercritical CO<sub>2</sub> Cycle, IEA Clean Coal Center, 2017.
- [76] "What is a Heatric Printed Circuit Heat Exchanger?," [Online]. Available: <a href="https://www.heatric.com/heatexchangers">https://www.heatric.com/heatexchangers</a>. [Accessed 02 07 2021].
- [77] M. D. Carlson, A. K. Kruizenga, C. Schalansky and D. F. Fleming, "SANDIA Progress on Advanced Heat Exchangers for SCO<sub>2</sub> Brayton Cycles," in The 4th International Symposium-Supercritical CO<sub>2</sub> Power Cycles, Pittsburgh, PA, 2014.
- [78] A. Kruizenga, D. Fleming, M. Carlson and M. Anstey, "Supercritical CO<sub>2</sub> Heat Exchanger Fouling," in The 4th International Symposium-Supercritical CO<sub>2</sub> Power Cycles, Pittsburgh, PA, 2014.
- [79] F. Brunner and P. Krummenacher, "Einführung in die Prozessintegration mit der Pinch-Methode," Bern: Bundesamt für Energie, 2015.

- [80] J. Hosseinpour, J. Howard, J. Chen and A. Engeda, "Challenges for Developing and Marketing a Brayton-Cycle-Based Power Genset Gas Turbine Using Supercritical CO<sub>2</sub> and a Compressor Design for Simple Recuperated Cycle," Energy Resources Technology, vol. 144, 2022.
- [81] "Rotordynamics," [Online]. Available: <a href="https://en.wikipedia.org/wiki/Rotordynamics">https://en.wikipedia.org/wiki/Rotordynamics</a>. [Accessed 08 07 2021].
- [82] J. Chen and A. Engeda, "A Review of The Prospect and Challenges for Developing and Marketing a Brayton-Cycle Based Power Genset Gas-Turbine Using Supercritical CO<sub>2</sub>. Part I: The General System Challenges," in ASME Turbo Expo, London, England, 2020.
- [83] P. A. Chapman, "Advanced Gas Foil Bearing Design for Supercritical CO<sub>2</sub> Power Cycles," in The 6th International Supercritical CO<sub>2</sub> Power Cycles Symposium, Pittsburgh, PA, 2018.
- [84] J. J. Sienicki, A. Moisseytsev, R. L. Fuller, S. A. Wright and P. P. S., "Scale Dependencies of Supercritical Carbon Dioxide Brayton Cycle Technologies and the Optimal Size for a Next-Step Supercritical CO<sub>2</sub> Cycle Demonstration," in SCO<sub>2</sub> Power Cycle Symposium, Boulder, CO, 2011.
- [85] J. Phillips, "Thermal Integration of Closed, Indirect Supercritical CO<sub>2</sub> Brayton Power Cycles with Oxy-Fired Heaters," in NETL CO<sub>2</sub> Capture Technology Project Review Meeting, Pittsburgh, PA, 2017.
- [86] J. E. Cha, S. W. Bae, J. Lee, S. K. Cho, J. I. Lee and J. H. Park, "Operation Results of a Closed Supercritical CO<sub>2</sub> Simple Brayton Cycle," in The 5th International Symposium-Supercritical CO<sub>2</sub> Power Cycles, San Antonio, TX, 2016.
- [87] J. Cho, H. Shin, J. Cho, H.-S. Ra, C. Roh, B. Lee, G. Lee, B. Choi and Y.-J. Baik, "Development and Operation of Supercritical Carbon Dioxide Power Cycle Test Loop with Axial Turbo-Generator," in ASME Turbo Expo, Oslo, Norway, 2018.
- [88] R. Allam, S. Martin, B. Forrest, j. Fetvedt, X. Lu, D. Freed, G. W. Brown, T. Sasaki, M. Itoh and J. Manning, "Demonstration of the Allam Cycle: An Update on the Development Status of a High Efficiency Supercritical Carbon Dioxide Power Process Employing Full Carbon Capture," Energy Procedia, vol. 114, 2017.
- [89] S. Martin, B. Forrest, N. Rafati, X. Lu, J. Fetvedt, M. McGroddy, B. Brown, R. Allam, D. Beauchamp and D. Freed, "Progress Update on the Allam Cycle: Commercialization of NET Power and the NET Power Demonstration Facility," in 14th International Conference on Greenhouse Gas Control Technologies, Melbourne, Australia, 2018.
- [90] T. C. Allison, J. Moore, D. Hofer, M. D. Towler and J. Thorp, "Planning for Successful Transients and Trips in a 1 MWe-Scale High-Temperature sCO<sub>2</sub> Test Loop," Journal of Engineering for Gas Turbines and Power, vol. 141, 2019.

- [91] T. J. Held, "Initial Test Results of a Megawatt-Class Supercritical CO<sub>2</sub> Heat Engine," in The 4th International Symposium on Supercritical CO<sub>2</sub> Power Cycles, Pittsburgh, PA, 2014.
- [92] J. Marion, M. Kutin, A. McClung, J. Mortzheim and R. Ames, "The STEP 10 MWe sCO<sub>2</sub> Pilot Plant Demonstration," in ASME Turbo Expo, Phoenix, AZ, 2019.
- [93] M. A. Reyes-Belmonte, A. Sebastian, M. Romero and J. Gonzalez-Aguilar, "Optimization of a Recompression Supercritical Car-bon Dioxide Cycle for an Innovative Central Receiver Solar Power Plant," Energy, vol. 112, pp. 17-27, 2016.
- [94] R. H. Aungier, Centrifugal Compressors: A Strategy for Aerodynamic Design and Analysis, New York, NY: ASME Press, 2000.
- [95] N. Watson and M. S. Janota, Turbocharging the Internal Combustion Engine, New York, NY: McMillan, 2000.
- [96] A. Whitfield and F. J. Wallace, "Study of incidence loss models in radial and mixed-flow turbomachinery," in Proceedings of the Congress of Heat Fluid Flow in Steam and Gas Turbine Plant, Coventry, UK, 1973.
- [97] O. Conrad, K. Raif and M. Wessels, "The Calculation of Performance Maps for Centrifugal Compressors with Vane-Island Diffusers," in ASME Twenty-fifth Annual International Gas Turbine Conference and Twenty-second Annual Fluids Engineering Conference on Performance Prediction of Centrifugal Pumps and Compressors, New Orleans, LA, 1980.
- [98] W. Jiang, J. Khan and R. A. Dougal, "Dynamic Centrifugal Compressor Model for System Simulation," Journal of Power Sources, vol. 158, pp. 1333-1343, 2006.
- [99] J. E. Coppage, F. Dallenbach, H. P. Eichenberger, G. Hlavaka, E. M. Knoernschild and N. Van Le, "Study of Supersonic Radial Compressors for Refrigeration and Pressurization Systems," Airesearch Manufacturing Company, 1956.
- [100] W. Jansen, "A Method for Calculating the Flow in a Centrifugal Impeller When Entropy Gradients Are Present," in Royal Society Conference on Internal Aerodynamics (Turbomachinery), 1967.
- [101] K. Birdi, Mixed Flow Compressors, Cranfield University Short Course on Centrifugal Compressors, 1992.
- [102] M. P. Boyce, Centrifugal Compressors: A Basic Guide, Tulsa, OK: PennWell, 2003.
- [103] J. P. Johnston and R. C. Dean Jr, "Losses in Vaneless Diffusers of Centrifugal Compressors and Pumps. Analysis, Experiment, and Design," Journal of Engineering for Power, vol. 88, pp. 49-60, 1966.
- [104] J. P. Johnston and J. Moore, "Secondary Flow Mixing Losses in a Centrifugal Impeller," Journal of Engineering for Gas Turbines and Power, vol. 105, pp. 24-32, 1983.

- [105] C. Stuart, S. Spence, D. Filsinger, A. Starke and S. I. Kim, "A Three-Zone Modeling Approach for Centrifugal Compressor Slip Factor Prediction," Turbomachinery, vol. 141, no. 3, 2019.
- [106] K. Klausner and G. U., "Evaluation and Enhancement of a One-Dimensional Performance Analysis Method for Centrifugal Compressors," in ASME Turbo Expo, Düsseldorf, Germany, 2014.
- [107] Y. Zhu and S. A. Sjolander, "Effect of Geometry on the Performance of Radial Vaneless Diffusers," Turbomachinery, vol. 109, pp. 550-556, 1987.
- [108] J. W. Daily and R. E. Nece, "Chamber Dimension Effects on Induced Flow and Frictional Resistance of Enclosed Rotating Disks," Journal of Basic Engineering, vol. 82, pp. 217-232, 1960.
- [109] H. W. Oh, E. S. Yoon and M. K. Chung, "An Optimum Set of Loss Models for Performance Prediction of Centrifugal Compressors," Proceedings of the Institution of Mechanical Engineers, vol. 211, 1997.
- [110] S. L. Dixon and C. A. Hall, Fluid Mechanics and Thermodynamics of Turbomachinery, 6th ed., Elsevier, 2010.
- [111] O. E. Balje, Turbomachines: a guide to design selection and Theory, New York, NY: John Wiley & Sons, 1981.
- [112] J. Hosseinpour, M. Messele and A. Engeda, "Analysis and Design of Centrifugal Compressor for 10 MWe Supercritical CO<sub>2</sub> Brayton Cycles," Mechanical Science and Technology, vol. 37, no. 5, 2023.
- [113] D. Eckardt, "Instantaneous Measurements in the Jet-Wake Discharge Flow of a Centrifugal Compressor Impeller," Journal of Engineering and Power, vol. 97, pp. 337-346, 1975.
- [114] D. Eckardt, "Detailed Flow Investigations within a High-Speed Centrifugal Compressor Impeller," Journal of Fluid Engineering, vol. 98, pp. 390-402, 1976.
- [115] D. Eckardt, "Flow Field Analysis of Radial and Backswept Centrifugal Compressor," in Performance Prediction of Centrifugal Pumps and Compressors, Gopalskrishnan, S., Cooper, P., ASME, 1980.
- [116] J. Hosseinpour, M. Messele and A. Engeda, "Design and Development of a Stable Supercritical CO<sub>2</sub> Centrifugal Compressor," Energy (Under Review).
- [117] ANSYS CFX-Solver Theory Guide, 2021 R1, ANSYS, Inc., 2021.
- [118] [Online]. Available: https://turbmodels.larc.nasa.gov/sst.html. [Accessed 16 02 2023].

- [119] J. Hosseinpour and H. Mahdavy-Moghaddam, "Computational study of magnetic field effects on the nozzle of hydrogen micro flame," Combustion and Flame, vol. 220, pp. 247-256, 2020.
- [120] H. Mahdavy-Moghaddam and J. Hosseinpour, "Numerical investigation of magnetic field effect on hydrogen flame," Aerospace Knowledge and Technology Journal, vol. 5, no. 1, pp. 31-40, 2016.
- [121] J. Hosseinpour, L. Bravo and O. Samimi-Abianeh, "Computational study of unsteady cavitating flows and erosion in a fuel nozzle," in ASME ICEF Technical Conference. San Diego, California, 2018.
- [122] M. Pandey, B. N. Padhi and I. Mishra, "Numerical simulation of solar parabolic trough collector with viscous dissipation in slits of arc-plug insertion," Journal of Solar Energy, vol. 230, 2021.
- [123] ANSYS Fluent Beta Features Manual, 2021 R1, Section 6.1.1., ANSYS, Inc., 2021.
- [124] D. Fleming, A. Kruizenga, J. Pasch, T. Conboy and M. Carlson, "Corrosion and Erosion Behavior in Supercritical CO<sub>2</sub> Power Cycles," in ASME Turbo Expo, Düsseldorf, Germany, 2014.
- [125] "CO<sub>2</sub> Corrosion," TWI LTD, [Online]. Available: <a href="https://www.twi-global.com/what-we-do/research-and-technology/technologies/materials-and-corrosion-management/corrosion-testing/co2-corrosion">https://www.twi-global.com/what-we-do/research-and-technology/technologies/materials-and-corrosion-management/corrosion-testing/co2-corrosion</a>. [Accessed 19 01 2023].
- [126] "Nozzle Applet," Virginia Tech, [Online]. Available: <a href="https://www.engapplets.vt.edu/fluids/CDnozzle/cdinfo.html">https://www.engapplets.vt.edu/fluids/CDnozzle/cdinfo.html</a>. [Accessed 18 01 2023].